THE UNIVERSITY OF ALABAMA IN HUNTSVILLE
FINAL REPORT ON NASA CONTRACT
NAS8-38609 Delivery Order No. 96

SUPERFLUID HELIUM SLOSHING DYNAMICS INDUCED OSCILLATIONS AND FLUCTUATIONS OF ANGULAR MOMENTUM, FORCE AND MOMENT ACTUATED ON SPACECRAFT DRIVEN BY GRAVITY GRADIENT OR JITTER ACCELERATION ASSOCIATED WITH SLEW MOTION

Prepared by
R. J. Hung, Ph.D., P.E.
Professor of Mechanical and Aerospace Engineering
The University of Alabama in Huntsville
Huntsville, Alabama 35899, USA

February 1994

(NASA-CR-193928) SUPERFLUID HELIUM SLOSHING DYNAMICS INDUCED OSCILLATIONS AND FLUCTUATIONS OF ANGULAR MOMENTUM, FORCE AND MOMENT ACTUATED ON SPACECRAFT DRIVEN BY GRAVITY GRADIENT OR JITTER ACCELERATION ASSOCIATED WITH SLEW MOTION Final Report (Alabama Univ.) 106 p

N94-27931

Unclas

G3/34 0000304

Abstract

The generalized mathematical formulation of sloshing dynamics for partially filled liquid of cryogenic superfluid helium II in dewar containers driven by the gravity gradient and jitter accelerations associated with slew motion for the purpose to perform scientific observation during the normal spacecraft operation are investigated. An example is given with the Advanced X-Ray Astrophysics Facility-Spectroscopy (AXAF-S) for slew motion which is responsible for the sloshing dynamics. The jitter accelerations include slew motion, spinning motion, atmospheric drag on the spacecraft, spacecraft attitude motions arising from machinery vibrations, thruster firing, pointing control of spacecraft, crew motion, etc. Explicit mathematical expressions to cover these forces acting on the spacecraft fluid systems are derived. The numerical computation of sloshing dynamics is based on the non-inertia frame spacecraft bound coordinate, and solve time-dependent, three-dimensional formulations of partial differential equations subject to initial and boundary conditions. The explicit mathematical expressions of boundary conditions to cover capillary force effect on the liquid-vapor interface in microgravity environments are also derived. The formulations of fluid moment and angular moment fluctuations in fluid profiles induced by the sloshing dynamics, together with fluid stress and moment fluctuations exerted on the spacecraft dewar containers have also been derived. Examples are also given for cases applicable to the AXAF-S spacecraft sloshing dynamics associated with slew motion.

Acknowledgement

The authors appreciate the support received from the National Aeronautics and Space Administration through the NASA contract NAS8-38609/Delivery Order No. 96. The extensive computer simulations accomplished by H. L. Pan and Y. T. Long of the University of Alabama in Huntsville (UAH) are greatly acknowledged. All the computational supports provided by UAH through the Alabama Supercomputer System are also appreciated. They would like to express their gratitude to Gerald S. Nurre, John P. Sharkey, and Philip C. Calhoun of NASA/Marshall Space Flight Center for the stimulating discussions during the course of the present study.

Statement of Work for the Numerical Simulation of The AXAF-S Superfluid Helium Cryogenic Dewar Slosh Dynamics

In order to support the Advanced X-ray Astrophysics Facility-Spectroscopy (AXAF-S) Cryogenic Subsystem (CSS) Preliminary Design Review (PDR), the following tasks have been carried out and accomplished in this research project:

1. Adopt the numerical model of the Gravity Probe-B cryogenic, superfluid helium dewar to the AXAF-S configuration by removing the center core tube, adjusting fluid dynamic coefficients for AXAF-S nominal fluid temperature of 1.3 K, and adjusting the rigid body spacecraft mass properties and orbital parameters to those associated with AXAF-S. In compliance with AXAF-S numerical model, mathematical formulations of the dynamic model of gravity gradient and external jitter accelerations associated with slew motions have been developed. Detailed descriptions are illustrated in pages 5 to 27 of the present report.
2. Assume a worst case ratio of fluid-to-dewar volume with respect to slosh dynamics in the range of 70% and establish the equilibrium conditions for fluid state with zero vehicle internal angular velocity. Figure 10 in this report shows the equilibrium conditions illustrated.
3. In order to perform the numerical simulations to determine fluid profiles, the levels of force and torque applied to the AXAF-S spacecraft by the superfluid in response to the gravity gradient and jitter accelerations associated with slew motion. Mathematical derivation of fluid profiles including angular momentum and moment

fluctuations driven by both gravity gradient and jitter accelerations associated with slew motions are illustrated in pages 27 to 30 while the mathematical formulation of force and torque applied to the spacecraft system are described in pages 30 to 37 of the present report. Examples of numerical simulations applicable to AXAF-S spacecraft by superfluid helium in response to vehicle accelerations have been carried out which include the following items:

(a) Time-dependent, three-dimensional bubble configuration oscillations, bubble mass center fluctuations, angular momentum and moment fluctuations of 70% liquid-filled superfluid helium flow profiles, and force and torque actuated on the dewar container of spacecraft driven by gravity gradient acceleration associated with slew motion during a time period of 800 seconds have been carried out. The results are fully illustrated in pages 37 to 53 and in Figures 10 to 15 and 22 to 27 of this report.

(b) Time-dependent, three-dimensional liquid-vapor interface oscillations of superfluid helium, bubble mass center fluctuations, angular momentum and moment disturbances of 70% liquid-filled cryogenic helium flow profiles, and force and torque applied on the dewar container of AXAF-S spacecraft driven by external acceleration jitter associated with slew motion at amplitudes of 10^{-5} g_o (g_o=9.81 m/s^2) during a time period of 800 seconds have been carried out. These results have been illustrated in pages 39 to 53 and in Figures 16 to 21 and 28 to 31 of this report.

Because unexpected complications in numerical instabilities and convergent problems occurred during the execution of iterations in numerical computation, computation of white noise frequency spectrum was unable to accomplish during the period of time in this research. The total expenses of computer service are completely covered by the University of Alabama in Huntsville (UAH) without charge to the government. The amount of computational expenses supported by UAH exceeded the amount of expenses supported by the government in this project.

Data outputs from these numerical simulations had been provided to the Contracting Officer's Technical Representative (COTR) in both graphical form and on 3.5 inch micro-floppy diskettes in a disk format as required by the contract.

TABLE OF CONTENTS

I. Introduction

For the purpose to carry out scientific experiments, some experimental spacecraft use cryogenic cooling for observation instrumentation and telescope, superconducting sensors for gyro read-out and maintain very low temperature near absolute zero for mechanical stability. The approaches to both cooling and control involve the use of superfluid liquid helium II. In this study, sloshing dynamics associated with spinning and/or slew motions are investigated. To cover the spacecraft spinning and/or slew motions, Gravity Probe-B (GP-B) and Advanced X-Ray Astrophysics Facility-Spectroscopy (AXAF-S) spacecrafts have been chosen as the examples in this study. Both the GP-B and the AXAF-S spacecrafts adopt the cooling and boil-off from the cryogenic liquid helium dewar as a cryogen and propellant to maintain the cooling of instrumentations, attitude control and drag-free operation of the spacecraft. The potential problems for cryogenic liquid in dewar container could be due to asymmetry in the static liquid helium distribution and to perturbations in the liquid-vapor interface caused by slosh wave excitation driven by pointing control, machinery vibration, etc.

For the cases of both the GP-B and the AXAF-S spacecrafts, cryogenic liquid helium II, at a temperature of 1.3 K, is used as the propellant. With its superconducting behavior, there is no temperature gradients in the liquid helium. In the absence of temperature gradient along the surface which drive Marangoni convection, the equilibrium shape of the free surface is governed by a balance of capillary, centrifugal and gravitational forces. Determination of liquid-vapor interface profiles based on computational experiments can uncover details of the flow which can not be easily visualized or measured experimentally in a microgravity environment.

The instability of the liquid-vapor interface surface can be induced by the presence of longitudinal and lateral accelerations. Slosh waves are, thus, excited which produces high and low frequency oscillations in the liquid propellant. The sources of the residual accelerations range from the effects of the Earth's gravity gradient and jitter accelerations which include, atmospheric drag on the spacecraft, vibration of compressor, spacecraft attitude motions arising from machinery vibrations, thruster firings, spacecraft slew motion, pointing control of spacecraft, crew motion, etc. Recent study (Kamotani et al., 1981) suggest that the high frequency accelerations may be unimportant in comparison to the residual motions caused by low frequency accelerations.

Time-dependent dynamical behavior of partially-filled rotating fluids in reduced gravity environments was simulated by numerically solving the Navier Stokes equations subject to the initial and the boundary conditions (Hung and Shyu, 1991 a,b,c; 1992 a,b,c; Hung et al., 1991 a,b,c; 1992 a,b,c). At the interface between the liquid and the gaseous fluids, both the kinematic surface boundary condition, and the interface stress conditions for components tangential and normal to the interface, were applied (Hung and Shyu, 1991 a,b,c; 1992 a,b,c; Hung et al., 1991 a,b,c; 1992 a,b,c). The initial conditions were adopted from the steady-state formulations developed by Hung et al (1989 a,b,c). Some of the steady-state formulations of interface shapes were compared with the available experiments carried out by Leslie (1985) in a free-falling aircraft (KC-135). The experiments carried out by Mason et al (1978) showed that the classical fluid mechanics theory is applicable for cryogenic liquid helium in large containers.

In the spacecraft orbit around the Earth, the direction of azimuth angle of Earth toward the location of the spacecraft geometric center varies from 0° along the rolling axis of spacecraft to various directions in which three dimensional calculation shall be adopted.

As the spacecraft moves along the orbit, any fluid capable of motion relative to the spacecraft is subject to the acceleration that arises from the gravity gradients of the Earth (Avduyevsky, 1984; Forward, 1982; Misner et al., 1973). The interaction between the particle mass of fluid and the spacecraft mass due to gravity gradient accelerations (Forward, 1982) are capable for the excitation of slosh waves and disturb the fluid system which induces the fluctuations of viscous stress and its moment exerted on the containers of the spacecraft fluid systems. In the meanwhile, the sources of residual acceleration of gravity jitter range from atmospheric drag on the spacecraft, background gravity, spacecraft attitude motions arising from machinery vibrations, spacecraft slew motion, thruster firings, crew motion, etc., are also capable for the excitation of slosh waves on the fluid containers.

It is critically important to understand the physical and dynamical behavior of cryogenic helium in a rotating cylinder to effectively promote space-oriented missions.

At temperatures close to absolute zero, quantum effects begin to be of importance in the properties of fluids. At a temperature of 2.17°K, liquid helium has a λ-point (a second-order phase transition); at temperatures below this point liquid helium (helium II) has a number of remarkable properties, the most important of which is superfluidity. This is the property of being able to flow without viscosity in narrow capillaries or gaps.

The basis of the dynamics of helium II is the following fundamental result of microscopic theory. At temperatures other than zero, helium II behaves as if it were a mixture of two different liquids. One of these is a superfluid and moves with zero viscosity along a solid surface. The other is a normal viscous fluid. It is of great importance that no friction occurs between these two parts of the liquid in their relative motion, i.e., no momentum is transferred from one to the other.

It should be emphasized that regarding the liquid as a mixture of normal and superfluid parts is no more than a convenient description of the phenomena which occur in a fluid where quantum effects are important. One of these motions is normal and has the same properties as the motion of an ordinary viscous fluid, but the other is the motion of a superfluid. The two motions occur without any transfer of momentum from one to another. We can, in a certain sense, speak of the superfluid and normal parts of the fluid, but this does not mean that the fluid can actually be separated into two such parts.

If fluid flow can separate helium II into the regions of the superfluid and the normal fluid, two temperatures zones are immediately created. A very low temperature zone is located at the zone of very high density concentration of the superfluid, while a high temperature (below 2.17° K) zone is located at the zone of very high density concentration of the normal fluid at the other end. The existence of a sharp temperature gradient at the interface between the superfluid and the normal fluid results in the creation of a great difference in chemical potential, which, in turn, induces a great reverse pressure gradient, creating the environment of isothermal fluid distribution everywhere throughout the cylinder and homogenous distribution of superfluid density concentration. This illustration of the possible separation of superfluid from normal fluid of helium II means that there is in reality, no way for anyone to achieve the separation of the superfluid from the normal fluid of helium II. In other words, in considering the dynamical behavior of helium II in a large rotating cylinder, a mixture of the superfluid and the normal fluid without separation of the two fluids is accounted for in the model computation. Density concentration of superfluid is a function of temperature, which is also true for the surface tension and viscous coefficient for helium II (Wilks, 1967; Hoare et al., 1961; Hung, 1990; Hung and Lee, 1992). In fact, the experiments carried out by Mason et al. (1978) showed that the classical fluid mechanics theory is applicable for cryogenic liquid helium in a large container. In this study, the theory of viscous Newtonian fluids is employed with modification of transport coefficients adjusted by normal and superfluid density concentration which is a function of temperature.

II. Functions of Scientific Observation and Spacecraft Motions

The AXAF-S spacecraft is a sun synchronous Earth satellites orbiting at 650 km altitude directly over the poles. The functions of scientific observation for the AXAF-S spacecrafts and its motions are illustrated as follows:

The AXAF-S with its sister spacecraft AXAF-I (I for imaging) are two spacecrafts restructured from the original AXAF design to carry out astrophysical observation. Equipped with the (microcalorimeter) X-Ray Spectrometer (XRS), AXAF-S provides high-throughput, high-resolution, non-dispersive spectroscopy at the higher AXAF x-ray energies - including the astrophysically important iron-K spectral region (above 6.4 keV) - and also permits some spatially resolved high-resolution spectroscopy. AXAF-S comprises a foil-mirror (or possibly, a replication-optic) telescope (4.7-m focal length), with XRS in the focal plane. With the baseline optical system, the AXAF-S provides important, unique capabilities for high-throughput, high resolution (above 1 keV) spectroscopy of extended and point sources and for some spatially resolved high-resolution spectroscopy.

Because of the unique capabilities for high-resolution spectroscopy of point and extended sources, AXAF-S is eligible to carry out following scientific programs:

(1) Distance scale: Measure the cosmological distance scale using the Krolik-Raymond-Sarazin technique in clusters of galaxies. The technique requires comparison of the equivalent width of an absorption line of the spectrum of a background (or central) active galactic nuclei (AGN) observed through a cluster of galaxies, with emission-line flux of the same line from the cluster itself.

(2) Active Galactic Nuclei (AGN): Detect x-ray emission from the hot intercloud medium around AGN. Study photo-ionized environs of AGN through analysis of the redshift and line shape of the resonance fluorescence line of iron.

(3) Absorption features: Analyze absorption edges to determine abundance, ionization, and column densities of absorbing clouds around active galactic nuclei and in the interstellar medium.

(4) Cooling flows: Conduct a detailed study of cooling flows in giant elliptical galaxies and in clusters of galaxies. Isolate emission from cooling regions from the hot plasma. Determine abundances, temperatures, and their radial dependence.

(5) Clusters of galaxies: Measure redshift and velocity dispersion of intracluster medium. Determine the dynamical properties of the emitting gas, for direct comparison with simulations of cluster merging. Measure the evolution of the abundances of low-Z elements.

(6) Supernova remnants: Trace plasma diagnostics in low-surface-brightness areas of supernova remnants. Determine spatial dependence of temperature and ionization age for young supernova remnants, using spatially resolved high-resolution spectra.

(7) X-ray binaries: Determine the sites at which Fe line emission originates in individual binary x-ray sources. The width and temporal behavior of (hot-plasma) recombination and (cold-plasma) fluorescence lines (most strongly Fe-K) probe the spatial structure of the environs of the compact x-ray source.

(8) Stars: Perform time-resolved spectroscopy to examine plasma heating and cooling during stellar flares. For eclipsing binaries, determine location of active regions of the corona.

To comprise these functions of scientific observation, AXAF-S equipped with foil-mirror telescope and XRS in the focal plane is capable to observe point and extended sources of AGN, clusters of galaxies, supernova remnants, x-ray binaries, stellar flares, active regions of corona, etc., through spacecraft slew motion of pointing control. In other words, spacecraft slew motion without spinning with rotating axis is required for AXAF-S to perform its scientific mission.

III. Basic Characteristics of Gravity Gradient and Gravity Jitter Accelerations

Any fluid element inside the on-orbit spacecraft fluid system is subject to the acceleration that arises from the gravity gradient of the Earth (Avduyevsky, 1984; Forward, 1982; Misner et al., 1973; Hung and Pan, 1993; Hung et al., 1993 a,b,c). Once the spacecraft orbit is fixed, the orbit period is determined and the basic structure of the gravity gradient acceleration also can be calculated. However, gravity gradient acceleration acting on each fluid element inside the on-orbit spacecraft fluid system is different dependent upon the distance of the location of the fluid element to the geometrical center of the spacecraft and its direction toward the location of the center of the Earth.

This acceleration can only be calculated based on the non-inertia frame of spacecraft bound coordinate. Thus, the coordinate system shall be transformed from ordinary inertia frame coordinate to non-inertia coordinate.

(A) Orbit Motion of Spacecraft

Let us consider the case of the AXAF-S spacecraft, which is the Earth satellites orbiting at 650 km altitude directly over the poles, the orbit period, τ_o can be computed from following expression:

$$\tau_o = 2\pi \frac{R_c^{3/2}}{R_E g_o^{1/2}} \tag{3-1}$$

where R_E denotes the radius of Earth ($= 6373$ km); R_c, the radius of the circular orbit ($= R_E + h = 7023$ km); h, orbit altitude ($= 650$ km); and g_o, Earth gravity acceleration ($= 9.81\ ^m/s^2$). For the case of the AXAF-S spacecraft, the orbit period $\tau_o = 97.6$ min, and orbit rate $n = {}^{2\pi}/\tau_o = 1.07 \times 10^{-3}\ ^{rad}/_s$.

As the spacecraft is orbiting around the Earth, the azimuth angle of the Earth, ψ_E, toward the location of the spacecraft geometric center varies with respect to time. At time $t = 0$, the rolling axis of the spacecraft is aligned with the radial direction of the Earth's center to the spacecraft geometric center. Assuming the spacecraft rolling axis is linearly turning around 0° to 360° in the orbit period, τ_o, of the spacecraft when the spacecraft is orbiting around the Earth. Without the spacecraft slew motion, the azimuth angle (ψ_{Eo}) can be defined as

$$\psi_{E_o} = \frac{2\pi}{\tau_o} t \tag{3-2}$$

where τ_o is the spacecraft orbit period [defined in Equation (3-1)]; and t is the time measured from the instant when the direction of the spacecraft rolling axis is aligned with the radial direction of the spacecraft mass center to the center of the Earth.

(B) Slew Motion of Spacecraft

For the purpose to carry out wide-range observations, some scientific spacecraft requires slew motion with respect to the mass center of the spacecraft. This is particularly true for the case of the AXAF-S spacecraft. For the case of the spacecraft slew motion, azimuth angle, shown in Equation (3-2), shall be modified through the coordinate transformation of slew motion when the spacecraft is orbiting around the Earth.

Let us assume that the slew motion starts with the center located at the mass center of the spacecraft. Let us choose cartesian coordinate (x", y", z") with z"-axis along the axis of the dewar container (see Figure 1). At time $t = 0$, the radial vector $\hat{r}_c$ from the center of the spacecraft to the center of the Earth lies on the x"-z" plane of the cartesian coordinate chosen (see Figure 2). The azimuth angle ψ_E is defined as the angle between the radial vector $\hat{r}_c$ and the z"-axis. Rotation matrices for spinning and/or slew motions along the x"-, y"- and z"-axes can be expressed as

$$\begin{bmatrix} 1 & 0 & 0 \\ 0 & \cos\omega_x t & \sin\omega_x t \\ 0 & -\sin\omega_x t & \cos\omega_x t \end{bmatrix}, \begin{bmatrix} \cos\omega_y t & 0 & -\sin\omega_y t \\ 0 & 1 & 0 \\ \sin\omega_y t & 0 & \cos\omega_y t \end{bmatrix}, \begin{bmatrix} \cos\omega_z t & \sin\omega_z t & 0 \\ -\sin\omega_z t & \cos\omega_z t & 0 \\ 0 & 0 & 1 \end{bmatrix}$$

respectively. Here, ω_x, ω_y and ω_z denote angular velocity of slew and/or spinning motions along the x"-, y"- and z"-axes, respectively. Radial vector $\hat{r}_c$ in cartesian coordinate without slew and spinning motion is (see Figure 2)

$$\hat{r}_{co} = [\sin\psi_{Eo}, 0, -\cos\psi_{Eo}] \qquad (3-3)$$

With an execution of spinning motion along the z"-axis only, radial vector $\hat{r}_c$ becomes (see Figure 2)

$$\hat{r}_{c-z} = \begin{bmatrix} \cos\omega_z t & \sin\omega_z t & 0 \\ -\sin\omega_z t & \cos\omega_z t & 0 \\ 0 & 0 & 1 \end{bmatrix} \begin{bmatrix} \sin\psi_{Eo} \\ 0 \\ -\cos\psi_{Eo} \end{bmatrix}$$

$$= [\sin\psi_{Eo}\cos\omega_z t, -\sin\psi_{Eo}\sin\omega_z t, -\cos\psi_{Eo}] \qquad (3\text{-}4)$$

With an execution of slew motion along the y"-axis only, radial vector $\hat{r}_c$ becomes (see Figure 2)

$$\hat{r}_{c-y} = \begin{bmatrix} \cos\omega_y t & 0 & -\sin\omega_y t \\ 0 & 1 & 0 \\ \sin\omega_y t & 0 & \cos\omega_y t \end{bmatrix} \begin{bmatrix} \sin\psi_{Eo} \\ 0 \\ -\cos\psi_{Eo} \end{bmatrix}$$

$$= [\sin(\psi_{Eo}+\omega_y t), 0, -\cos(\psi_{Eo}+\omega_y t)] \qquad (3\text{-}5)$$

With an operation of slew motion along the x"-axis only, radial vector $\hat{r}_c$ becomes (see Figure 2)

$$\hat{r}_{c-x} = \begin{bmatrix} 1 & 0 & 0 \\ 0 & \cos\omega_x t & \sin\omega_x t \\ 0 & -\sin\omega_x t & \cos\omega_x t \end{bmatrix} \begin{bmatrix} \sin\psi_{Eo} \\ 0 \\ -\cos\psi_{Eo} \end{bmatrix}$$

$$= [\sin\psi_{Eo}, -\cos\psi_{Eo}\sin\omega_x t, -\cos\psi_{Eo}\cos\omega_x t] \qquad (3\text{-}6)$$

In other words, radial vector $\hat{r}_c$ will be modified from the mathematical expression shown in Equation (3-3) to (3-4), (3-5) and (3-6) for the slew and/or spinning motions along the z"-, y"-, and x"-axes alone, respectively. In particular, for the case of slew motion along the y"-axis, comparison between Equations (3-3) and (3-5), it shows that the azimuth angle will be modified as

$$\psi_E = \psi_{Eo} + \omega_y t \qquad (3\text{-}7)$$

For the successive operations of the spacecraft from spinning motion along the z"-axis, then slew motion along the y"-axis, and then slew motion along the x"-axis, radial vector $\hat{r}_c$ results

$$\hat{r}_{c-z,y,x} = \begin{bmatrix} 1 & 0 & 1 \\ 0 & \cos\omega_x t & \sin\omega_x t \\ 0 & -\sin\omega_x t & \cos\omega_x t \end{bmatrix} \begin{bmatrix} \cos\omega_y t & 0 & -\sin\omega_y t \\ 0 & 1 & 0 \\ \sin\omega_y t & 0 & \cos\omega_y t \end{bmatrix} \cdot$$

$$\cdot \begin{bmatrix} \cos\omega_z t & \sin\omega_z t & 0 \\ -\sin\omega_z t & \cos\omega_z & 0 \\ 0 & 0 & 1 \end{bmatrix} \begin{bmatrix} \sin\psi_{Eo} \\ 0 \\ -\cos\psi_{Eo} \end{bmatrix} \qquad (3\text{-}8)$$

To give a practical example for spacecraft slew motion along the x"-axis and/or y"-axis, starting and ending conditions for angular position, angular velocity and angular acceleration of slew motion can be given as $\theta_s(t_o) = 0$, $\theta_s(t_f) = \pi/2$, $\dot{\theta}_s(t_o) = \dot{\theta}_s(t_f) = \ddot{\theta}_s\ (t_o) = \ddot{\theta}(t_f) = \dddot{\theta}(t_o) = \dddot{\theta}(t_f) = 0$ where t_o, t_f, $\dot{\theta}_s$, $\ddot{\theta}_s$, and $\dddot{\theta}_s$ denote starting time, ending time, first time derivative, second time derivative and third time derivative of the angle of slew motion, respectively, expressions of θ_s, $\dot{\theta}_s$, $\ddot{\theta}_s$ become

$$\theta_s(t) = a_7 t^7 + a_6 t^6 + a_5 t^5 + a_4 t^4 \qquad (rad) \qquad (3\text{-}9)$$

$$\dot{\theta}_s(t) = \omega_s(t) = 7a_7 t^6 + 6a_6 t^5 + 5a_5 t^4 + 4a_4 t^3 \ (rad/\mathrm{min}) \qquad (3\text{-}10)$$

$$\ddot{\theta}_s(t) = \alpha_s(t) = 42a_7 t^5 + 30a_6 t^4 + 20a_5 t^3 + 12a_4 t^2 \ (rad/\mathrm{min}^2) \qquad (3\text{-}11)$$

where ω_s and α_s denote angular velocity and angular acceleration of slew motion, respectively. If the slew motion operates at 90° in 10 minutes, the coefficients of angular position a_7, a_6, a_5 and a_4, shown in Equations (3-4) to (3-6), can be expressed as follows:

$a_7 = -3.14159 \times 10^{-6}$, $a_6 = 1.09956 \times 10^{-4}$, $a_5 = -1.31947 \times 10^{-3}$

$a_4 = 5.49778 \times 10^{-3}$, and $t_f = 10$ min.

The expressions of θ_s, ω_s, α_s are illustrated in Figures 3, 4 and 5, respectively.

In addition to the modification of the azimuth angle made by the spacecraft slew motion through the formulation of coordinate transformation, shown in Equation (3-3) to (3-8), accelerations are also induced to activate on the fluid mass in the dewar container. Accelerations acting on the fluid particle in the dewar induced by the slew motion of the spacecraft with the coordinate fixed at the spacecraft center of the mass is as follows (see Figure 1):

$$\ddot{\vec{R}}_p = \vec{\omega} x (\vec{\omega} x \vec{R}_p) + \vec{\alpha} x \vec{R}_p + 2 \vec{\omega} x \vec{V} \qquad (3-12)$$

where $\vec{R}_p$ denotes the position vector of the fluid particle in the dewar container relative to the body frame of the spacecraft; $\vec{\omega}$, angular velocity of the spacecraft body frame; $\vec{\alpha}$, angular acceleration of the spacecraft body frame; and $\vec{v}$, velocity of the fluid particle relative to the spacecraft body frame.

As we indicated earlier, let us assume that the slew motion starts with the center located at the spacecraft mass center, cartesian coordinate (x'', y'', z'') is chosen with origin located at the spacecraft mass center. Let us also assume that x''-z'' plane intersects the center of Earth and the spacecraft mass center. In other words, azimuth angle of Earth toward the spacecraft mass center lies in the x''-z'' plane. Slew motion is along both the x''- and y''-coordinates. Thus, $\vec{\omega}_s = (\omega_{sx}, \omega_{sy}, 0)$ and $\vec{\alpha}_s = (\alpha_{sx}, \alpha_{sy}, 0)$, $\ddot{\vec{R}}_p$ due to slew motion becomes

$$\ddot{\vec{R}}_{p,slew} = \begin{bmatrix} \ddot{\vec{R}}_{x''} \\ \ddot{\vec{R}}_{y''} \\ \ddot{\vec{R}}_{z''} \end{bmatrix}_{slew} = \begin{bmatrix} \omega_{sy}(\omega_{sx}R_y - R_x\omega_{sy}) + \alpha_{sy}R_z + 2\omega_{sy}V_z \\ -\omega_{sx}(\omega_{sx}R_y - R_x\omega_{sy}) - \alpha_{sx}R_z - 2\omega_{sx}V_z \\ -R_z(\omega_{sx}^2 + \omega_{sy}^2) + (\alpha_{sx}R_y - \alpha_{sy}R_x) + 2(\omega_{sx}V_y - \omega_{sy}V_x) \end{bmatrix}_{slew}$$

(3-13)

(C) Coupling for the Accelerations of Spinning and Slew Motion of Spacecraft

As we indicated in Section II of this report, with their specified functions of scientific observation, the dewar container of the GP-B is spinning with a certain rotating rate without slew motion during the normal operation while AXAF-S requires slew motion for pointing control to observe point and extended sources of astronomical objects without spinning. For some particular reasons required in other spacecraft, it might be faced with the situation that both spinning and slew motions are needed simultaneously. To encounter this case, the following formulations are made to deal with coupling for the accelerations of spinning and slew motion of the spacecraft:

$$\ddot{\vec{R}}_{p,\,slew\ and\ spinning} = \begin{bmatrix} \ddot{\vec{R}}_x \\ \ddot{\vec{R}}_y \\ \ddot{\vec{R}}_z \end{bmatrix}_{slew\ and\ spinning}$$

$$= \begin{bmatrix} \omega_{sy}(\omega_{sx}R_y - \omega_{sy}R_x) + \alpha_{sy}R_z + 2\omega_{sy}V_z \\ -\omega_{sx}(\omega_{sx}R_y - \omega_{sy}R_x) - \alpha_{sx}R_z - 2\omega_{sx}V_z \\ -R_z(\omega_x^2 + \omega_{sy}^2) + (\alpha_{sx}R_y - \alpha_{sy}R_x) + 2(\omega_{sx}V_y - \omega_{sy}V_x) \end{bmatrix}_{slew}$$

$$+ \begin{bmatrix} -(\omega_z R_x - \omega_{sx}R_z)\omega_z - \dot{\omega}_z R_y - 2\omega_z V_y \\ (\omega_{sy}R_z - \omega_z R_y)\omega_z + \dot{\omega}_z R_x + 2\omega_z V_x \\ (\omega_{sx}R_x + \omega_{sy}R_y)\omega_z \end{bmatrix}_{spinning\ and\ coupling} \qquad (3\text{-}14)$$

where ω_z and $\dot{\omega}_z$ denote angular velocity and angular acceleration, respectively, of spacecraft spinning motion along the z-axis.

For the case of the GP-B spacecraft, there is no slew motion and the spinning is the only acceleration acting on the spacecraft fluid system. Acceleration due to spacecraft spinning motion becomes

$$\ddot{\vec{R}}_{p,\,spinning} = \begin{bmatrix} \ddot{\vec{R}}_x \\ \ddot{\vec{R}}_y \\ \ddot{\vec{R}}_z \end{bmatrix}_{spinning} = \begin{bmatrix} -R_x\omega_z^2 - R_y\dot{\omega}_z - 2\omega_z V_y \\ -R_y\omega_z^2 + R_x\dot{\omega}_z + 2\omega_z V_x \\ 0 \end{bmatrix}_{spinning} \qquad (3\text{-}15)$$

To convert the expression of Equation (3-15) in cartesian coordinate to cylindrical coordinate, by using the relationships of $(R_x, R_y) = (r\cos\theta, r\sin\theta)$ and $(v_x, v_y) = (u_r \cos\theta - u_\theta \sin\theta, u_r \sin\theta + u_\theta \cos\theta)$, Equation (3-15) becomes

$$\ddot{\vec{R}}_{p,\,spinning} = \begin{bmatrix} \ddot{\vec{R}}_x \\ \ddot{\vec{R}}_y \\ \ddot{\vec{R}}_z \end{bmatrix}_{spinning} = \begin{bmatrix} -r\cos\theta\,\omega_z^2 - r\sin\theta\,\dot{\omega}_z - 2(u_r\sin\theta + u_\theta\cos\theta)\,\omega_z \\ -r\sin\theta\,\omega_z^2 + r\cos\theta\,\dot{\omega}_z + 2(u_r\cos\theta - u_\theta\sin\theta)\,\omega_z \\ 0 \end{bmatrix}_{spinning}$$

and (3-16)

$$\ddot{\vec{R}}_{p,\,spinning} = \begin{bmatrix} \ddot{\vec{R}}_r \\ \ddot{\vec{R}}_\theta \\ \ddot{\vec{R}}_z \end{bmatrix}_{spinning} = \begin{bmatrix} \ddot{\vec{R}}_x\cos\theta + \ddot{\vec{R}}_y\sin\theta \\ -\ddot{\vec{R}}_x\sin\theta + \ddot{\vec{R}}_y\cos\theta \\ \ddot{\vec{R}}_z \end{bmatrix}_{spinning} = \begin{bmatrix} -r\omega_z^2 - 2u_\theta\omega_z \\ r\dot{\omega}_z + 2u_r\omega_z \\ 0 \end{bmatrix}_{spinning} \qquad (3\text{-}17)$$

Accelerations induced by spacecraft spinning motion alone becomes

$$\begin{bmatrix} a_r \\ a_\theta \\ a_z \end{bmatrix}_{spinning} = -\begin{bmatrix} \ddot{\vec{R}}_r \\ \ddot{\vec{R}}_\theta \\ \ddot{\vec{R}}_z \end{bmatrix}_{spinning} = \begin{bmatrix} r\omega_z^2 + 2u_\theta\omega_z \\ -r\dot{\omega}_z - 2u_r\omega_z \\ 0 \end{bmatrix}_{spinning} \qquad (3\text{-}18)$$

(D) Gravity Gradient Acceleration

The gravity gradient acceleration acting on the fluid mass of spacecraft can be shown as

$$\hat{a}_{gg} = -n^2\,[3\,(\hat{r}_c\cdot\vec{d})\,\hat{r}_c - \vec{d}\,] \qquad (3\text{-}19)$$

where $\hat{a}_{gg}$ denotes gravity gradient acceleration vector; $\hat{d}$, the vector (not a unit vector) from the fluid element to the spacecraft geometric center; $\hat{r}_c$, a unit vector from the spacecraft geometric center to the center of the Earth; and n, the orbit rate (see Figure 2).

It is assumed that the gravity gradient exerted on the geometrical center of the spacecraft orbiting around the Earth on its specified orbit is zero. In other words, all the gravity acceleration exerted on the spacecraft is nothing but the gravity gradient acceleration which is defined in Equation (3-19). In this study, we are interested in investigating how gravity gradient acceleration affects the dynamical behaviors of cryogenic fluid elements of helium.

For the convenience of mathematical calculation, let us describe all the parameters involved in Equation (3-19) in terms of cartesian coordinates. In order to match with the computer simulation, mathematical derivation are considered in the first quadrant. Figure 2 illustrates the geometrical relationship of the parameters shown in Equation (3-19).

Let us consider the fluid element of interests, m, located at (r, θ, z) in cylindrical coordinates and at (x, y, z) in cartesian coordinates. The origin of the two coordinate systems is located at the center bottom of the dewar tank. The slew and/or spinning motions, mentioned earlier, are executed at the spacecraft mass center with cartesian coordinate (x", y", z"). The geometry center or the spacecraft mass center is located at z = L_c. As $|\hat{d}|$ (not an unit vector) is much smaller than the distance between the location of the AXAF-S spacecraft geometric center to the center of the Earth, $\hat{r}_c$ (an unit vector) through the AXAF-S geometric center and $\hat{r}_c$ (an unit vector) through the fluid element, m, is basically the same. Assume that vector $\hat{r}_c$ lies in the x-z plane of the cartesian coordinate.

Radial vector $\hat{r}_c$ with the modification of slew and/or spinning motions along the x"-, y"-, z"-axes have been derived in Equations (3-3) to (3-8). Based on the relationship between coordinates (x, y, z) and (x", y", z")

$$\begin{bmatrix} x \\ y \\ z-L_c \end{bmatrix} = \begin{bmatrix} 1 & 0 & 0 \\ 0 & 1 & 0 \\ 0 & 0 & 1 \end{bmatrix} \begin{bmatrix} x'' \\ y'' \\ z'' \end{bmatrix} \tag{3-20}$$

Vector $\hat{d}$ in (x, y, z) coordinate becomes

$$\hat{d} = [-r\cos\theta, -r\sin\theta, -(z-L_c)] \tag{3-21}$$

Substituting Equations (3-4) and (3-21) in (3-19), non-inertia frame expression of gravity gradient acceleration with spinning motion in z-axis becomes

$$\begin{bmatrix} a_{gg,x} \\ a_{gg,y} \\ a_{gg,z} \end{bmatrix}_{spinning\ in\ z\text{-}axis} = -n^2 \begin{bmatrix} 3[-r\sin\psi_{Eo}\cos(\theta+\omega_z t)+(z-L_c)\cos\psi_{Eo}]\sin\psi_{Eo}\cos\omega_z t+r\cos\theta \\ -3[-r\sin\psi_{Eo}\cos(\theta+\omega_z t)+(z-L_c)\cos\psi_{Eo}]\sin\psi_{Eo}\sin\omega_z t+r\sin\theta \\ -3[-r\sin\psi_{Eo}\cos(\theta+\omega_z t)+(z-L_c)\cos\psi_{Eo}]\cos\psi_{Eo}+(z-L_c) \end{bmatrix} \quad (3\text{-}22)$$

Substituting Equations (3-5) and (3-21) in (3-19), non-inertia frame expressions of gravity gradient acceleration with slew motion in y-axis becomes

$$\begin{bmatrix} a_{gg,x} \\ a_{gg,y} \\ a_{gg,z} \end{bmatrix}_{slew\ in\ y\text{-}axis} = -n^2 \begin{bmatrix} 3[-r\sin\psi\cos\theta+\cos\psi(z-L_c)]\sin\psi+r\cos\theta \\ r\sin\theta \\ -3[-r\sin\psi\cos\theta+\cos\psi(z-L_c)]\cos\psi+(z-L_c) \end{bmatrix} \quad (3\text{-}23)$$

where $\psi_E = \psi_{Eo} + \omega_y t$.

Substituting Equations (3-6) and (3-21) in (3-19), non-inertia frame expressions of gravity gradient acceleration with slew motion in x-axis becomes

$$\begin{bmatrix} a_{gg,x} \\ a_{gg,y} \\ a_{gg,z} \end{bmatrix}_{slew\ in\ x\text{-}axis} = -n^2 \begin{bmatrix} 3\{-r\cos\theta\sin\psi_{Eo}+\cos\psi_{Eo}[r\sin\omega_x t\sin\theta+\cos\omega_x t(z-L_c)]\}\sin\psi_{Eo}+r\cos\theta \\ -3\{-r\cos\theta\sin\psi_{Eo}+\cos\psi_{Eo})]\sin\omega_x t\sin\theta+\cos\omega_x t(z-L_c)]\}\cos\psi_{Eo}\sin\omega_x t+r\sin\theta \\ -3\{-r\cos\theta\sin\psi_{Eo}+\cos\psi_{Eo}[r\sin\omega_x t\sin\theta+\cos\omega_x t(z-L_c)]\}\cos\psi_{Eo}\cos\omega_x t+(z-L_c) \end{bmatrix} \quad (3\text{-}24)$$

The relationship for the coordinate transformation from cartesian to cylindrical coordinates for any vector $\hat{F}$ (such as velocity or force vectors) in non-inertia frame of spacecraft bound coordinate can be shown as

$$\begin{bmatrix} F_r \\ F_\theta \\ F_z \end{bmatrix} = \begin{bmatrix} \cos\theta & \sin\theta & 0 \\ -\sin\theta & \cos\theta & 0 \\ 0 & 0 & 1 \end{bmatrix} \begin{bmatrix} F_x \\ F_y \\ F_z \end{bmatrix} \quad (3\text{-}25)$$

Thus, the gravity gradient acceleration located at (r, θ, z) can be computed from that located at (x, y, z), shown in Equations (3-22) to (3-24), from the following relation:

$$\hat{a}_{gg} = \begin{bmatrix} a_{gg,r} \\ a_{gg,\theta} \\ a_{gg,z} \end{bmatrix} = \begin{bmatrix} \cos\theta & \sin\theta & 0 \\ -\sin\theta & \cos\theta & 0 \\ 0 & 0 & 1 \end{bmatrix} \begin{bmatrix} a_{gg,x} \\ a_{gg,y} \\ a_{gg,z} \end{bmatrix} \quad (3\text{-}26)$$

(E) Jitter Accelerations

In addition to gravity gradient acceleration acting on the fluid element of on-orbit spacecraft fluid systems, there is another acceleration of gravity jitter also exerted forces on the fluid systems. The sources of residual acceleration of gravity jitter range from slew motion of spacecraft, atmospheric drag on the spacecraft, background gravity, spacecraft attitude motions arising from machinery vibrations, thruster firings, crew motion, etc., are also capable for the excitation of slosh waves in spacecraft fluid systems (Kamotani et al., 1981; Hung and Shyu, 1991 a,b,c; 1992 a,b,c; 1993 a,b,c; Hung et al., 1992 a,b,c).

Among all of the varieties of jitter accelerations listed, accelerations induced by slew motion of the spacecraft dominate the forces activated on the spacecraft fluid systems. Two coordinate systems (cylindrical and cartesian) chosen in this study are (r, θ, z) with corresponding velocity components (u_r, u_θ, u_z) for cylindrical, and (x, y, z) with corresponding velocity components (u_x, u_y, u_z) for cartesian coordinates. The origin of these two coordinates are located at the central bottom of the dewar tank, as shown in Figure 6. The spacecraft center of mass, or the geometric center of the spacecraft is located at $(x_c, y_c, z_c) = (0, 0, L_c)$. The relationships of the coordinate, velocity and the force between cartesian and cylindrical coordinates are

$$\begin{bmatrix} x \\ y \\ z \end{bmatrix} = \begin{bmatrix} \cos\theta & 0 & 0 \\ \sin\theta & 0 & 0 \\ 0 & 0 & 1 \end{bmatrix} \begin{bmatrix} r \\ \theta \\ z \end{bmatrix} \tag{3-27}$$

$$\begin{bmatrix} u_x \\ u_y \\ u_z \end{bmatrix} = \begin{bmatrix} \cos\theta & -\sin\theta & 0 \\ \sin\theta & \cos\theta & 0 \\ 0 & 0 & 1 \end{bmatrix} \begin{bmatrix} u_r \\ u_\theta \\ u_z \end{bmatrix} \tag{3-28}$$

$$\begin{bmatrix} F_r \\ F_\theta \\ F_z \end{bmatrix} = \begin{bmatrix} \cos\theta & \sin\theta & 0 \\ -\sin\theta & \cos\theta & 0 \\ 0 & 0 & 1 \end{bmatrix} \begin{bmatrix} F_x \\ F_y \\ F_z \end{bmatrix} \tag{3-29}$$

In the derivation of acceleration induced by the slew motion of spacecraft, the coordinate system (x", y", z") is fixed at the spacecraft center of the mass. The relationships of the coordinate, velocity and acceleration between expressions with the origin located at the spacecraft center of the mass (x", y", z") and origin located at the center bottom of the dewar tank (x, y, z) are

$$\begin{bmatrix} R_x \\ R_y \\ R_z \end{bmatrix} = \begin{bmatrix} x \\ y \\ z-L_c \end{bmatrix} = \begin{bmatrix} \cos\theta & 0 & 0 \\ \sin\theta & 0 & 0 \\ 0 & 0 & 1 \end{bmatrix} \begin{bmatrix} r \\ \theta \\ z-L_c \end{bmatrix} \tag{3-30}$$

$$\begin{bmatrix} V_x \\ V_y \\ V_z \end{bmatrix} = \begin{bmatrix} u_x \\ u_y \\ u_z \end{bmatrix} = \begin{bmatrix} \cos\theta & -\sin\theta & 0 \\ \sin\theta & \cos\theta & 0 \\ 0 & 0 & 1 \end{bmatrix} \begin{bmatrix} u_r \\ u_\theta \\ u_z \end{bmatrix} \tag{3-31}$$

$$\begin{bmatrix} \ddot{R}_x \\ \ddot{R}_y \\ \ddot{R}_z \end{bmatrix}_{slew} = \begin{bmatrix} F_x \\ F_y \\ F_z \end{bmatrix}_{slew} = \begin{bmatrix} \cos\theta & \sin\theta & 0 \\ -\sin\theta & \cos\theta & 0 \\ 0 & 0 & 1 \end{bmatrix}^{-1} \begin{bmatrix} F_r \\ F_\theta \\ F_z \end{bmatrix}_{slew} \tag{3-32}$$

$$\begin{bmatrix} F_r \\ F_\theta \\ F_z \end{bmatrix}_{slew} = \begin{bmatrix} \cos\theta & \sin\theta & 0 \\ -\sin\theta & \cos\theta & 0 \\ 0 & 0 & 1 \end{bmatrix} \begin{bmatrix} F_x \\ F_y \\ F_z \end{bmatrix}_{slew} \tag{3-33}$$

A detailed expression of $[\ddot{R}_x, \ddot{R}_y, \ddot{R}_z]_{slew}$ are shown in Equation (3-13) of this report. Jitter acceleration is a summation of acceleration induced by slew motion and others, such as atmospheric drag on the spacecraft, spacecraft attitude motions arising from machinery vibration, thruster firing, crew motion, etc. Thus, jitter acceleration can be expressed as

where f is the jitter frequency (Hz) imposed on the fluid systems of the

$$\hat{a}_{gj} = \begin{bmatrix} a_{gj,r} \\ a_{gj,\theta} \\ a_{gj,z} \end{bmatrix}_{slew} + \begin{bmatrix} a_{gj,r} \\ a_{gj,\theta} \\ a_{gj,z} \end{bmatrix}_{others} = -\begin{bmatrix} F_r \\ F_\theta \\ F_z \end{bmatrix}_{slew} - \begin{bmatrix} F_r \\ F_\theta \\ F_z \end{bmatrix}_{others} \{\, 1 + \frac{1}{2}\sin(2\pi f t) \,\}$$

$$= -\begin{bmatrix} \cos\theta & \sin\theta & 0 \\ -\sin\theta & \cos\theta & 0 \\ 0 & 0 & 1 \end{bmatrix} \begin{bmatrix} F_x \\ F_y \\ F_z \end{bmatrix}_{slew} - \begin{bmatrix} F_r \\ F_\theta \\ F_z \end{bmatrix}_{others} \{\, 1 + \frac{1}{2}\sin(2\pi f t) \,\} \qquad (3\text{-}34)$$

spacecraft.

IV. Non-Inertia Frame Mathematical Formulation of Fundamental Equations

Dynamical behavior of fluid elements inside the on-orbit spacecraft fluid systems are strongly modified by the gravity gradient and gravity jitter accelerations. In order to accommodate the impact of gravity gradient acceleration, in particular, on the on-orbit fluid motion, one has to consider non-inertia frame of the spacecraft bound coordinate rather than adopting inertia frame coordinate used in ordinary fluid mechanics formulation.

Consider a closed circular cylindrical dewar of radius, a, with height, L, which is partially filled with cryogenic liquid helium, and rest of the ullage is filled with a helium vapor. Angular velocity of rotating cylinder is ω. Density and viscosity of liquid helium and helium vapor are ρ_L, μ_L, ρ_v, and μ_v, respectively (Mason, 1978). Let us use cylindrical coordinates (r, θ, z), with corresponding velocity components (u, v, w), and corresponding residual gravity acceleration, such as gravity gradient components ($a_{gg,r}$, $a_{gg,\theta}$, $a_{gg,z}$) and gravity jitter components ($a_{gj,r}$, $a_{gj,\theta}$, $a_{gj,z}$). In the derivation of the governing equations, accelerations induced by the spinning motion of the spacecraft is included in the formulation. The rest of the acceleration such as slew motion, atmospheric drag on the spacecraft, spacecraft attitude motions arising from machinery vibrations, thruster firing and others, are included in the jitter acceleration, shown in Equation (3-34). The governing equations for non-inertia frame of spacecraft bound coordinates can be shown as follows:

(A) Continuity Equation

$$\frac{1}{r}\frac{\partial}{\partial r}(ru)+\frac{1}{r}\frac{\partial v}{\partial\theta}+\frac{\partial w}{\partial z}=0 \tag{4-1}$$

(B) Momentum Equations

$$\rho\left(\frac{\partial u}{\partial t}+u\frac{\partial u}{\partial r}+\frac{v}{r}\frac{\partial u}{\partial\theta}-\frac{v^2}{r}+w\frac{\partial u}{\partial z}\right)=-\frac{\partial p}{\partial r}+2\rho\omega_z v+\rho\left(a_{gj,r}+a_{gg,r}\right)+\rho r\omega_z^2$$

$$+\mu\left(\nabla^2 u-\frac{u}{r^2}-\frac{2}{r^2}\frac{\partial v}{\partial\theta}\right) \tag{4-2}$$

$$\rho\left(\frac{\partial v}{\partial t}+u\frac{\partial v}{\partial r}+\frac{v}{r}\frac{\partial v}{\partial\theta}+\frac{uv}{r}+w\frac{\partial v}{\partial z}\right)=-\frac{1}{r}\frac{\partial p}{\partial\theta}\ -2\rho\omega_z u+\rho\left(a_{gj,\theta}+a_{gg,\theta}\right)-\rho r\dot{\omega}_z$$

$$+\mu\left(\nabla^2 v-\frac{v}{r^2}+\frac{2}{r^2}\frac{\partial u}{\partial\theta}\right) \tag{4-3}$$

$$\rho\left(\frac{\partial w}{\partial t}+u\frac{\partial w}{\partial r}+\frac{v}{r}\frac{\partial w}{\partial\theta}+w\frac{\partial w}{\partial z}\right)=-\frac{\partial p}{\partial z}+\rho\left(a_{gj,z}+a_{gg,z}\right)+\mu\nabla^2 w \tag{4-4}$$

where

$$\nabla^2=\frac{1}{r}\frac{\partial}{\partial r}\left(r\frac{\partial}{\partial r}\right)+\frac{1}{r^2}\frac{\partial^2}{\partial\theta^2}+\frac{\partial^2}{\partial z^2} \tag{4-5}$$

In these formulations, $2\omega_z v$ and $2\omega_z u$ are the Coriolis acceleration, $r\omega_z^2$ is the centrifugal acceleration, and $r\dot{\omega}_z$ is the angular acceleration induced by the spinning motion of the spacecraft.

In the computation of fluid forces, moment, viscous stress and angular momentum acting on the container wall of the spacecraft, one has to consider those forces and moment in the inertia frame rather than the non-inertia frame, in particular for the case of the spinning motion in the z-axis. To show an example, one has to transform those vectors from the non-inertia frame to the inertia frame for the case of spinning motion in the z-axis.

$$\begin{bmatrix} F'_x \\ F'_y \\ F'_z \end{bmatrix} = \begin{bmatrix} \cos\omega_z t & -\sin\omega_z t & 0 \\ \sin\omega_z t & \cos\omega_z t & 0 \\ 0 & 0 & 1 \end{bmatrix} \begin{bmatrix} F_x \\ F_y \\ F_z \end{bmatrix} \qquad (4-6)$$

where prime symbol denotes vectors in the inertia frame while those parameters without the prime symbol indicate vectors in the non-inertia frame.

V. Initial and Boundary Conditions of Spacecraft Fluid System in Microgravity Environment

Governing equations of the fluid motion in on-orbit spacecraft fluid systems for non-inertia frame of spacecraft bound coordinates have been illustrated in Equations (4-1) to (4-6). These equations shall be combined with the characteristics of gravity gradient and gravity jitter accelerations as formulated in Equations (3-1) to (3-34). Initial and boundary conditions shall be introduced to accommodate solving fluid motion in on-orbit spacecraft fluid system for non-inertia frame coordinate (Hung et al., 1990 a,b,c; 1991 a,b,c,d,e,f,g,h,i,j).

Let the profile of the interface between gaseous and liquid fluids be given by:

$$\eta(t, r, \theta, z) = 0 \qquad (5-1)$$

The initial condition of the profile of the interface between gaseous and liquid fluids at $t = t_o$ is assigned explicitly, and is given by:

$$\eta(t = t_o, r, \theta, z) = 0 \qquad (5-2)$$

A set of boundary conditions has to be supplied for solving the equations. These initial interface profiles used in this study have been given explicitly through the steady state computations made by Hung and Leslie (1988) and Hung et al (1989 a,b,c,d) which were checked by the experiments carried out by Leslie

(1985). These boundary conditions are as follows:

(1) Along the container wall, the following three boundary conditions apply:

(a) Interface between solid and liquid fluid: No-penetration and no-slip conditions assure that both the tangential and the normal components of the liquid velocity along the solid walls will vanish.

(b) Interface between solid and gaseous (vapor) fluid: Similar no-penetration and no-slip conditions as that shown for interface between solid and liquid fluid will apply.

(c) At the location of solid-liquid-gaseous (vapor) three phases interface: No-penetration, but not no-slip condition apply. This will assure that normal components of liquid and vapor velocities along the solid wall vanish, and allow a slipping flow of liquid and vapor fluids along the solid wall at three phase interface location. The velocity of slipping flow at this location is governed by the adhesive forces between fluids (liquid and gaseous) and solid walls. Also, at this location of three phase interface, a constant contact angle is present in which the behaviors of wet or dry contacts are determined by Coulomb interaction between the fluids (liquid and vapor) and the surface phenomena (material and roughness) of solid walls.

(2) Along the interface between the liquid and gaseous fluids, the following two conditions apply:

(a) Kinematic surface boundary condition: The liquid (or gaseous) surface moves with the liquid (or gas) which implies

$$\frac{D\eta}{Dt}=0\text{, or}$$

$$\frac{\partial\eta}{\partial t}+u\frac{\partial\eta}{\partial r}+\frac{v}{r}\frac{\partial\eta}{\partial\theta}+w\frac{\partial\eta}{\partial z}=0 \qquad (5\text{-}3)$$

$$\text{on } \eta(t=t_\alpha, r, \theta, z)$$

(b) Interface stress condition: Across the liquid-vapor interface, the stress must be continuous. Based on Landu and Lifshitz (1959), the stress across the liquid-vapor interface can be expressed as

$$(P_G-P_L)n_i-[(\tau_{ij})_G-(\tau_{ij})_L]n_j=\sigma\left(\frac{1}{R_1}+\frac{1}{R_2}\right)n_i \qquad (5\text{-}4)$$

where R_1 and R_2 are the radius of curvatures of two major axes at the point of interests on the surface of the liquid-vapor interface.

The expressions of radius of curvatures R_1 and R_2 in cylindrical coordinates from differential geometry can be shown as

$$\frac{1}{R_1}+\frac{1}{R_2}=\frac{EN-2FM+GL}{EG-F^2} \qquad (5\text{-}5)$$

where the relationship of cartesian and cylindrical coordinates for the curved surface of liquid-vapor interface is

$$\begin{bmatrix}x\\y\\z\end{bmatrix}=\begin{bmatrix}r\cos\theta\\r\sin\theta\\H(t_\alpha,r,\theta)\end{bmatrix} \qquad (5\text{-}6)$$

Here, the configuration of the liquid-vapor interface is $z = H(t = t_\alpha, r, \theta)$;

$$E=\left(\frac{\partial x}{\partial r}\right)^2+\left(\frac{\partial y}{\partial r}\right)^2+\left(\frac{\partial z}{\partial r}\right)^2 \qquad (5\text{-}7)$$

$$F=\frac{\partial x}{\partial r}\frac{\partial x}{\partial\theta}+\frac{\partial y}{\partial r}\frac{\partial y}{\partial\theta}+\frac{\partial z}{\partial r}\frac{\partial z}{\partial\theta} \qquad (5\text{-}8)$$

where,

$$G = \left(\frac{\partial x}{\partial \theta}\right)^2 + \left(\frac{\partial y}{\partial \theta}\right)^2 + \left(\frac{\partial z}{\partial \theta}\right)^2$$

$$L = \frac{1}{(EG-F^2)^{\frac{1}{2}}} \begin{bmatrix} x''_{rr} & y''_{rr} & z''_{rr} \\ x'_r & y'_r & z'_r \\ x'_\theta & y'_\theta & z'_\theta \end{bmatrix} \tag{5-9}$$

$$M = \frac{1}{(EG-F^2)^{\frac{1}{2}}} \begin{bmatrix} x''_{r\theta} & y''_{r\theta} & z''_{r\theta} \\ x'_r & y'_r & z'_r \\ x'_\theta & y'_\theta & z'_\theta \end{bmatrix} \tag{5-10}$$

$$N = \frac{1}{(EG-F^2)^{\frac{1}{2}}} \begin{bmatrix} x''_{\theta\theta} & y''_{\theta\theta} & z''_{\theta\theta} \\ x'_r & y'_r & z'_r \\ x'_\theta & y'_\theta & z'_\theta \end{bmatrix} \tag{5-11}$$

$$[x'_r, y'_r, z'_r] = \frac{\partial}{\partial r}[x, y, z,] \tag{5-12}$$

$$[x'_\theta, y'_\theta, z'_\theta] = \frac{\partial}{\partial \theta}[x, y, z] \tag{5-13}$$

and,

$$\begin{bmatrix} x''_{rr} & y''_{rr} & z''_{rr} \\ x''_{r\theta} & y''_{r\theta} & z''_{r\theta} \\ x''_{\theta\theta} & y''_{\theta\theta} & z''_{\theta\theta} \end{bmatrix} = \begin{bmatrix} \dfrac{\partial^2}{\partial r^2} \\ \dfrac{\partial^2}{\partial r \partial \theta} \\ \dfrac{\partial^2}{\partial \theta^2} \end{bmatrix} [x, y, z] \tag{5-14}$$

Simplifying Equations (5-7) to (5-11), one obtains

$$EG-F^2 = r^2(1 + H_r{}^2 + \frac{1}{r^2}H_\theta{}^2) = r^2D^2$$

$$E = 1 + H_r^2, \; F = H_r H_\theta, \; G = r^2 + H_\theta^2$$

$$[H_r, H_\theta] = [\frac{\partial}{\partial r}, \frac{\partial}{\partial \theta}] H$$

$$L = \frac{H_{rr}}{D}, \; M = \frac{(-H_\theta + rH_{r\theta})}{rD}, \; N = \frac{(r^2 H_r + rH_{\theta\theta})}{rD}, \text{ and}$$

$$D = (1 + H_r^2 + \frac{1}{r^2} H_\theta^2)^{\frac{1}{2}}$$

Substituting these relations to Equation (5-4), the radius of the curvature on the curved surface of the configuration of liquid-vapor interface in cylindrical coordinates can be expressed as follows:

$$\frac{1}{R_1} + \frac{1}{R_2} = -\frac{1}{r} [\frac{\partial}{\partial r} (r \frac{H_r}{D}) + \frac{\partial}{\partial \theta} (\frac{H_\theta}{rD})] \qquad (5\text{-}15)$$

Here, in Equations (5-4) and (5-15)

$$\tau_{ij} = \mu (\frac{\partial u_i}{\partial x_j} + \frac{\partial u_j}{\partial x_i} + \frac{2}{3} \frac{\partial u_k}{\partial x_k} \delta_{ij}) + \zeta \frac{\partial u_k}{\partial x_k} \delta_{ij}$$

is the viscous stress tensor; μ, the viscous coefficient of the first kind; ζ, the viscous coefficient of the second kind; P, the pressure; σ, the surface tension of the liquid-vapor interface; and n_j, the unit vector normal to the interface; and δ_{ij}, the Kronecker's delta function. Also, subscripts G and L denote conditions at gaseous and liquids fluids, respectively, across the liquid-vapor interface.

The fluid stresses across the liquid-vapor interface can be decomposed to the components normal (n_i, a unit vector) and tangential (t_i, a unit vector) to the interface. For the component tangential to the interface, one can take a dot product of a unit vector tangential to the interface, t_i, to Equations (5-4) and

(5-15), which leads to

$$[(\tau_{ij}t_in_j)]_L=[(\tau_{ij}t_in_j)]_G \tag{5-16}$$

since $n_it_i = 0$.

For the component normal to the interface, one can also take a dot product of a unit vector normal to the interface, n_i, to Equations (5-4) and (5-15), which leads to

$$P_G - P_L - [(\tau_{ij}n_in_j)_G - (\tau_{ij}n_in_j)_L] = -\frac{\sigma}{r}[\frac{\partial}{\partial r}(\frac{rH_r}{D}) + \frac{\partial}{\partial\theta}(\frac{H_\theta}{rD})] \tag{5-17}$$

For components normal to the interface along the (r, θ, z) directions in cylindrical coordinates can be obtained by taking dot products of n_r, n_θ, n_z separately to Equations (5-4) and (5-15), which are expressed as

$$(P_G - P_L)\begin{bmatrix} n_r \\ n_\theta \\ n_z \end{bmatrix} - \begin{bmatrix} (\tau_{rj}n_j)_G - (\tau_{rj}n_j)_L \\ (\tau_{\theta j}n_j)_G - (\tau_{\theta j}n_j)_L \\ (\tau_{zj}n_j)_G - (\tau_{zj}n_j)_L \end{bmatrix}$$

$$= -\frac{\sigma}{r}[\frac{\partial}{\partial r}(\frac{rH_r}{D}) + \frac{\partial}{\partial\theta}(\frac{H_\theta}{rD})]\begin{bmatrix} n_r \\ n_\theta \\ n_z \end{bmatrix} \tag{5-18}$$

where (n_r, n_θ, n_z) is the unit vector normal to the interface in cylindrical coordinates (r, θ, z).

For a special case of axial symmetry, component normal to the interface, shown in Equation (5-17), can be simplified and becomes

$$P_G - P_L - (\tau_{ij}n_in_j)_G + (\tau_{ij}n_in_j)_L$$

$$= -\frac{\sigma}{r}\frac{d}{dr}[\frac{r\phi}{(1 + \phi^2)^{\frac{1}{2}}}] \tag{5-19}$$

since $\partial/\partial\theta = 0$, $H_r = \partial H/\partial r = dz/dr = \phi$, $H_\theta = 0$ and $D = (1 + \phi^2)^{1/2}$ for the case of axial symmetry.

VI. Characteristics of Slosh Wave Induced Fluctuations in Fluid Moment and Angular Momentum

Slosh wave induced fluctuations in the fluid system of the rotating dewar introduce time-dependent disturbances in moment and angular momentum of spacecraft fluid system. In this study, there are induced angular velocities along the yawing, pitching and rolling axes due to the fluid motion inside rotating container. These angular velocities in yawing, pitching and rolling axes, caused by the fluid flows in a partially liquid-filled container, readjust the angular velocity in rolling axis.

In order to accommodate the spacecraft dynamics of yawing, pitching and rolling, cylindrical coordinates (shown in Figure 2) of rotating container is transformed into cartesian coordinates based on $(x, y, z) = (r\cos\theta, r\mathrm{sini}\theta, z)$ with corresponding velocity components $(V_x, V_y, V_z) = (u\cos\theta - v\sin\theta, u\sin\theta + v\cos\theta, w)$. If spacecraft is rotated with respect to mass center at (r_c, θ_c, z_c) in cylindrical coordinates, location of mass center in cartesian coordinates becomes $(x_c, y_c, z_c) = (r_c\cos\theta_c, r_c\sin\theta_c, z_c)$. Induced angular velocities $(\tilde{\omega}_x, \tilde{\omega}_y, \tilde{\omega}_z)$ in cartesian coordinates becomes

$$\begin{bmatrix} \tilde{\omega}_x \\ \tilde{\omega}_y \\ \tilde{\omega}_z \end{bmatrix} = \begin{bmatrix} K_{xx} & -K_{xy} & K_{xz} \\ K_{yx} & K_{yy} & -K_{yz} \\ -K_{zx} & K_{zy} & K_{zz} \end{bmatrix} \begin{bmatrix} V_x \\ V_y \\ V_z \end{bmatrix} \tag{6-1}$$

where

$$K_{xx} = K_{yy} = K_{zz} = 0$$

$$\begin{bmatrix} K_{xy} \\ K_{yx} \end{bmatrix} = (z-z_c) \begin{bmatrix} [(y-y_c)^2+(z-z_c)^2]^{-1} \\ [(x-x_c)^2+(z-z_c)^2]^{-1} \end{bmatrix}$$

$$\begin{bmatrix} K_{xz} \\ K_{zx} \end{bmatrix} = (y-y_c) \begin{bmatrix} [(y-y_c)^2+(z-z_c)^2]^{-1} \\ [(x-x_c)^2+(y-y_c)^2]^{-1} \end{bmatrix}$$

$$\begin{bmatrix} K_{yz} \\ K_{zy} \end{bmatrix} = (x-x_c) \begin{bmatrix} [(x-x_c)^2+(z-z_c)^2]^{-1} \\ [(x-x_c)^2+(y-y_c)^2]^{-1} \end{bmatrix}$$

As the velocity components are given by

$$\begin{bmatrix} V_x \\ V_y \\ V_z \end{bmatrix} = \begin{bmatrix} \cos\theta & -\sin\theta & 0 \\ \sin\theta & \cos\theta & 0 \\ 0 & 0 & 1 \end{bmatrix} \begin{bmatrix} u \\ v \\ w \end{bmatrix}, \tag{6-2}$$

the relationship between the components of induced angular velocity and flow velocity in cylindrical coordinates can be expressed in the following formulation:

$$\begin{bmatrix} \tilde{\omega}_x \\ \tilde{\omega}_y \\ \tilde{\omega}_z \end{bmatrix} = \begin{bmatrix} \tilde{K}_{xx} & \tilde{K}_{xy} & \tilde{K}_{xz} \\ \tilde{K}_{yx} & \tilde{K}_{yy} & \tilde{K}_{yz} \\ \tilde{K}_{zx} & \tilde{K}_{zy} & \tilde{K}_{zz} \end{bmatrix} \begin{bmatrix} u \\ v \\ w \end{bmatrix} \tag{6-3}$$

where

$$\begin{bmatrix} \tilde{K}_{xx} \\ \tilde{K}_{xy} \\ \tilde{K}_{xz} \end{bmatrix} = \begin{bmatrix} -(z-z_c)\sin\theta \\ -(z-z_c)\cos\theta \\ r\sin\theta - r_c\sin\theta_c \end{bmatrix} [(r\sin\theta - r_c\sin\theta_c)^2+(z-z_c)^2]^{-1}$$

$$\begin{bmatrix} \tilde{K}_{yx} \\ \tilde{K}_{yy} \\ \tilde{K}_{yz} \end{bmatrix} = \begin{bmatrix} (z-z_c)\cos\theta \\ -(z-z_c)\sin\theta \\ -(r\cos\theta - r_c\cos\theta_c) \end{bmatrix} [(r\cos\theta - r_c\cos\theta_c)^2+(z-z_c)^2]^{-1}$$

$$\begin{bmatrix} \tilde{K}_{zx} \\ \tilde{K}_{zy} \\ \tilde{K}_{zz} \end{bmatrix} = \begin{bmatrix} -r_c \sin(\theta-\theta_c) \\ r - r_c \cos(\theta-\theta_c) \\ 0 \end{bmatrix} [r^2 + r_c^2 - 2 r r_c \cos(\theta-\theta_c)]^{-1}$$

For the case of AXAF-S Spacecraft, axis of slew motion is always fixed at the point of spacecraft center of mass which is located at the mass center of the spacecraft at (0, 0, L_c), where L_c is the height of axis of slew motion (see Figure 1). By using the computed results of induced angular velocity shown in Equation (6-3), one can compute the angular momentum (H_x, H_y, H_z) as follows:

$$\begin{bmatrix} H_x \\ H_y \\ H_z \end{bmatrix} = \rho_v \left\{ \iiint \begin{bmatrix} \tilde{I}_{xx} & -\tilde{I}_{xy} & -\tilde{I}_{xz} \\ -\tilde{I}_{yx} & \tilde{I}_{yy} & -\tilde{I}_{yz} \\ -\tilde{I}_{zx} & -\tilde{I}_{zy} & \tilde{I}_{zz} \end{bmatrix} \begin{bmatrix} \tilde{\omega}_x \\ \tilde{\omega}_y \\ \tilde{\omega}_z \end{bmatrix} + \begin{bmatrix} r\sin\theta v_{c,z} & -(z-L_c) v_{c,y} \\ (z-L_c) v_{c,x} & -r\cos\theta v_{c,z} \\ r\cos\theta v_{c,y} & -r\sin\theta v_{c,x} \end{bmatrix} \right\}_{vapor} r d\theta dr dz$$

$$+ \rho_L \left\{ \iiint \begin{bmatrix} \tilde{I}_{xx} & -\tilde{I}_{xy} & -\tilde{I}_{xz} \\ -\tilde{I}_{yx} & \tilde{I}_{yy} & -\tilde{I}_{yz} \\ -\tilde{I}_{zx} & -\tilde{I}_{zy} & \tilde{I}_{zz} \end{bmatrix} \begin{bmatrix} \tilde{\omega}_x \\ \tilde{\omega}_y \\ \tilde{\omega}_z \end{bmatrix} + \begin{bmatrix} r\sin\theta v_{c,z} & -(z-L_c) v_{c,y} \\ (z-L_c) v_{c,x} & -r\cos\theta v_{c,z} \\ r\cos\theta v_{c,y} & -r\sin\theta v_{c,x} \end{bmatrix} \right\}_{liquid} r d\theta dr dz \qquad (6\text{-}4)$$

where

$\tilde{I}_{xx} = r^2\sin^2\theta + (z - L_c)^2$; $\tilde{I}_{xy} = \tilde{I}_{yx} = r^2\sin\theta\cos\theta$

$\tilde{I}_{yy} = r^2\cos^2\theta + (z - L_c)^2$; $\tilde{I}_{xz} = \tilde{I}_{zx} = r(z - L_c)\cos\theta$

$\tilde{I}_{zz} = r^2$; $\tilde{I}_{yz} = \tilde{I}_{zy} = r(z - L_c)\sin\theta$

and

$$\begin{bmatrix} v_{c,x} \\ v_{c,y} \\ v_{c,z} \end{bmatrix} = \begin{bmatrix} \cos\theta & -\sin\theta & 0 \\ \sin\theta & \cos\theta & 0 \\ 0 & 0 & 1 \end{bmatrix} \begin{bmatrix} u_c \\ v_c \\ w_c \end{bmatrix}$$

The moment of spacecraft can be computed from the time rate of change of the angular momentum, i.e.,

$$\begin{bmatrix} M_x \\ M_y \\ M_z \end{bmatrix} = \frac{d}{dt} \begin{bmatrix} H_x \\ H_y \\ H_z \end{bmatrix} + \begin{bmatrix} \omega_y H_z & -\omega_z H_y \\ \omega_z H_x & -\omega_x H_y \\ \omega_x H_y & -\omega_y H_x \end{bmatrix} \tag{6-5}$$

where $\omega_i = (\omega_x, \omega_y, \omega_z)$ denotes pitching, yawing and rolling angular velocities of spacecraft in inertia frame.

VII. Mathematical Formulation of Fluid Stresses and Moment Fluctuations Due to Slosh Waves

For the purpose of considering large amplitude slosh wave activated fluid stresses exerted on the solid walls of the dewar, the fluid stresses are decomposed into the tangential and normal components to the walls which can be expresses as follows:

$$\Pi_t = \mu \left(\frac{\partial u_\alpha}{\partial x_\beta} + \frac{\partial u_\beta}{\partial x_\alpha} \right) \hat{t}_\alpha \hat{n}_\beta \tag{7-1}$$

$$\Pi_n = P\delta_{\alpha\beta} - \mu \left(\frac{\partial u_\alpha}{\partial x_\beta} + \frac{\partial u_\beta}{\partial x_\alpha} \right) \hat{n}_\alpha \hat{n}_\beta \tag{7-2}$$

where Π_t denotes the tangential component of fluid stresses; Π_n, the normal component of fluid stresses; P, the thermodynamic pressure; u_α, fluid velocity in α direction; $\hat{t}_\alpha$, unit vector tangential to the wall; $\hat{n}_\beta$, unit vector normal to the wall; μ, the molecular viscosity coefficient of fluid; and $\delta_{\alpha B}$, the Kronecker's delta function. Subscripts α and β imply the directions of flow fields.

Figures 6(A) and 6(B) show the geometry of GP-B dewar propellant tank in both r-z and r-θ planes, respectively. In order to make the computation of fluid stresses match the geometry of the dewar tank, mathematical formulations have been divided into three sections: (A) Top wall (dome) section, (B) Bottom wall (dome) section, (C) Cylindrical section (including probe section of the inner wall of dewar) and (D) Baffle plates section. There are several plates of baffle inserted in the dewar [see Figure 7(A) and 7(B) for baffle board illustration]. Baffles with the shape of hollow circular plate with an inner radius R_1, and an outer radius R_2 are installed along the probe column of the dewar located at $z = L_i$, where $i = 1, 2, \ldots$, n plates and the thickness of each plate is d.

(A) Top Wall (Dome) Section:

$$(\Pi_t)^{r-z}_{Top\ Wall}=\mu\left(\frac{\partial u}{\partial z}+\frac{\partial w}{\partial r}\right)\cos 2\phi \tag{7-3}$$

$$(\Pi_t)^{r-\theta}_{Top\ Wall}=\mu\left[\left(\frac{1}{r}\frac{\partial u}{\partial \theta}+\frac{\partial v}{\partial r}\right)\cos\phi+\left(\frac{1}{r}\frac{\partial w}{\partial \theta}+\frac{\partial v}{\partial z}\right)\sin\phi\right] \tag{7-4}$$

$$(\Pi_n)_{Top\ Wall}=P+\mu\left(\frac{\partial u}{\partial z}+\frac{\partial w}{\partial r}\right)\sin 2\phi \tag{7-5}$$

(B) Bottom Wall (Dome) Section:

$$(\Pi_t)^{r-z}_{Bottom\ Wall}=\mu\left(\frac{\partial u}{\partial z}+\frac{\partial w}{\partial r}\right)\cos 2\phi \tag{7-6}$$

$$(\Pi_t)^{r-\theta}_{Bottom\ Wall}=\mu\left[\left(\frac{1}{r}\frac{\partial u}{\partial \theta}+\frac{\partial v}{\partial r}\right)\cos\phi-\left(\frac{1}{r}\frac{\partial w}{\partial \theta}+\frac{\partial v}{\partial z}\right)\sin\phi\right] \tag{7-7}$$

$$(\Pi_n)_{Bottom\ Wall}=P-\mu\left(\frac{\partial u}{\partial z}+\frac{\partial w}{\partial r}\right)\sin 2\phi \tag{7-8}$$

(C) Cylindrical Section (including probe section of the inner wall of dewar):

$$(\Pi_t)^{r-z}_{Cylindrical}=\mu\left(\frac{\partial u}{\partial z}+\frac{\partial w}{\partial r}\right) \tag{7-9}$$

$$(\Pi_t)^{r-\theta}_{Cylindrical}=\mu\left(\frac{1}{r}\frac{\partial u}{\partial \theta}+\frac{\partial v}{\partial r}\right) \tag{7-10}$$

$$(\Pi_n)_{Cylindrical} = P \tag{7-11}$$

(D) Baffle Plates Section:

$$(\Pi_t)^{r-z}_{Baffle} = \mu\left(\frac{\partial u}{\partial z} + \frac{\partial w}{\partial r}\right) \tag{7-12}$$

$$(\Pi_t)^{r-\theta}_{Baffle} = \mu\left(\frac{1}{r}\frac{\partial u}{\partial \theta} + \frac{\partial v}{\partial r}\right) \tag{7-13}$$

$$(\Pi_n)_{Baffle} = \pm P \tag{7-14}$$

where ϕ is the azimuth angle of the dome; and $(\Pi_t)^{r-z}$ and $(\Pi_t)^{r-\theta}$ denote tangential stresses in r-z and r-θ planes of the dewar, respectively. Velocity components in cylindrical coordinates of (r, θ, z) are shown as (u, v, w).

The stress distribution shown in Eqs. (7-3) to (7-14) can be integrated with respect to area and obtain the tangential and normal forces on top wall, bottom wall, and cylindrical sections of the dewar.

(A) Top Wall (Dome) Sections:

$$\begin{bmatrix} (F_t)^{r-z} \\ (F_t)^{r-\theta} \\ (F_n) \end{bmatrix}_{Top\ Wall} = \iint \begin{bmatrix} (\Pi_t)^{r-z} \\ (\Pi_t)^{r-\theta} \\ (\Pi_n) \end{bmatrix}_{Top\ Wall} R_d^2 \cos\phi \, d\phi \, d\theta \tag{7-15}$$

(B) Bottom Wall (Dome) Section:

$$\begin{bmatrix} (F_t)^{r-z} \\ (F_t)^{r-\theta} \\ (F_n) \end{bmatrix}_{Bottom\ Wall} = \iint \begin{bmatrix} (\Pi_t)^{r-z} \\ (\Pi_t)^{r-\theta} \\ (\Pi_n) \end{bmatrix}_{Bottom\ Wall} R_d^2 \cos\phi \, d\phi \, d\theta \tag{7-16}$$

(C) Cylindrical Section (including probe section of the inner wall of dewar):

$$\begin{bmatrix} (F_t)^{r-z} \\ (F_t)^{r-\theta} \\ (F_n) \end{bmatrix}_{Cylindrical} = \iint \begin{bmatrix} (\Pi_t)^{r-z} \\ (\Pi_t)^{r-\theta} \\ (\Pi_n) \end{bmatrix}_{Inner\,Cylinder} R_{c1} \, d\theta \, dz$$

$$+\iint \begin{bmatrix} (\Pi_t)^{r-z} \\ (\Pi_t)^{r-\theta} \\ (\Pi_n) \end{bmatrix}_{Outer\,Cylinder} R_{c2} d\theta dz \qquad (7\text{-}17)$$

(D) Baffle Plate Section:

$$\begin{bmatrix} (F_t)^{r-\theta} \\ (F_t)^{r-\theta} \\ (F_n) \end{bmatrix}_{Baffle} = \iint \begin{bmatrix} (\Pi_t)^{r-z} \\ (\Pi_t)^{r-\theta} \\ (\Pi_n) \end{bmatrix}_{Baffle} r dr d\theta \qquad (7\text{-}18)$$

where R_d and ϕ denote the radius and the azimuth angle of the dome section, respectively; and R_{c1} and R_{c2} are the radii of the inner and outer walls of the cylindrical section of the dewar (see Figs. 6 and 7).

In order to accommodate the spacecraft dynamics of pitching, yawing and rolling, cylindrical coordinates (shown in Figs. 6 and 7) of the rotating container is transformed into cartesian coordinates based on $(x, y, z) = (r\cos\theta, r\sin\theta, z)$ with corresponding velocity components $(v_x, v_y, v_z) = (u\cos\theta - v\sin\theta, u\sin\theta + v\cos\theta, w)$. For the case of the AXAF-S spacecraft, the axes of slew motion are always fixed at the mass center of the spacecraft which is located at $(x_c, y_c, z_c) = (0, 0, L_c)$ where L_c is the height of the axis of slew motion (see Figure 4). To fulfill this goal, stress distributions, shown in Eqs. (7-15) to (7-18), have to be recalculated in the (x, y, z) directions (see Figs. 6 and 7).

$$F_x = \left\{ \left[\iint -(\Pi_t)^{r-z}_{Top\ Wall} + \iint (\Pi_t)^{r-z}_{Bottom\ Wall} \right] R_d^2 \cos\phi \cdot \sin\phi \cdot \cos\theta \, d\phi \, d\theta \right\}$$

$$+ \left\{ \left[\iint -(\Pi_t)^{r-\theta}_{Top\ Wall} - \iint (\Pi_t)^{r-\theta}_{Bottom\ Wall} \right] R_d^2 \cos\phi \cdot \sin\theta \, d\phi \, d\theta \right\}$$

$$+ \left\{ \left[\iint (\Pi_n)_{Top\ Wall} + \iint (\Pi_n)_{Bottom\ Wall} \right] R_d^2 \cos^2\phi \cdot \cos\theta \, d\phi \, d\theta \right\}$$

$$+\left\{\left[\iint -(\Pi_t)^{r-\theta}_{InnerCylinder}\sin\theta + \iint (\Pi_n)_{InnerCylinder}\cos\theta\right] R_{c1}d\theta dz\right\}$$

$$+\ \{\ [\iint -(\Pi_t)^{r-\theta}_{Outer\ Cylinder}\ \sin\theta + \iint (\Pi_n)_{Outer\ Cylinder}\cos\theta]\, R_{c2}d\theta dz\ )$$

$$+\sum_i\left\{\left[\iint (\Pi_t)^{r-z}_{Baffle}\cos\theta r dr d\theta + \iint (\Pi_t)^{r-\theta}_{Baffle}\sin\theta r dr d\theta\right]_{z=L_i-\frac{d}{2}}\right\}$$

$$+\sum_i\left\{\left[\iint (\Pi_t)^{r-z}_{Baffle}\cos\theta r dr d\theta + (\Pi_t)^{r-\theta}_{Baffle}\sin\theta r dr d\theta\right]_{z=L_i+\frac{d}{2}}\right\} \qquad (7-19)$$

$$F_y=\left\{\left[\iint -(\Pi_t)^{r-z}_{Top\ Wall} + \iint (\Pi_t)^{r-z}_{Bottom\ Wall}\right] R_d^2\cos\phi\cdot\sin\phi\cdot\sin\theta d\phi d\theta\right\}$$

$$+\left\{\left[\iint (\Pi_t)^{r-\theta}_{Top\ Wall} + \iint (\Pi_t)^{r-\theta}_{Bottom\ Wall}\right] R_d^2\cos\phi\cdot\cos\theta d\phi d\theta\right\}$$

$$+\left\{\left[\iint (\Pi_n)_{Top\ Wall} + \iint (\Pi_n)_{Bottom\ Wall}\right] R_d^2\cos^2\phi\cdot\sin\theta d\phi d\theta\right\}$$

$$+\left\{\left[\iint (\Pi_t)^{r-\theta}_{InnerCylinder}\cos\theta + \iint (\Pi_n)_{InnerCylinder}\sin\theta\right] R_{c1}d\theta dz\right\}$$

$$+\ \{\left[\iint (\Pi_n)^{r-\theta}_{Outer\ Cylinder}\cos\theta + \iint (\Pi_n)_{Outer\ Cylinder}\sin\theta\right] R_{c2}d\theta dz\ \}$$

$$+\sum_i\left\{\left[\iint (\Pi_t)^{r-z}_{Baffle}\sin\theta r dr d\theta + (\Pi_t)^{r-\theta}_{Baffle}\cos\theta r dr d\theta\right]_{z=L_i-\frac{d}{2}}\right\}$$

$$+\sum_i\left\{\left[\iint (\Pi_t)^{r-z}_{Baffle}\sin\theta r dr d\theta + \iint (\Pi_t)^{r-\theta}_{Baffle}\cos\theta r dr d\theta\right]_{z=L_i+\frac{d}{2}}\right\} \qquad (7-20)$$

$$F_z=\left\{\left[\iint (\Pi_t)^{r-z}_{Top\ Wall} + \iint (\Pi_t)^{r-z}_{Bottom\ Wall}\right] R_d^2\cos^2\phi d\phi d\theta\right\} + \ \{[\iint (\Pi_n)_{Top\ Wall}$$

$$+\iint (\Pi_n)_{Bottom\ Wall}]\ R_d^2\cos\phi\cdot\sin\phi d\phi d\theta\} + \left[\iint (\Pi_t)^{r-z}_{InnerCylinder}R_{c1}d\theta dz + \iint (\Pi_t)^{r-z}_{OuterCylinder}R_{c2}d\theta dz\right] \quad (7-21)$$

The moment of stress force acting on the dewar wall of the container can be computed from the cross product of moment arm, [which is the perpendicular distance from the location of proof mass of the spacecraft to the total forces], and the total forces. Components of the moment can be computed from the following formulations:

$$M_x = \Big[\iint (\Pi_t)^{r-z}_{Top\ Wall} + \iint (\Pi_t)^{r-z}_{Bottom\ Wall}\Big]\ R_d^3\cos^3\phi\cdot\sin\theta\, d\phi\, d\theta$$

$$+\Big[\iint (\Pi_n)_{Top\ Wall} + \iint (\Pi_n)_{Bottom\ Wall}\Big]\ R_d^3\cos^2\phi\cdot\sin\phi\cdot\sin\theta\, d\phi\, d\theta$$

$$+\Big[\iint (\Pi_t)^{r-z}_{Inner\ Cylinder} R_{c1}^2\sin\theta\, d\theta\, dz + \iint (\Pi_t)^{r-z}_{Outer\ Cylinder} R_{c2}^2\sin\theta\, d\theta\, dz\Big] + \{\Big[\iint -(\Pi_t)^{r-z}_{Top\ Wall} + \iint (\Pi_t)^{r-z}_{Bottom\ Wall}\Big]$$

$$\cdot (L_c - L_d + R_d\sin\phi) R_d^2\cos\phi\cdot\sin\phi\cdot\sin\theta\, d\phi\, d\theta + [\iint (\Pi_t)^{r-\theta}_{Top\ Wall}$$

$$+\iint (\Pi_t)^{r-\theta}_{Bottom\ Wall}]\,(L_c - L_d + R_d\sin\phi) R_d^2\cos\phi\cdot\cos\theta\, d\phi\, d\theta + [\iint (\Pi_n)_{Top\ Wall}$$

$$+\iint (\Pi_n)_{Bottom\ Wall}]\ \ (L_c - L_d + R_d\sin\psi)\ R_d{}^2\cos^2\psi\cdot\sin\theta\, d\psi\, d\theta$$

$$+\ \{\ \Big[\iint (\Pi_t)^{r-\theta}_{Inner\,Cylinder}\cos\theta + \iint (\Pi_n)_{Inner\,Cylinder}\sin\theta\ \Big]\ (z - L_c) R_{c1}\, d\theta\, dz$$

$$+\ \Big[\iint\ (\Pi_t)^{r-\theta}_{Outer\,Cylinder}\cos\theta\ +\ \iint\ (\Pi_n)_{Outer\,Cylinder}\sin\theta\Big]\ \ (z - L_c)\, R_{c2}\, d\theta\, dz\}$$

$$+\sum_i \left\{\Big[-\iint (\Pi_t)^{r-z}_{Baffle}\sin\theta\, r\, dr\, d\theta + \iint (\Pi_t)^{r-\theta}_{Baffle}\cos\theta\, r\, dr\, d\theta\Big]_{z=L_i-\frac{d}{2}} \left(-L_c + L_i - \frac{d}{2}\right)\right\}$$

$$+\sum_i\ \left\{\ \Big[-\iint (\Pi_t)^{r-z}_{Baffle}\sin\theta\, r\, dr\, d\theta\ +\ \iint (\Pi_t)^{r-\theta}_{Baffle}\cos\theta\, r\, dr\, d\theta\Big]_{z=L_i+\frac{d}{2}} \left(-L_c + L_i + \frac{d}{2}\right)\right\} \quad (7\text{-}22)$$

$$M_y = \Big[\iint (\Pi_t)^{r-z}_{Top\ Wall} + \iint (\Pi_t)^{r-z}_{Bottom\ Wall}\Big](L_c - L_d + R_d\sin\phi) R_d^2\cos\phi\cdot\sin\phi\cdot\cos\theta\, d\phi\, d\theta$$

$$+\Big[\iint -(\Pi_t)^{r-\theta}_{Top\ Wall} - \iint (\Pi_t)^{r-\theta}_{Bottom\ Wall}\Big]\ (L_c - L_d + R_d\sin\phi)\ \cdot\ R_d^2\cos\phi\cdot\sin\theta\, d\phi\, d\theta$$

$$+\Bigg[\iint(\Pi_n)_{Top\ Wall}+\iint(\Pi_n)_{Bottom\ Wall}\Bigg]\ (L_c-L_d+R_d\sin\phi)\ R_d^2\cdot\cos^2\phi\cdot\cos\theta d\phi d\theta$$

$$+\ \{\ \Bigg[\iint-(\Pi_t)^{r-\theta}_{Inner\,Cylinder}\sin\theta+\iint(\Pi_n)_{Inner\,Cylinder}\cdot\cos\theta\Bigg]\cdot(z-L_c)R_{c1}d\theta dz$$

$$+\ \Bigg[\ \iint\ -(\Pi_t)^{r-\theta}_{Outer\,Cylinder}\sin\theta\ +\ \iint(\Pi_n)_{Outer\,Cylinder}\cos\theta\Bigg]\ (z-L_c)\ \ R_{c2}d\theta dz\}$$

$$-\{[\iint(\Pi_t)^{r-z}_{Top\ Wall}+\iint(\Pi_t)^{r-z}_{Bottom\ Wall}]\cdot R_d^3\cos^2\phi\cdot\cos\theta d\phi d\theta+[\iint(\Pi_n)_{Top\ Wall}$$

$$+\iint(\Pi_n)_{Bottom\,Wall}]\cdot R_d^3\cdot\cos^2\phi\cdot\sin\phi\cdot\cos\theta d\phi d\theta$$

$$+\iint(\Pi_t)^{r-z}_{Inner\,Cylinder}R_{c1}^2\cos\phi d\phi d\theta\ +\ \iint(\Pi_t)^{r-z}_{Outer\,Cylinder}R_{c2}^2\cos\phi d\phi d\theta\}$$

$$+\sum_i\Bigg\{\ \Bigg[\iint(\Pi_t)^{r-z}_{Baffle}\cos\theta rdrd\theta\ +\ \iint(\Pi_t)^{r-\theta}_{Baffle}\sin\theta rdrd\theta\Bigg]_{z=L_i-\frac{d}{2}}(-L_c+L_i-\frac{d}{2})\Bigg\}$$

$$+\sum_i\Bigg\{\ \Bigg[-\iint(\Pi_t)^{r-z}_{Baffle}\cos\theta rdrd\theta\ +\ \iint(\Pi_t)^{r-\theta}_{Baffle}\sin\theta rdrd\theta\Bigg]_{z=L_i+\frac{d}{2}}(-L_c+L_i+\frac{d}{2})\Bigg\}\tag{7-23}$$

$$M_z=\Bigg[\iint-(\Pi_t)^{r-z}_{Top\ Wall}+\iint(\Pi_t)^{r-z}_{Bottom\ Wall}\Bigg]R_d^3\cos^2\phi\cdot\sin\phi\cdot\sin\theta\cdot\cos\theta d\phi d\theta$$

$$+\Bigg[\iint(\Pi_t)^{r-\theta}_{Top\ Wall}+\iint(\Pi_t)^{r-\theta}_{Bottom\ Wall}\Bigg]R_d^3\cos^2\phi\cdot\cos^2\theta d\phi d\theta$$

$$+\Bigg[\iint(\Pi_n)_{Top\ Wall}+\iint(\Pi_n)_{Bottom\ Wall}\Bigg]R_d^3\cos^3\phi\cdot\sin\theta\cdot\cos\theta d\phi d\theta$$

$$+\Bigg[\iint(\Pi_t)^{r-\theta}_{Inner\,Cylinder}\cos\theta+\iint(\Pi_n)_{Inner\,Cylinder}\cdot\sin\theta\Bigg]R_{c1}^2\cos\theta d\theta dz$$

$$\{\ +\ \Bigg[\ \iint(\Pi_t)^{r-\theta}_{Outer\,Cylinder}\cos\theta\ +\ \iint(\Pi_n)_{Outer\,Cylinder}\sin\theta\Bigg]R_{c2}^2\cos\theta d\theta dz$$

$$-\{[\iint-(\Pi_t)^{r-z}_{Top\ Wall}+\iint(\Pi_t)^{r-z}_{Bottom\ Wall}]\cdot R_d^3\cos^2\phi\cdot\sin\phi\cdot\cos\theta\cdot\sin\theta d\phi d\theta$$

$$+\Bigg[\iint-(\Pi_t)^{r-\theta}_{Top\ Wall}-\iint(\Pi_t)^{r-\theta}_{Bottom\ Wall}\Bigg]R_d^3\cos^2\phi\cdot\sin^2\theta d\phi d\theta$$

$$+\left[\iint (\Pi_n)_{Top\ Wall} + (\Pi_n)_{Bottom\ Wall}\right] R_d^3 \cos^3\phi \cdot \cos\theta \cdot \sin\theta \, d\phi \, d\theta$$

$$+\left[\iint - (\Pi_t)^{r-\theta}_{Inner\ Cylinder} \sin\theta + \iint (\Pi_n)_{Inner\ Cylinder} \cos\theta\right] R_{c1}^2 \sin\theta \, d\theta \, dz$$

$$+\left[\iint - (\Pi_t)^{r-\theta}_{Outer\ Cylinder} \sin\theta + \iint (\Pi_n)_{Outer\ Cylinder} \cos\theta\right] R_{c2} \sin\theta \, d\theta \, dz \} \quad (7\text{-}24)$$

where L_d denotes the height of the dome (see Fig. 2).

After the integration of Eqs. (7-19) thru (7-24), components of the moment can be rewritten as the following expression:

$$\begin{bmatrix} M_x \\ M_y \\ M_z \end{bmatrix} = \begin{bmatrix} L_y F_z - (L_z - L_c) F_y \\ (L_z - L_c) F_x - L_x F_z \\ L_x F_y - L_y F_x \end{bmatrix} \qquad (7\text{-}25)$$

where L_x, L_y, and L_z denote the components of the moment arm along x, y, and z axes, respectively.

By using the relation of $F_\alpha \, L_\alpha = 0$, or $F_x \, L_x + F_y \, L_y + F_z \, (L_z - L_c) = 0$, moment arms of the moment of fluid stress moment induced by the slosh wave excitation can be computed from the following relations:

$$\begin{bmatrix} L_x \\ L_y \\ L_z - L_c \end{bmatrix} = \frac{1}{F_x^2 + F_y^2 + F_z^2} \begin{bmatrix} F_y M_z - F_z M_y \\ F_z M_x - F_x M_z \\ F_x M_y - F_y M_x \end{bmatrix} \qquad (7\text{-}26)$$

VIII. Methods of Numerical Simulation

Detailed descriptions of the computational algorithm applicable to cryogenic fluid management under microgravity are also given in our earlier studies (Hung et al., 1990 a,b,c). In this report, a full-scale AXAF-S spacecraft propellant dewar tanks with a radius of 68 cm and a height of 145 cm will be used in the numerical simulation. The propellant tank is 70% filled with cryogenic liquid helium and the rest of the ullage is filled with helium vapor. The temperature of cryogenic helium is 1.3 K. In this study the following data were used: liquid helium density = 0.145 g/cm^3, helium vapor density = 0.00147 g/cm^3, fluid pressure = 1.66 x 10^3 dyne/cm^2, surface tension coefficient at the interface between liquid helium and helium vapor = 0.346 dyne/cm, liquid helium viscosity coefficient = 1.12 x 10^{-4} cm^2/s; and contact angle = 5°. The initial profiles of the liquid-vapor interface for the rotating dewar are determined from computations based on algorithms developed for the steady state formulation of microgravity fluid management (Hung et al., 1990 a,b,c).

A staggered grid for the velocity components is used in this computer program. The method was developed by Harlow and Welch (1965) for their MAC (marker-and-cell) method of studying fluid flows along a free surface. The finite difference method employed in this numerical study was the "Hybrid Scheme" developed by Spalding (1972). The formulation for this method is valid for any arbitrary interface location between the grid points and is not limited to middle point interfaces (Patankar and Spalding, 1972). An algorithm for a semi-implicit method (Patankar, 1980) was used as the procedure for modeling the flow field. The time step is determined automatically based on the size of the grid points and the velocity of flow fields. A detailed description of the computational algorithm applicable to microgravity fluid management is illustrated in our earlier studies (Hung et al., 1990 a,b,c). Figures 8(A) and 8(B) show the similar distribution of grid points for the dewar tank for the AXAF-S spacecraft in the radial-axial plane and radial-circumferential plane, respectively, in cylindrical coordinates.

IX. Spacecraft Sloshing Dynamics Associated With Spinning and/or Slew Motions

By using the mathematical formulations illustrated in Sections III and IV, subject to the initial and boundary conditions in Section V, spacecraft sloshing dynamics associated with slew motions depending upon the specific scientific missions assigned to the spacecraft are investigated. Two examples are given to illustrate sloshing dynamics driven by each of the gravity gradient and jitter accelerations associated with slew motion for the AXAF-S spacecraft.

(IX-A) Spacecraft Sloshing Dynamics Driven by Gravity Gradient Acceleration Associated With Slew Motion

As we indicated earlier, AXAF-S spacecraft is capable to observe point and extended sources of active galactic nuclei, clusters of galaxies, supernova remnants, x-ray binaries, etc., through spacecraft slew motion of pointing control. Assume that slew motion is along the y"-axis (see Figure 1), gravity gradient acceleration associated with slew motion can be computed from the non-inertia frame expressions of Equations (3-1) and (3-26). It is assumed that the slew motion operates in 90° in 10 minutes. Non-inertia frame fundamental equations, shown in Equations (4-1) to (4-5) shall be adopted with making ω_z and $\dot{\omega}_z$ equal to zero because there is no spinning motion in the z-axis. Initial and boundary conditions, shown in Equations (5-1) to (5-19), shall also be considered in our computation.

In this example, spacecraft sloshing dynamics driven by gravity gradient acceleration associated with slew motion in the y"-axis, shown in Figure 1, have been investigated. As the orbital period of AXAF-S spacecraft is 97.6 min and period of slew motion in the y"-axis is 600 s, the component of gravity gradient acceleration along the (x, y, z) directions acted on the fluid mass located at $(r, \theta, z) = (12\text{ cm}, \pi/2, 3\text{ cm})$ is shown in Figure 9. This figure shows that the magnitude of gravity gradient acceleration is on the order of 10^{-7} g_o for AXAF-S dewar on its operation orbit. The distance from the spacecraft mass center to the bottom of the dewar, L_c, shown in Figure 1, is 257.8 cm. The grid point generation of the dewar tank, shown in Figure 8, is adopted in this example of the AXAF-S dewar.

Gravity gradient acceleration indicates that acceleration acted on any fluid mass inside the container increases two units of acceleration per unit of distance measured from the spacecraft mass center to the location of the fluid mass parallel along the radial axis from the spacecraft mass center to the center of the Earth (parallel to unit vector $\hat{r}_c$ shown in Figure 1) while the acceleration acted on the fluid mass decreases one unit of acceleration per unit of the shortest distance measured from the location of the fluid mass to the radial axis along the vector from the mass center of the spacecraft to the center of the Earth (Forward, 1982). As the magnitude and the direction of gravity gradient acceleration acted on each fluid mass is strongly dependent upon how far the location of the fluid mass deviates from the spacecraft mass center measured along the axis parallel to the vector $\hat{r}_c$ which varies with respect to time, it can be anticipated that gravity gradient acceleration acted on the fluid mass is different for fluid mass at different locations in the container.

The equilibrium shape of the liquid-vapor interface for a dewar with 70% liquid-filled level under a residual gravity environment below 10^{-7} g_o, as that shown in Figure 9, is a sphere. Figure 10(A) shows the initial shape of the interface in the r-z plane at $\theta = 0°$ and 180°; Figure 10(B) shows the initial profile of the liquid-vapor interface in the r-z plane at $\theta = 90°$ and 270°; Figure 10(C) shows the initial profile of the liquid-vapor interface in the r-θ plane at height $z = 95.9$ cm; and Figure 10(D) shows the initial profile of three-dimensional liquid-vapor interface.

Figure 11 shows the time sequence evolution of the three-dimensional dynamical behavior of the interface oscillations driven by gravity gradient acceleration associated with slew motion. For the convenience of comparison, figures of liquid-vapor interface profiles with the same values of the time sequences chosen throughout this paper are at time $t = 334$, 392, 431, 456, 487, 524, 554, 588, 600, 695, 784 and 800 seconds. It clearly shows that there are a series of asymmetric oscillations excited along the surface of sloshing dynamics governed liquid-vapor interface driven by asymmetric gravity gradient acceleration associated with slew motion.

The evolution of the sloshing dynamics governed interface oscillations at various cross-sections driven by gravity gradient acceleration associated with slew motion are also examined. Figures 12 and 13 show the time sequence of the sloshing dynamics governed liquid-vapor interface profiles, driven by the same gravity gradient acceleration associated with slew motion as that shown in Figure 11, in the vertical r-z plane at $\theta = 0^\circ$ and 180°, and at $\theta = 90^\circ$ and 270°, respectively. It indicates that the spherical shape bubble (helium vapor) configurations change from axial symmetric to asymmetric profiles in both planes during the course of slew motion.

Figure 9 shows that gravity gradient acceleration associated with slew motion is pointing toward the southwestern direction in the x-z plane (or r-z plane at $\theta = 0^\circ$ and 180°), and also is pointing toward the southern direction in the y-z plane (or r-z plane at $\theta = 90^\circ$ and 270°). These indicate that liquid is pushed toward the southwestern direction (the bubble is pushed toward the northeastern direction) in r-z plane at $\theta = 0^\circ$ and 180° while the liquid is pushed toward the southern direction (the bubble is pushed in the northern direction) in r-z plane at $\theta = 90^\circ$ and 270°. Figures 12 and 13 exactly demonstrate these results.

Figure 14 shows the time evolution of the sloshing dynamics governed liquid-vapor interface oscillations driven by the same gravity gradient acceleration associated with slew motion, as that shown in Figure 11, in the horizontal (r-θ) plane for height at $z = 95.9$ cm. It shows that a circular-shaped bubble configuration of the liquid-vapor interface changes from axial symmetry [see Figure 10(C)] to asymmetry (see Figure 14) profiles. Based on Figure 9, it shows that gravity gradient acceleration associated with slew motion is pointing toward the western direction in the x-y plane (or r-θ plane). This implies that the liquid is pushed toward the western direction while bubble is pushed toward the eastern direction in the r-θ plane. In the meanwhile, the bubble is also pushed in a upward direction along the spinning axis of the dewar as that shown in Figures 12 and 13. This scenario exactly reflects the evolution of the bubble shown in Figure 14 that the bubble is pushed toward the eastern direction and also gradually becomes smaller due to the upward movement of the bubble.

Comparison of Figures 9,11,12,13 and 14 illustrate some peculiar behavior of cryogenic helium II fluids with temperature below the λ-point (2.17 K) in which liquid helium demonstrates a number of remarkable properties of superfluidity such as extremely low viscous and surface tension coefficients reacted to the disturbances driven by gravity gradient acceleration associated with slew motion. These results can be concluded as follows: (a) Both negative direction of gravity gradient acceleration in x and z components imply that the liquid is pushed toward negative x and z directions while bubble is pushed toward positive x and z directions. (b) Comparison of the magnitudes of gravity gradient acceleration in the x, y and z components, shown in Figure 9, indicated that $g_z > g_x > g_y$. This magnitude of driving force reflects the results of the bubble mass center fluctuations, shown in Figures 11, 12 and 13. (c) Configuration of bubble fluctuations at time $t = 334$ s, shown in Figures 11 and

12, indicate a near perfect shape of a sphere, as that shown in Figure 10, even though an extensive gravity gradient acceleration has continuously applied to the fluid system starting at $t = 0$, shown in Figure 9. (d) Uneven and imbalanced flow velocities toward the southwestern direction create similar uneven and imbalanced pressure distribution reacted to the bubble toward the northeastern direction. Because of extremely low surface tension coefficients of helium II between the liquid-vapor interface, a deformed irregular concave and convex-shaped oscillating bubble is created.

Figure 15 shows time fluctuations of the locations of bubble mass centers of the fluids inside the dewar container due to sloshing dynamics driven by gravity gradient acceleration associated with slew motion. The values of bubble mass center fluctuations are $(\Delta x_c, \Delta y_c, \Delta z_c) = (11.8, 1.25, 18.4)$ cm. It shows $\Delta z_c > \Delta x_c > \Delta y_c$ for bubble mass center fluctuations driven by gravity gradient acceleration associated with slew motion.

The trend of the bubble center fluctuations, $\Delta z_c > \Delta x_c > \Delta y_c$, exactly reflect the values of major driving forces of gravity gradient acceleration associated with slew motion in which it shows $g_z > g_x > g_y$ as that shown in Figure 9.

(IX-B) Spacecraft Sloshing Dynamics Driven by Jitter Acceleration Associated With Slew Motion

By using the mathematical formulations illustrated in Sections III to IV, one can numerically simulate spacecraft sloshing dynamics associated with spinning and/or slew motions depending upon the specific scientific missions assigned to the spacecraft. As we indicated earlier, AXAF-S spacecraft is capable to observe point and extended source of active galactic nuclei, clusters of galaxies, supernova remnants, x-ray binaries, etc., through spacecraft slew motion of pointing control.

If slew motion operates with a range of 90° in 10 minutes (= 600 s), the component of jitter acceleration, based on Equations (3-1) to (3-34), along the (x, y, z) directions acted on the fluid mass located at $(r, \theta, z) = (12 \text{ cm}, \pi/2, 3 \text{ cm})$ is shown in Figure 16. This figure shows that the magnitude of gravity gradient acceleration is on the order of 10^{-5} g_o.

The equilibrium shape of the liquid-vapor interface for a dewar with 70% liquid-filled level under a residual gravity environment below 10^{-6} g_o is a sphere. Figure 10(A) shows the initial shape of the interface in the r-z plane at $\theta = 0°$ and 180°; Figure 10(B) shows the initial profile of the liquid-vapor interface in the r-z plane at $\theta = 90°$ and 270°; Figure 10(C) shows the initial profile of the liquid-vapor interface in the r-θ plane at height $z = 95.9$ cm; and Figure 10(D) shows the initial profile of three-dimensional liquid-vapor interface.

Figure 17 shows the time sequence evolution of the three-dimensional behavior of the interface oscillations driven by jitter acceleration associated with slew motion. It is shown in this figure that a time sequence evolution of liquid-vapor interface profiles at time t = 60.4, 258, 323, 354, 379, 403, 430, 528, 572, 628, 663, and 800 seconds are illustrated. It clearly shows that there are a series of asymmetric oscillations excited along the surface of sloshing dynamics governed liquid-vapor interface driven by asymmetric jitter acceleration associated with slew motion.

Figure 18 shows the time sequence of the sloshing dynamics governed liquid-vapor interface profiles, driven by the same jitter acceleration associated with slew motion as that shown in Figure 17, in the vertical r-z plane at $\theta = 0°$ and 180°. It clearly indicates that the spherical shape bubble (helium vapor) configurations change from axial symmetric to asymmetric profiles during the course of slew motion.

The evolution of the sloshing dynamics governed interface oscillations at various cross-sections driven by gravity jitter acceleration associated with slew motion are also examined. Figures 18 and 19 show the time sequence of the sloshing dynamics governed liquid-vapor interface profiles, driven by the same gravity jitter acceleration associated with slew motion as that shown in Figure 17, in the vertical r-z plane at $\theta = 0°$ and 180°, and at $\theta = 90°$ and 270°, respectively. It indicates that the spherical shape bubble (helium vapor) configurations change from axial symmetric to asymmetric profiles in both planes during the course of slew motion.

Figure 16 shows that gravity jitter acceleration associated with slew motion is pointing toward the southeastern direction at the very beginning and then is pointing toward the southwestern direction at the end in the x-z plane (or r-z plane at $\theta = 0°$ and 180°), and also is pointing toward the southern direction in the y-z plane (or r-z plane at $\theta = 90°$ and 270°). These indicate that liquid is pushed toward the southeastern and then toward the southwestern directions (the bubble is pushed toward the northwestern and then toward the northeastern directions) in r-z plane at $\theta = 0°$ and 180° while the liquid is pushed toward the southern direction (the bubble is pushed toward the northern direction) in r-z plane at $\theta = 90°$ and 270°. Figures 18 and 19 exactly demonstrate these results.

Figure 20 shows the time evolution of the sloshing dynamics governed liquid-vapor interface oscillations driven by the same gravity jitter acceleration associated with slew motion, as that shown in Figure 17, in the horizontal (r-θ) plane for height at z = 95.9 cm. It shows that a circular-shaped bubble configuration of the liquid-vapor interface changes from axial symmetry [see Figure 10(C)] to asymmetry (see Figure 20) profiles. Based on Figure 16, it shows that gravity jitter acceleration associated with slew motion is pointing toward the eastern direction at the beginning and then pointing toward the western direction at the end in the x-y plane (or r-θ plane). This implies that the liquid is pushed toward the eastern direction and then toward the western direction while bubble is pushed toward the western direction and then toward the eastern direction in the r-θ plane. In the meanwhile, the bubble is also pushed toward the upward direction along the spinning axis of the dewar as that shown in Figures 18 and 19. This scenario exactly reflects the evolution of the bubble shown in Figure 20.

Figure 21 shows time evolution of the locations of bubble mass centers of fluids inside the dewar container due to sloshing dynamics driven by jitter acceleration associated with slew motion. The values of bubble mass center fluctuations are $(\Delta x_c, \Delta y_c, \Delta z_c) = (28.9, 0.44, 30.2)$ cm. It shows $\Delta z_c > \Delta x_c > \Delta y_c$ for bubble mass center fluctuations driven by jitter acceleration associated with slew motion. Behavior of bubble mass center fluctuations, shown in Figure 21 are the exact reflection of the behavior of jitter accelerations, shown in Figure 16.

Comparison between Figures 16 to 21 illustrate some peculiar behavior of cryogenic helium fluids with temperature below λ-point (2.17 K) in which helium demonstrates a number of remarkable properties of superfluidity such as extremely low viscous and surface tension coefficients reacted to the disturbances driven by jitter acceleration associated with slew motion. It can be concluded as follows: (a) Jitter acceleration associated with slew motion started at time $t = 0$. However, bubble mass center fluctuations did not start to react to the driven force until t = 80 s for x_c and t = 160 s for z_c. In other words, bubble configuration was in perfect spherical-shaped at 80 s after jitter acceleration associated with slew motion was applied. (b) x-component jitter acceleration associated with slew motion was applied to the fluid element with positive value from t = 0 to 300 s; negative value from t = 300 to 600 s; and zero value after t = 600 s. However, westward movement of bubble continued from t = 80 to 450 s, and then switched to eastward movement to t = 800 s which was 200 s after acceleration vanished. Obviously, there is a phase-shift between action of force and reaction of motion. (c) The z-component jitter acceleration associated with slew motion was applied to the fluid element with negative value from t = 80 to 500 s and the zero value after t = 500 s. However, the northward movement of the bubble started at t = 160 s; bounced back from the wall at t = 530 s; and then the southward movement continued to t = 800 s which was 300 s after acceleration vanished. Obviously, the motion continued for a long period of time even after the applied force vanished due to extremely low viscosity of helium II fluids. (d) An intensive oscillation of bubble with a deformation of irregular concave and convex-shaped continued and sustained for several hundred seconds after the applied force vanished due to extremely low surface tension coefficient for helium II fluids.

X. Sloshing Dynamics Induced Angular Momentum and Moment Fluctuations Driven by Gravity Gradient and Jitter Accelerations Associated With Slew Motion

(X-A) Angular Momentum and Moment Fluctuations Driven by Gravity Gradient Acceleration Associated With Slew Motion

Figure 22 shows the computed time variation of the fluctuations of angular momentum driven by gravity gradient acceleration associated with slew motion.

This figure shows the following results: (a) The values of angular momentum fluctuations are $(\Delta H_x, \Delta H_y, \Delta H_z) = (0.032, 2.602, 0.015)\ 10^6$ g·cm²/s, it clearly indicates $\Delta H_y > \Delta H_x > \Delta H_z$. The maximum absolute values of angular moment are Max $(|H_x|, |H_y|, |H_z|) = (0.032, 2.602, 0.015)\ 10^6$ g·cm²/s. It also indicates $|H_y| > |H_x| > |H_z|$. (b) The initial values of H_x, H_y and H_z start from zero value in non-inertia frame. (c) Variations of H_y is very much following the trend of angular displacement in the y-axis due to the slew motion, shown in Figure 9, while the variations of H_x and H_z are much smaller than H_y because there is no slew motion applied on the x- and z-axes.

Figures 23(A), 23(B) and 23(C) show variations of fluid moments due to sloshing dynamics driven by gravity gradient acceleration associated with slew motion along the x, y and z axes, respectively. The values of fluid moment fluctuations are $(\Delta M_x, \Delta M_y, \Delta M_z) = (613.1, 8235.4, 129.0)$ dyne·cm. The maximum absolute values of fluid moment are Max $(|M_x|, |M_y|, |M_z|) = (412.4, 6101.1, 69.2)$ dyne·cm. It shows $\Delta M_y > \Delta M_x > \Delta M_z$ and $|M_y| > |M_x| > |M_z|$. Characteristics of the fluctuations of fluid moments due to sloshing dynamics driven by gravity gradient acceleration associated with slew motion in the y-axis draw three point conclusions similar to that drawn for the fluctuations of angular momentum of fluid system except that the trend of fluid moment fluctuations follow that of angular velocity of the spacecraft slew motion in the y-axis, shown in Figure 4, rather than that of angular displacement for angular momentum because fluid moment is time derivative of angular momentum while the angular velocity is the time derivative of angular displacement.

(X-B) Angular Momentum and Moment Fluctuations Driven by Gravity Jitter Acceleration Associated With Slew Motion

Figures 24(A, 24(B) and 24(C) show the computed time variation of the fluctuations of angular momentum driven by gravity jitter acceleration associated with slew motion along the x, y and z axes, respectively. This figure shows the following results: (a) The values of angular momentum fluctuations are (ΔH_x, ΔH_y, ΔH_z) = (0.4, 17.55, 0.161) 10^6 g·cm^2/s, it clearly indicates $\Delta H_y > \Delta H_x > \Delta H_z$. The maximum absolute values of angular moment are Max ($|H_x|$, $|H_y|$, $|H_z|$) = (0.275, 8.92, 0.091) 10^6 g·cm^2/s. It also indicates $|H_y| > |H_x| > |H_z|$. (b) The initial values of H_x, H_y and H_z start from zero value in non-inertia frame. (c) Variations of H_y dominates the whole spectrum of angular momentum fluctuations because angular displacement in the y-axis is the only slew motion in the entire process, while the variations of H_x and H_z are much smaller than H_y because there is no slew motion applied on the x- and z-axes.

Figures 25(A), 25(B) and 25(C) show variations of fluid moments due to sloshing dynamics driven by gravity jitter acceleration associated with slew motion along the x, y and z axes, respectively. The values of fluid moment fluctuations are (ΔM_x, ΔM_y, ΔM_z) = (13.38, 200.79, 4.32) 10^3 dyne·cm. The maximum absolute values of fluid moment are Max ($|M_x|$, $|M_y|$, $|M_z|$) = (6.77, 100.75, 2.33) 10^3 dyne·cm. It shows $\Delta M_y > \Delta M_x > \Delta M_z$ and $|M_y| > |M_x| > |M_z|$. Characteristics of the fluctuations of fluid moments due to sloshing dynamics driven by gravity jitter acceleration associated with slew motion in the y-axis draw three point conclusions similar to that drawn for the fluctuations of angular momentum of fluid system.

XI. Characteristics of Sloshing Dynamics Induced Fluid Stresses and Moment Fluctuations Exerted on the Dewar Container

In this study, characteristics of the asymmetric fluctuations of liquid-vapor interface due to sloshing dynamics driven by each of the gravity gradient and jitter accelerations associated with slew motion were discussed in Section

IX. In Section VIII, the mathematical formulation of the fluctuations of fluid stresses and the moment of fluid stresses exerted on the dewar container have been illustrated. With references to Sections VIII and IX, one can calculate the fluid stresses and the associated moments exerted on the dewar container of spacecraft dewar tank.

(XI-A) Fluid Stress Forces and Moment Fluctuations Exerted on Dewar Container Driven by Gravity Gradient Acceleration Associated With Slew Motion

Figure 26(A), 26(B) and 26(C) show the computed time variation of the fluctuations of fluid stress forces exerted on the dewar container driven by gravity gradient acceleration associated with slew motion in the y-axis with components along the x-, y-, and z-axes, respectively. These figures show the following results: (a) The values of fluid stress force fluctuations are $(\Delta F_x, \Delta F_y, \Delta F_z) = (59.2, 4.11, 61.02)$ dynes, it clearly indicates $\Delta F_z > \Delta F_x > \Delta F_y$. The maximum absolute values of fluid stress force are Max $(|F_x|, |F_y|, |F_z|) = (47.42, 4.11, 78.68)$ dynes. It also indicates $|F_z| > |F_x| > |F_y|$. (b) The initial values of F_x and F_y start from zero value while that of the F_z starts from non-zero value. This is due to the fact that the major driving force of gravity gradient acceleration associated with slew motion at the beginning of slew motion is equal to zero along the x- and y-axes, and is non-zero along the z-axis. (c) The characteristics of fluid stress forces and their fluctuations are more likely following the trend of the major driving force of gravity gradient acceleration associated with slew motion in the y-axis as that shown in Figure 9. Comparison between Figures 26 and 9 reflect that the fluid system serves as a damping modulator for the forces acting on the fluid flows and then responds back to the spacecraft.

Figures 27(A), 27(B) and 27(C) show the variations of fluid stress moments exerted on the dewar container due to sloshing dynamics driven by gravity gradient acceleration associated with slew motion with components along the x, y and z axes, respectively. These figures show the following results: (a) The values of fluid stress moment fluctuations are (ΔM_x, ΔM_y, ΔM_z) = (770.6, 10784.5, 0.0004) dyne·cm. The maximum absolute values of fluid stress moment are Max ($|M_x|$, $|M_y|$, $|M_z|$) = (770.6, 8595.9, 0.0004) dyne·cm. (b) As slew motion is in the y-axis, this makes the magnitudes of both ΔM_y and $|M_y|$ to be the maximum. (c) As slew motion is in the y-axis, this makes the value of moment arm along the y-axis to be zero; and also as the y-component of the major driving force of gravity gradient acceleration associated with slew motion in the y-axis is equal to zero, this makes the magnitude of $|F_y|$ to be near zero. Since both $|F_y| \sim L_y \sim 0$, it leads $M_z = L_xF_y - L_yF_x \sim 0$.

Figure 28(A), 28(B) and 28(C) show time fluctuations of moment arms of fluid stress moments exerted on the dewar container due to sloshing dynamics driven by gravity gradient acceleration associated with slew motion in the y-axis for components along the x-, y-, and z-axes, respectively. These figures show the following results: (a) The values of moment arm fluctuations are (ΔL_x, ΔL_y, ΔL_z) = (119.2, 11.7, 156.1) cm. The maximum absolute values of moment arm are Max ($|L_x|$, $|L_y|$, $|L_z|$) = (91.3, 11.7, 257.8) cm. It shows $\Delta L_z > \Delta L_x > \Delta L_y$ and $|L_z| > |L_x| > |L_y|$. (b) As spacecraft slew motion is along the y-axis, this makes the values of L_y to be the minimum, and M_y to be the maximum. (c) As L_z is the function of F_xM_y, the values of M_y is the maximum and F_x is near to the maximum. This makes the values of L_z to be the maximum. (d) The trend of the fluctuations of momentum arm is very much like that of the fluid stress forces acting on the dewar container of the spacecraft. Again, the trend of the fluctuations of moment arm is very much like that of the major driving forces of gravity gradient acceleration associated with slew motion in the y-axis (see Figures 28 and 9).

(XI-B) Fluid Stress Forces and Moment Fluctuations Exerted on Dewar Container Driven by Gravity Jitter Acceleration Associated With Slew Motion

Figure 29(A), 29(B) and 29(C) show the computed time variation of the fluctuations of fluid stress forces exerted on the dewar container driven by gravity jitter acceleration associated with slew motion in the y-axis with components along the x-, y-, and z-axes, respectively. These figures show the following results: (a) The values of fluid stress force fluctuations are (ΔF_x, ΔF_y, ΔF_z) = (2.27, 0.04, 1.37) 10^3 dynes, it clearly indicates $\Delta F_x > \Delta F_z > \Delta F_y$. The maximum absolute values of fluid stress force are Max ($|F_x|$, $|F_y|$, $|F_z|$) = (1.15, 0.02, 1.20) 10^3 dynes. It also indicates $|F_z| > |F_x| > |F_y|$. (b) The initial values of F_x, F_y and F_z all start from zero value because there was no slew motion applying to the system at time $t = 0$. (c) Magnitudes and fluctuations of F_y is much smaller than F_x and F_z because the major driving moment of slew motion is along the y-axis. (d) The characteristics of fluid stress forces and their fluctuations are more likely following the trend of the major driving force of gravity jitter acceleration associated with slew motion in the y-axis as that shown in Figure 16. Comparison between Figures 29 and 16 reflect that the fluid system serves as a damping modulator for the forces acting on the fluid flows and then responds back to the spacecraft. The small fluctuations shown in the forces response back to the dewar container are due to the disturbances caused by the sloshing dynamics of the fluid system.

Figures 30(A), 30(B) and 30(C) show the variations of fluid stress moments exerted on the dewar container due to sloshing dynamics driven by gravity jitter acceleration associated with slew motion with components along the x, y and z axes, respectively. These figures show the following results: (a) The values of fluid stress moment fluctuations are $(\Delta M_x, \Delta M_y, \Delta M_z) = (7.53, 422.79, 0.0001)$ 10^3 dyne·cm. The maximum absolute values of fluid stress moment are Max $(|M_x|, |M_y|, |M_z|) = (4.31, 214.53, 0.0006)$ 10^3 dyne·cm. (b) As slew motion is in the y-axis, this makes the magnitudes of both ΔM_y and $|M_y|$ to be the maximum. (c) As slew motion is in the y-axis, this makes the value of moment arm along the y-axis to be zero; and also as the y-component of the major driving force of gravity jitter acceleration associated with slew motion in the y-axis is equal to zero, this makes the magnitude of $|F_y|$ to be near zero. Since both $|F_y| \sim L_y \sim 0$, it leads $M_x = L_yF_z - L_zF_y \sim 0$ and $M_z = L_xF_y - L_yF_x \sim 0$.

Figure 31(A), 31(B) and 31(C) show time fluctuations of moment arms of fluid stress moments exerted on the dewar container due to sloshing dynamics driven by gravity jitter acceleration associated with slew motion in the y-axis for components along the x-, y-, and z-axes, respectively. These figures show the following results: (a) The values of moment arm fluctuations are $(\Delta L_x, \Delta L_y, \Delta L_z) = (190.4, 56.1, 186.6)$ cm. The maximum absolute values of moment arm are Max $(|L_x|, |L_y|, |L_z|) = (95.4, 49.8, 186.6)$ cm. It shows $\Delta L_z > \Delta L_x > \Delta L_y$ and $|L_z| > |L_x| > |L_y|$. (b) As spacecraft slew motion is along the y-axis, this makes the values of L_y to be the minimum, and M_y to be the maximum. (c) As L_z is the function of F_xM_y ($F_yM_x \sim 0$ because $F_y = 0$), the values of M_y is the maximum and F_x is near to the maximum. This makes the values of L_z to be the maximum. (d) The trend of the fluctuations of momentum arm is very much like that of the fluid stress forces acting on the dewar container of the spacecraft. Again, the trend of the fluctuations of moment arm is very much like that of the major driving forces of gravity jitter acceleration associated with slew motion in the y-axis (see Figures 31 and 16).

XII. Discussion and Conclusion

With different scientific missions, some experimental spacecrafts have to operate with various kinds of slew motion for the purpose to perform its scientific experiments. In this study, the AXAF-S spacecraft has been given as an example to show a spacecraft operated with slew motion. The instability of the liquid-vapor interface surface of the fluid systems can be induced by the presence of gravity gradient and jitter accelerations associated with slew motion of the spacecraft. These instabilities originated from sloshing dynamics can cause various problems of spacecraft control systems. Sometimes, these sloshing dynamics problems can even deteriorate the quality of the normal operation of the spacecraft. It is vitally important to understand fully the characteristics of the spacecraft sloshing dynamics before one can assure the high quality operation of scientific spacecraft.

In this report, the generalized mathematical formulation of sloshing dynamics for partially filled liquid in the dewar container driven by the both the gravity gradient and jitter accelerations associated with spinning and/or slew motions are investigated. Explicit mathematical expressions of both the gravity gradient and jitter acceleration associated with various types of spinning and/or slew motions are derived. The formulations of fluid moment and angular moment fluctuations in fluid profiles induced by sloshing dynamics, together with fluid stress and moment fluctuations exerted on the spacecraft dewar container have also been derived.

Two examples of the numerical simulation of sloshing dynamics driven by orbital accelerations, applicable to the AXAF-S spacecraft associated with slew motion, have been carried out. These examples demonstrate (1) how great the degrees of sloshing dynamics for imbalance profiles have been developed; (2) how great the amplitudes and fluctuations of angular momentum and moment have been induced; and (3) how great the forces and moment fluctuations exerted on the dewar wall of the container have been excited by the effects of gravity gradient and jitter accelerations associated with spinning and/or slew motions. The generalized mathematical formulations shown in this study can provide a useful tool for the development of effective control techniques to assure the high quality operation of the spacecraft to achieve the final goal of scientific missions.

References

Avduyevsky V. S. (editor), Scientific Foundations of Space Manufacturing, MIR, Moscow, USSR 1984.

Everitt, F. Ed., Testing Einstein With Orbiting Gyroscopes - Gravity Probe-B, pp. 28, Stanford University, Palo Alto, CA, 1990.

Forward, R. L., Flattening Space-Time Near the Earth, Physical Review, Series D, Vol. 26, pp. 735-744, 1982.

Hoare, F. E., Jackson, L. C., and Kurti, N., Experimental Cryogenics: Liquid Helium II, Butterworths, London, U.K. (1961).

Hung, R. J., Superfluid and Normal Fluid Helium II in a Rotating Tank Under Low and Microgravity Environments, Proceedings of National Science Council, Series (A), Vol. 14, pp. 289-29, 1990.

Hung, R. J., and Lee, C. C., Characteristics and Behaviors of Gravity Probe-B Spacecraft Propulsion System, Proceed. National Science Council (A), 16, pp. 339-352, 1992.

Hung, R. J., Lee, C. C., and Leslie, F. W., Dynamics of Gravity Probe-B Spacecraft Due to Gravity Jitter Induced Cryogenic Helium Disturbances in Rotating Dewar, Advances in Space Research, Vol. 13, in press, 1993c.

Hung, R. J., Lee, C. C., and Leslie, F. W., Effect of G-Jitters on the Stability of Rotating Bubble Under Microgravity Environment, Acta Astronautica, Vol. 21, pp. 309-321, 1990a.

Hung, R. J., Lee, C. C., and Leslie, F. W., Gravity-Jitter Response Slosh Waves Excitation on the Fluid Rotating Dewar, Advances in Space Research, Vol. 11(7), pp. 201-208, 1991d.

Hung, R. J., Lee, C. C., and Leslie, F. W., Gravity-Jitter Effected Slosh Waves on the Stability of Rotating Bubble Under Microgravity Environment, Advances in Space Research, Vol. 11(7), pp. 209-216, 1991e.

Hung, R. J., Lee, C. C., and Leslie, F. W., Slosh Wave Excitation in a Partially Filled Rotating Tank Due to Gravity Jitters in a Microgravity Environment, Acta Astronautica, Vol. 25, pp. 523-551, 1991f.

Hung, R. J., Lee, C. C., and Leslie, F. W., Response of Gravity Level Fluctuations on the Gravity Probe-B Spacecraft Propellant System, Journal of Propulsion and Power, Vol. 7, pp. 556-564, 1991g.

Hung, R. J., Lee, C. C., and Leslie, Slosh Wave Excitation of Cryogenic Liquid Helium in Gravity Probe-B Rotating Dewar, Advances in Cryogenic Engineering, 37, 1281-1290, 1991j.

Hung, R. J., Lee, C. C., and Leslie, F. W., Gravity Jitter Excited Cryogenic Liquid Slosh Waves in Microgravity Environment, Advances in Cryogenic Engineering, 37, 1291-1302, 1991c.

Hung, R. J., Lee, C. C., and Leslie, F. W., Spacecraft Dynamical Distribution of Fluid Stresses Activated by Gravity Jitter Induced Slosh Waves, Journal of Guidance, Control and Dynamics, Vol. 15, pp. 817-824, 1992c.

Hung, R. J., Lee, C. C., and Leslie, F. W., Similarity Rules in Gravity Jitter-Related Spacecraft Liquid Propellant Slosh Waves Excitation, Journal of Fluids and Structures, Vol. 6, pp. 493-522, 1992d.

Hung, R. J., Lee, C. C., and Leslie, F. W., Effect of the Baffle on the Spacecraft Fluid Propellant Viscous Stress and Moment Fluctuations, Transaction of the Japan Society for Aeronautical and Space Sciences, 35, 187-207, 1993a.

Hung, R. J., Lee, C.C., and Leslie, F. W., Effect of the Baffle on the Asymmetric Gravity-Jitter Excited Slosh Waves and Spacecraft Moment and Angular Momentum Fluctuations, Journal of Aerospace Engineering (United Kingdom), in press, 1993b.

Hung, R. J., and Lee, C. C., Effect of the Baffle on On-Orbit Spacecraft Fluid System Angular Momentum Fluctuations and Action of Viscous Stress Moment Exerted on the Container, Proceed. National Science Council, (A), 17, in press, 1993c.

Hung, R. J., Lee, C. C., and Shyu, K. L., Reorientation of Rotating Fluid in Microgravity Environment With and Without Gravity Jitters, Journal of Spacecraft and Rockets, Vol. 28, pp. 71-79, 1991h.

Hung, R. J., and Leslie, F. W., Bubble Shapes in a Liquid-Filled Rotating Container Under Low Gravity, Journal of Spacecraft and Rockets, Vol. 25, pp. 70-74, 1988.

Hung, R. J., Pan, H. L., and Leslie, F. W. Gravity Gradient or Gravity Jitter Induced Viscous Stress and Moment Fluctuations in Microgravity, Fluid Dynamics Research, in press 1993d.

Hung, R. J., and Pan, H. L., Asymmetric Slosh Wave Excitation in Liquid-Vapor Interface Under Microgravity, Acta Mechanica Sinica, in press, 1993.

Hung, R. J., and Shyu, K. L., Cryogenic Hydrogen Reorientation and Geyser Initiation at Various Liquid-Filled Levels in Microgravity, Advances in Space Research, Vol. 11(7), pp. 217-226, 1991a.

Hung, R. J., and Shyu, K. L., Cryogenic Liquid Hydrogen Reorientation Activated by High Frequency Impulsive Reverse Gravity Acceleration of Geyser Initiation, Microgravity Quarterly, Vol. 1(2), pp. 81-92, 1991b.

Hung, R. J., and Shyu, K. L., Space-Based Cryogenic Liquid Hydrogen Reorientation Activated by Low Frequency Impulsive Reverse Gravity Thruster of Geyser Initiation, Acta Astronautica, Vol. 25, pp. 709-719, 1991c.

Hung, R. J., and Shyu, K. L., Constant Reverse Thrust Activated Reorientation of Liquid Hydrogen with Geyser Initiation, Journal of Spacecraft and Rockets, Vol. 29, pp. 279-285, 1992a.

Hung, R. J., and Shyu, K. L., Excitation of Slosh Waves Associated with Low Frequency Impulsive Reverse Gravity Acceleration of Geyser Initiation, Acta Astronautica, Vol. 26, pp. 425-433, 1992b.

Hung, R. J., and Shyu, K. L., Medium Frequency Impulsive Thrust Activated Liquid Hydrogen Reorientation with Geyser, Journal of Propulsion and Power, Vol. 8, pp. 987-994, 1992c.

Hung, R. J., and Shyu, K. ., Suction Dip, Liquid Residual and slosh Wave Excitation during Liquid Draining in Microgravity, Advances in Space Research, 13(7), 147-154, 1993a.

Hung, R. J., and Shyu, K. L., Liquid Settlement, Resettlement, Slosh Wave Excitation and Geyser Motion During Reorientation in Microgravity, Advances in Space Research, 13(7), 155-163, 1993b.

Hung, R. J., and Shyu, K. L., Liquid Resettlement and Slosh Wave Excitation During Fluid Reorientation in Microgravity, Acta Astronautica, 27, in press, 1993c.

Hung, R. J., Shyu, K. L., and Lee, C. C., Slosh Wave Excitation Associated with High Frequency Impulsive Reverse Gravity Acceleration of Geyser Initiation, Microgravity Quarterly, Vol. 1(3), pp. 125-133, 1991i.

Hung, R. J., Shyu, K. L., and Lee, C. C., Cryogenic Liquid Resettlement Activated by Impulsive Thrust in Microgravity Environment, Advances in Cryogenic Engineering, 37, 1313-1326, 1991a.

Hung, R. J., Shyu, K. L., and Lee, C. C., Slosh Wave Excitation Due to Cryogenic Liquid Reorientation in Space-Based Propulsion System, Advances in Cryogenic Engineering, 37, 1303-1312, 1991b.

Hung, R. J., Shyu, K. L., and Lee, C. C., Medium Frequency Impulsive Thrust Excited Slosh Waves During Propellant Reorientation with Geyser, Journal of Propulsion and Power, Vol. 8, pp. 778-785, 1992a.

Hung, R. J., Shyu, K. L., and Lee, C. C., Liquid Hydrogen Slosh Wave Excited by Constant Reverse Gravity Acceleration of Geyser Initiation, Journal of Spacecraft and Rockets, Vol. 29, pp. 523-528, 1992b.

Hung, R. J., Tsao, Y. D., Hong, B. B., and Leslie, F. W., Time Dependent Dynamical Behavior of Surface Tension on Rotating Fluids Under Microgravity Environment, Advances in Space Research, Vol. 8(12), pp. 205-213, 1989d.

Hung, R. J., Tsao, Y. D., Hong, B. B., and Leslie, F. W., Dynamics of Surface Tension in Microgravity Environment, Progress in Aeronautics and Astronautics, Vol. 127, pp. 124-150, 1990b.

Hung, R. J., Tsao, Y. D., Hong, B. B., and Leslie, F. W., Dynamical Behavior of Surface Tension on Rotating Fluids in Low and Microgravity Environments, International Journal for Microgravity Research and Applications, Vol. 11, pp. 81-95, 1989a.

Hung, R. J., Tsao, Y. D., Hong, B. B., and Leslie, F. W., Axisymmetric Bubble Profiles in a Slowly Rotating Helium Dewar Under Low and Microgravity Environments, Acta Astronautica, Vol. 19, pp. 411-426, 1989b.

Hung, R. J., Tsao, Y. D., Hong, B. B., and Leslie, F. W., Bubble Behaviors in a Slowly Rotating Helium Dewar in Gravity Probe-B Spacecraft Experiment, Journal of Spacecraft and Rockets, Vol. 26, pp. 167-172, 1989c.

Kamotani, Y., Prasad, A., and Oastrach, S., Thermal Convections in an Enclosure Due to Vibrations Aboard a Spacecraft, AIAA Journal, Vol. 19, pp. 511-516, 1981.

Landau, L. D., and Lifshitz, Fluid Mechanics, Pergamon Press, London, pp. 1-656, 1959.

Leslie, F. W., Measurements of Rotating Bubble Shapes in a Low Gravity Environment, _Journal of Fluid Mechanics_, Vol. 161, pp. 269-275, 1985.

Mason, P., Collins, D., Petrac, D., Yang, L., Edeskuty, F., Schuch, A., and Williamson, K., The Behavior of Superfluid Helium in Zero Gravity, _Proceedings 7th International Cryogenic Engineering Conferences_, Surrey, England, Science and Technology Press, 1978.

Misner, C. W., Thorne, K. S., and Wheeler, J. A., _Gravitation_, W. H. Freeman Co., San Francisco, CA, pp. 1-1279, 1973.

Stanford Relativity Gyroscope Experiment (NASA Gravity Probe-B), _Proceedings of Society of Photo-Optical Instrumentation Engineers_, _619_, pp. 1-165, Society of Photo-Optical Instrumentation Engineers, Bellingham, WA, 1986.

Weinberg, S., _Gravitation and Cosmology - Principles and Applications of General Relativity_, pp. 657, John Wiley and Sons, New York, 1972.

Wilks, J., _The Properties of Liquid and Solid Helium_, Clarendon Press, Oxford, U.K., 1967.

Wilkinson, D. T., Bender, P. I., Eardley, D. M., Gaisser, T. K., Hartle, J. B., Israel, M. H., Jones, L. W., Partridge, R. B., Schramm, D. N., Shapiro, I. I., Vessort, R. F. C., and Wagoner, R. V., Gravitation, Cosmology and Cosmic Ray Physics, _Physics Today_, _39_, 43-46, 1986.

Figure Captions

Figure 1 Time-dependent variation of angular position of spacecraft slew motion which operates at 90° angular displacement in 10 minutes.

Figure 2 Time-dependent variation of angular velocity of spacecraft slew motion which operates at 90° angular displacement in 10 minutes.

Figure 3 Time-dependent variation of angular acceleration of spacecraft slew motion which operates at 90° angular displacement in 10 minutes.

Figure 4 Three-dimensional cartesian coordinate (x'', y'', z'') used for spacecraft slew motion with axes at mass center of spacecraft, and coordinates (x, y, z) used in fluid mechanics computation.

Figure 5 AXAF-S spacecraft coordinate systems with azimuth angle ψ_E from spacecraft mass center to the center of the Earth. Coordinate (x'', y'', z'') for slew motion and coordinate(x, y, z) for fluid mechanics computation.

Figure 6 Geometry of the GP-B dewar container with the coordinate system perpendicular and tangential to the container wall. (A) Geometry in r-z plane and (B) Geometry in r-θ plane.

Figure 7 Geometry of the GP-B dewar container with baffle-boards and their locations. (A) Geometry in r-z plane and (B) Geometry in r-θ plane.

Figure 8 Distribution of grid points in the (A) Radial-axial plane, and (B) the radial-circumferential plane of the cylindrical coordinates for the AXAF-S dewar tank.

Figure 9 Time variation of AXAF-S spacecraft gravity gradient acceleration acting on fluid mass located at $(r, \theta, z) = (12\text{ cm}, \pi/2, 3\text{ cm})$ for 90° slew motion in 10 min. along the y''-axis and orbital period of 97.6 min. (A) Along x-direction; (B) Along y-direction; (C) Along z-direction.

Figure 10 Initial profiles of liquid-vapor interface for AXAF-S spacecraft of dewar tank under background gravity of 10^{-7} g_o and direction of background gravity at $\psi_E = 0°$. (A) In r-z plane at $\theta = 0°$ and 180°, (B) In r-θ plane at $\theta = 90°$ and 270°, (C) In r-θ plane at $z = 95.9$ cm, and (D) Three-dimensional liquid-vapor interface profile.

Figure 11 Time sequence evolution of AXAF-S spacecraft three-dimensional liquid-vapor interface oscillations for dewar driven by gravity gradient acceleration associated with slew motion in the y"-axis. 97.6 min orbital period and 90° slew motion in 10 min are applied to the spacecraft operation.

Figure 12 Time sequence evolution of AXAF-S spacecraft liquid-vapor interface oscillations for dewar tank in r-z plane at $\theta = 0°$ and 180°, driven by gravity gradient acceleration associated with slew motion in the y"-axis. 97.6 min orbital period and 90° slew motion in 10 min are applied to the spacecraft operation.

Figure 13 Time sequence evolution of AXAF-S the spacecraft liquid-vapor interface oscillations for rotating dewar in r-z plane at $\theta = 90°$ and 270°, driven by gravity gradient acceleration associated with slew motion in the y"-axis. 97.6 min orbital period and 90° slew motion in 10 min are applied to the spacecraft operation.

Figure 14 Time sequence evolution of the AXAF-S spacecraft liquid-vapor interface oscillations for rotating dewar in r-θ plane at height $z =$ 95.9 cm, driven by gravity gradient acceleration associated with slew motion in the y"-axis. 97.6 min orbital period and 90° slew motion in 10 min are applied to the spacecraft operation.

Figure 15 Time sequences of the AXAF-S spacecraft bubble mass center fluctuations due to the sloshing dynamics driven by gravity gradient acceleration associated with slew motion in the y-axis.

Figure 16 Time variation of AXAF-S spacecraft jitter acceleration associated with slew motion acting on fluid mass located at $(r, \theta, z) = (12$ cm, $\pi/2$, 3 cm) for 90° slew motion in 10 min. along the y"-axis and orbital period of 97.6 min. (A) Along x-direction; (B) Along y-direction; (C) Along z-direction.

Figure 17 Time sequence evolution of AXAF-S spacecraft three-dimensional liquid-vapor interface oscillations for dewar driven by jitter acceleration associated with slew motion in the y"-axis. 90° slew motion in 10 min is applied to the spacecraft operation.

Figure 18 Time sequence evolution of AXAF-S spacecraft liquid-vapor interface oscillations for dewar tank in r-z plane at $\theta = 0°$ and 180°, driven by jitter acceleration associated with slew motion in the y"-axis. 90° slew motion in 10 min is applied to the spacecraft operation.

Figure 19 Time sequence evolution of AXAF-S the spacecraft liquid-vapor interface oscillations for rotating dewar in r-z plane at $\theta = 90°$ and 270°, driven by gravity jitter acceleration associated with slew motion in the y"-axis. 90° slew motion in 10 min is applied to the spacecraft operation.

Figure 20 Time sequence evolution of the AXAF-S spacecraft liquid-vapor interface oscillations for rotating dewar in r-θ plane at height $z = 95.9$ cm, driven by gravity jitter acceleration associated with slew motion in the y"-axis. 90° slew motion in 10 min is applied to the spacecraft operation.

Figure 21 Time sequences of the AXAF-S spacecraft bubble mass center fluctuations due to the sloshing dynamics driven by jitter acceleration associated with slew motion in the y-axis. 90° slew motion in 10 min is applied to the spacecraft operation.

Figure 22 Time sequence of the AXAF-S spacecraft angular momentum fluctuations H_x, H_y, H_z) due to the sloshing dynamics driven by gravity gradient acceleration associated with slew motion in the y-axis.

Figure 23 Time sequences of the AXAF-S spacecraft fluid moment fluctuations due to sloshing dynamics driven by gravity gradient acceleration associated with slew motion in the y-axis. (A) For moment along x-direction; (B) For moment along y-direction; and (C) For moment along z-direction.

Figure 24 Time sequence of the AXAF-S spacecraft angular momentum fluctuations H_x, H_y, H_z) due to the sloshing dynamics driven by gravity jitter acceleration associated with slew motion in the y-axis. 90° slew motion in 10 minutes is applied to spacecraft operation.

Figure 25 Time sequences of the AXAF-S spacecraft fluid moment fluctuations due to sloshing dynamics driven by gravity jitter acceleration associated with slew motion in the y-axis. 90° slew motion in 10 minutes is applied to spacecraft motion. (A) For moment along x-direction; (B) For moment along y-direction; and (C) For moment along z-direction.

Figure 26 Time sequence of the fluctuations of fluid stress forces exerted on the AXAF-S dewar container due to the sloshing dynamics driven by gravity gradient acceleration associated with slew motion. (A) Along x-direction; (B) Along y-direction; and (C) Along z-direction.

Figure 27 Time sequence of the fluctuations of fluid stress moment exerted on the AXAF-S dewar container due to the sloshing dynamics driven by gravity gradient acceleration associated with slew motion in the y-axis (A) Along x-direction; (B) Along y-direction; and (C) Along z-direction.

Figure 28 Time sequence of the fluctuations of moment arm of viscous stress moment exerted on the AXAF-S dewar container due to the sloshing dynamics driven by gravity gradient acceleration associated with slew motion. (A) Along x-direction (pitching moment); (B) Along y-direction (yawing moment); and (C) Along z-direction (rolling moment).

Figure 29 Time sequence of the fluctuations of fluid stress forces exerted on the AXAF-S dewar container due to the sloshing dynamics driven by gravity jitter acceleration associated with slew motiony. (A) Along x-direction; (B) Along y-direction; and (C) Along z-direction.

Figure 30 Time sequence of the fluctuations of fluid stress moment exerted on the AXAF-S dewar container due to the sloshing dynamics driven by gravity jitter acceleration associated with slew motion in the y-axis (A) Along x-direction; (B) Along y-direction; and (C) Along z-direction.

Figure 31 Time sequence of the fluctuations of moment arm of viscous stress moment exerted on the AXAF-S dewar container due to the sloshing dynamics driven by gravity jitter acceleration associated with slew motion. (A) Along x-direction (pitching moment); (B) Along y-direction (yawing moment); and (C) Along z-direction (rolling moment).

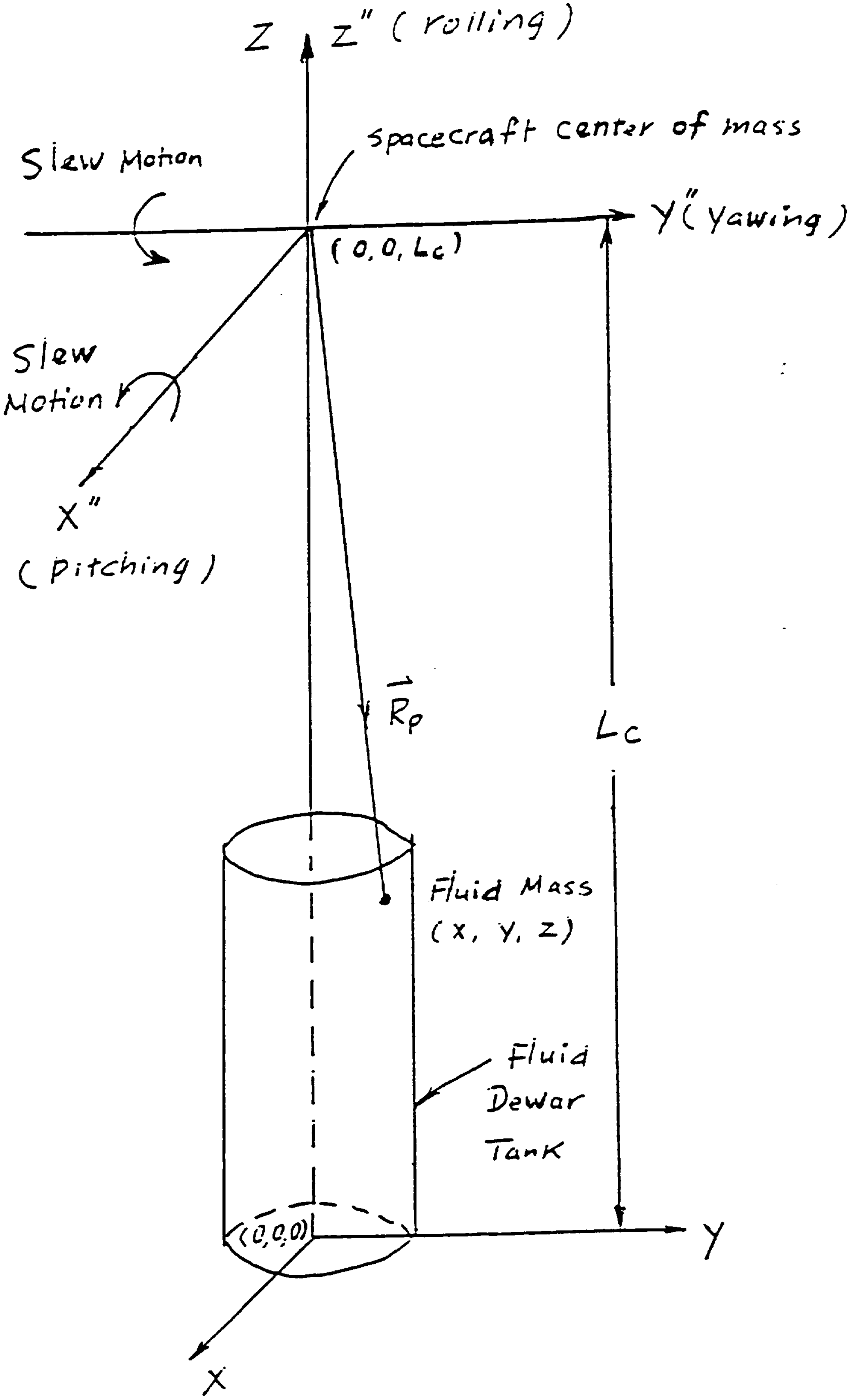
Z
Z" (rolling)
spacecraft center of mass
Slew Motion
Y" (yawing)
(0, 0, L_c)
Slew Motion
X"
(Pitching)
$\vec{R}_p$
L_c
Fluid Mass
(x, y, z)
Fluid Dewar Tank
(0, 0, 0)
Y
X

Fig. 1

ON ORBIT COORDINATE SYSTEM

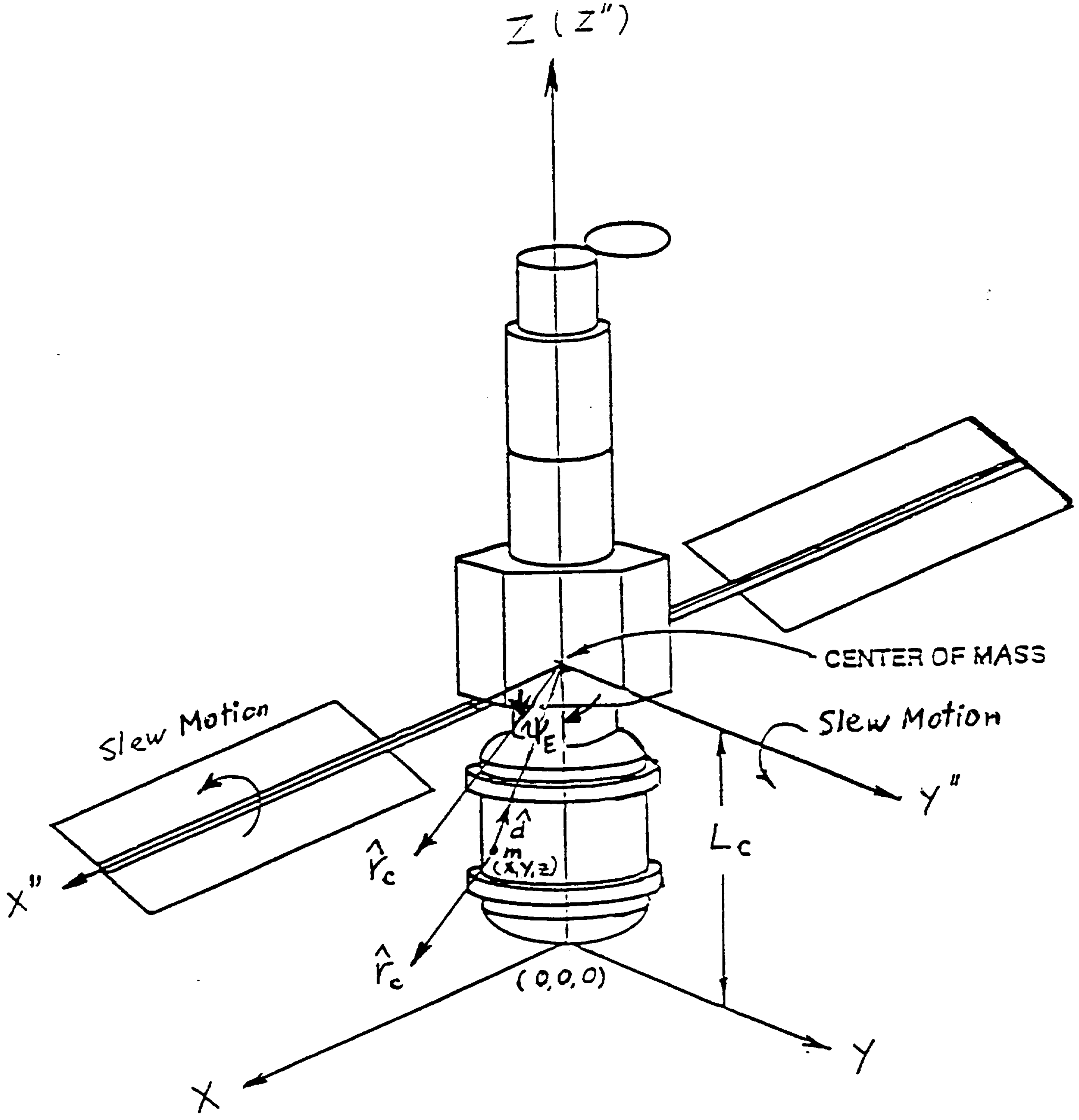

Figure 2

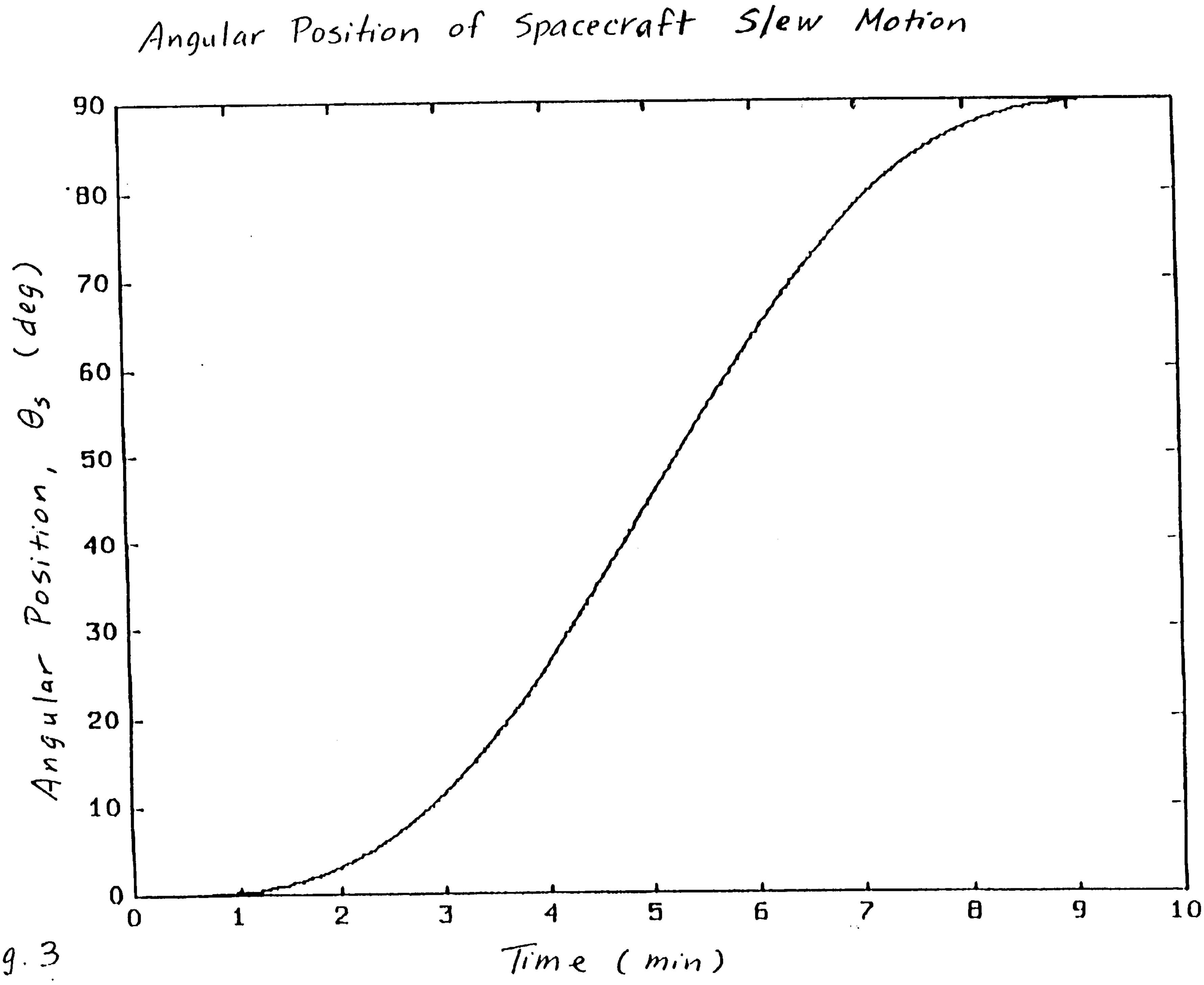
Angular Position of Spacecraft Slew Motion

Fig. 3

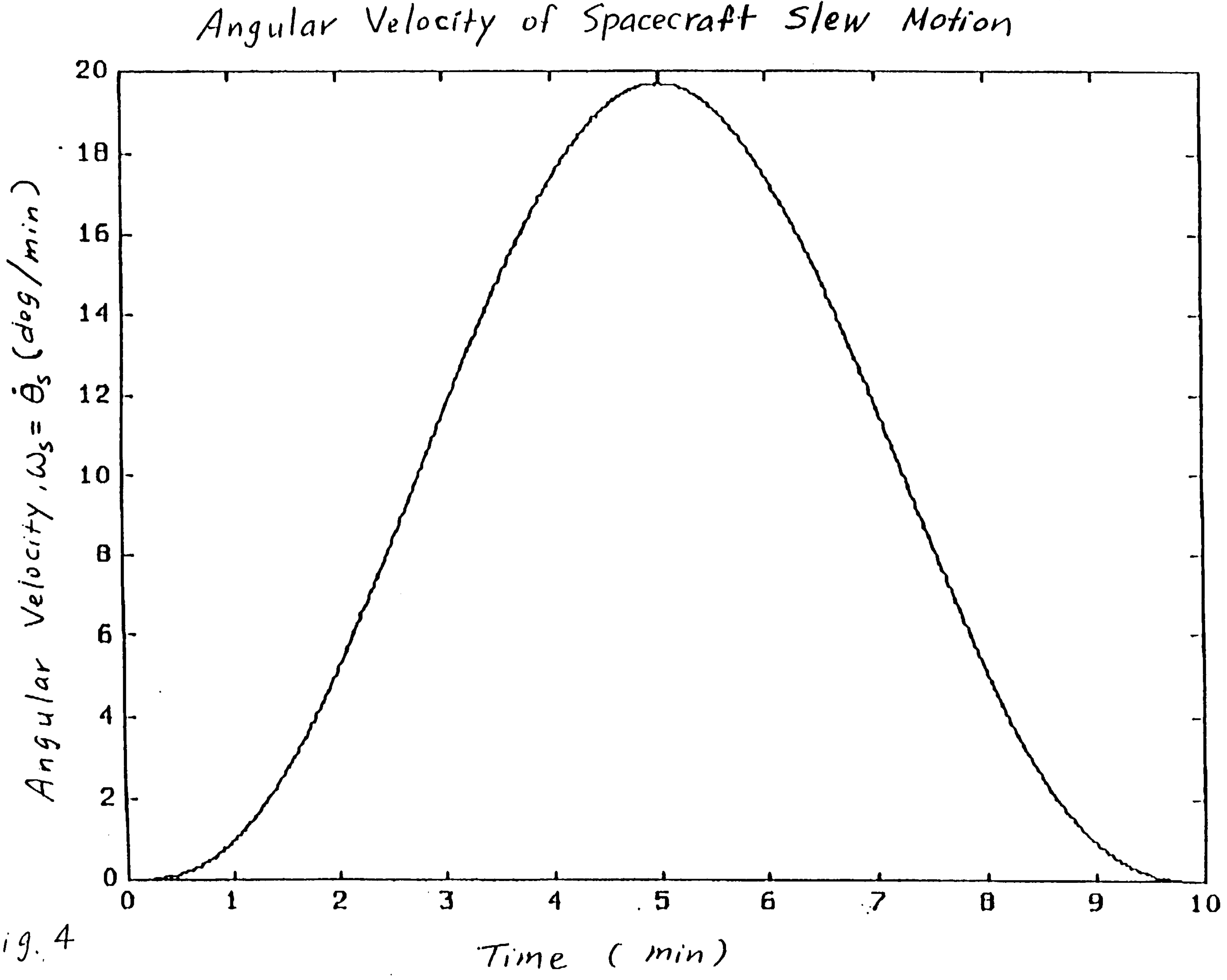
Angular Velocity of Spacecraft Slew Motion
Angular Velocity, $\omega_s = \dot{\theta}_s$ (deg/min)
20
18
16
14
12
10
8
6
4
2
0
0
1
2
3
4
5
6
7
8
9
10
Time (min)

Fig. 4

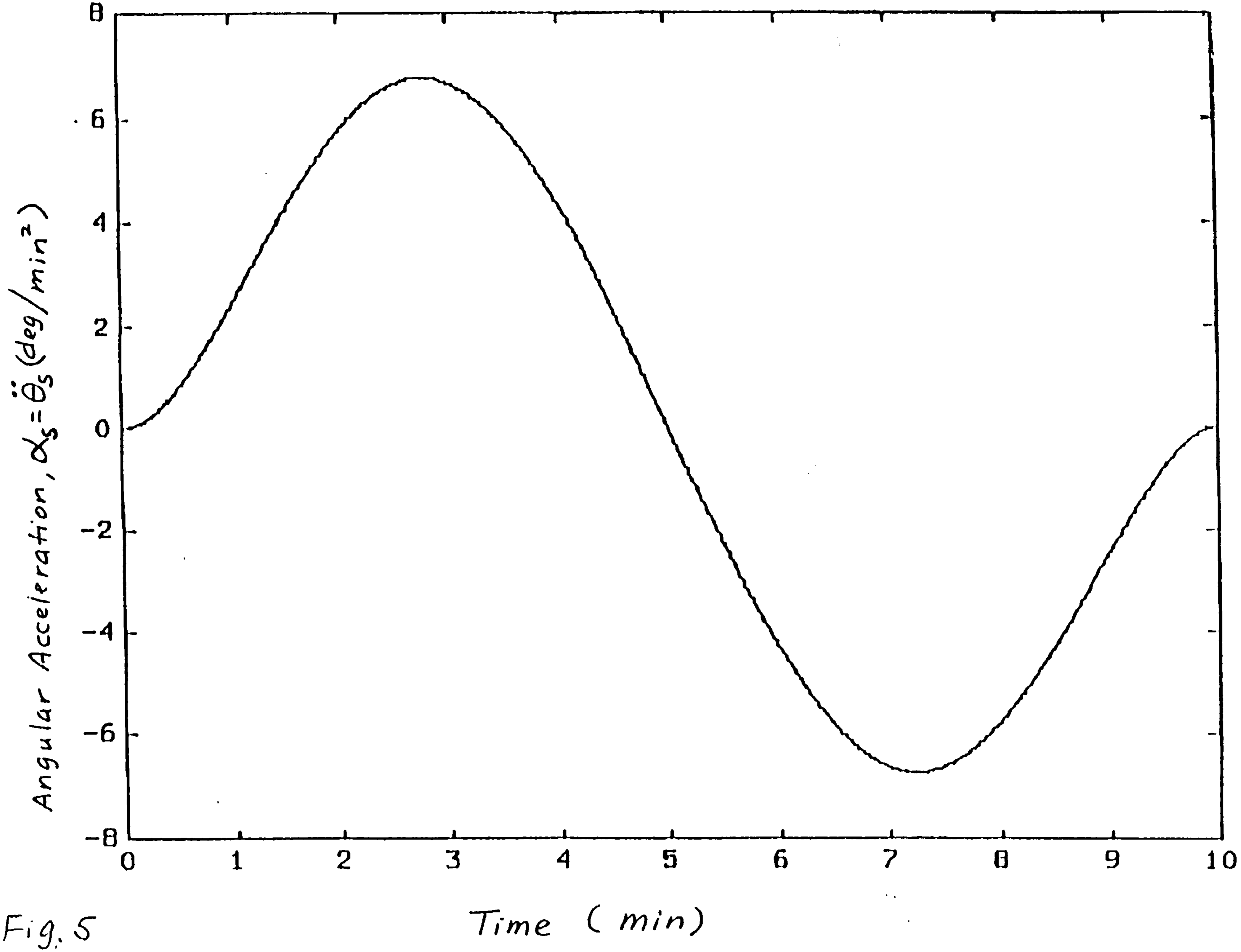

Angular Acceleration of Spacecraft Slew Motion

Fig. 5

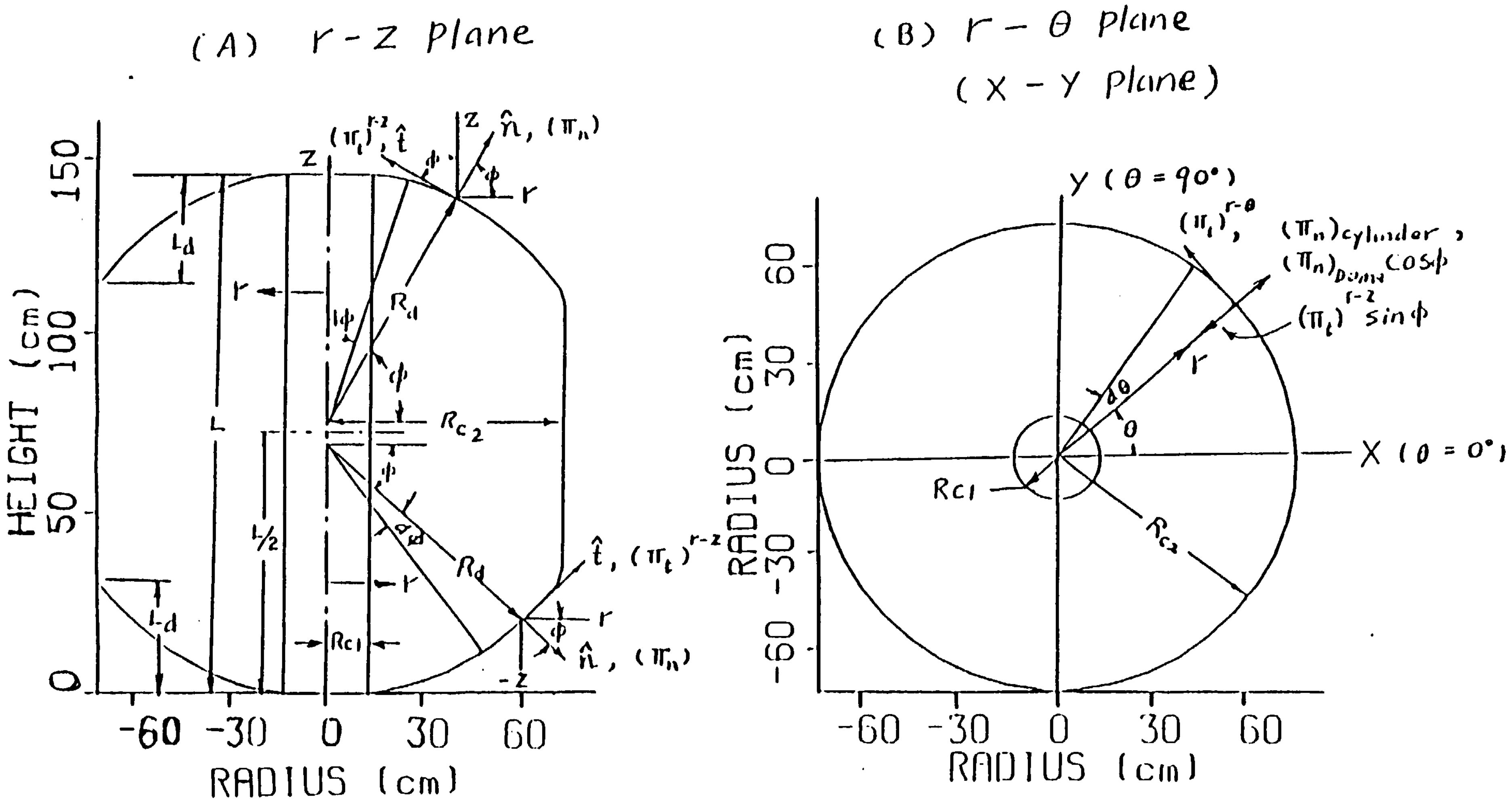
(A) r-Z Plane
(B) r-θ plane
(X-Y plane)
HEIGHT (cm)
150
100
50
0
-60
-30
0
30
60
RADIUS (cm)
Ld
L
L/2
r
Z
$(\pi_t)^{r\text{-}z}, \hat{t}$
$\hat{n}, (\pi_n)$
ϕ
R_d
R_{c2}
α_d
$\hat{t}, (\pi_t)^{r\text{-}z}$
-z
Rc1
Y (θ = 90°)
X (θ = 0°)
$(\pi_t)^{r\text{-}\theta}$,
$(\pi_n)_{cylinder}$,
$(\pi_n)_{Dome} \cos\phi$
$(\pi_t)^{r\text{-}z} \sin\phi$
dθ
θ
R_{c2}
RADIUS (cm)

Fig.6

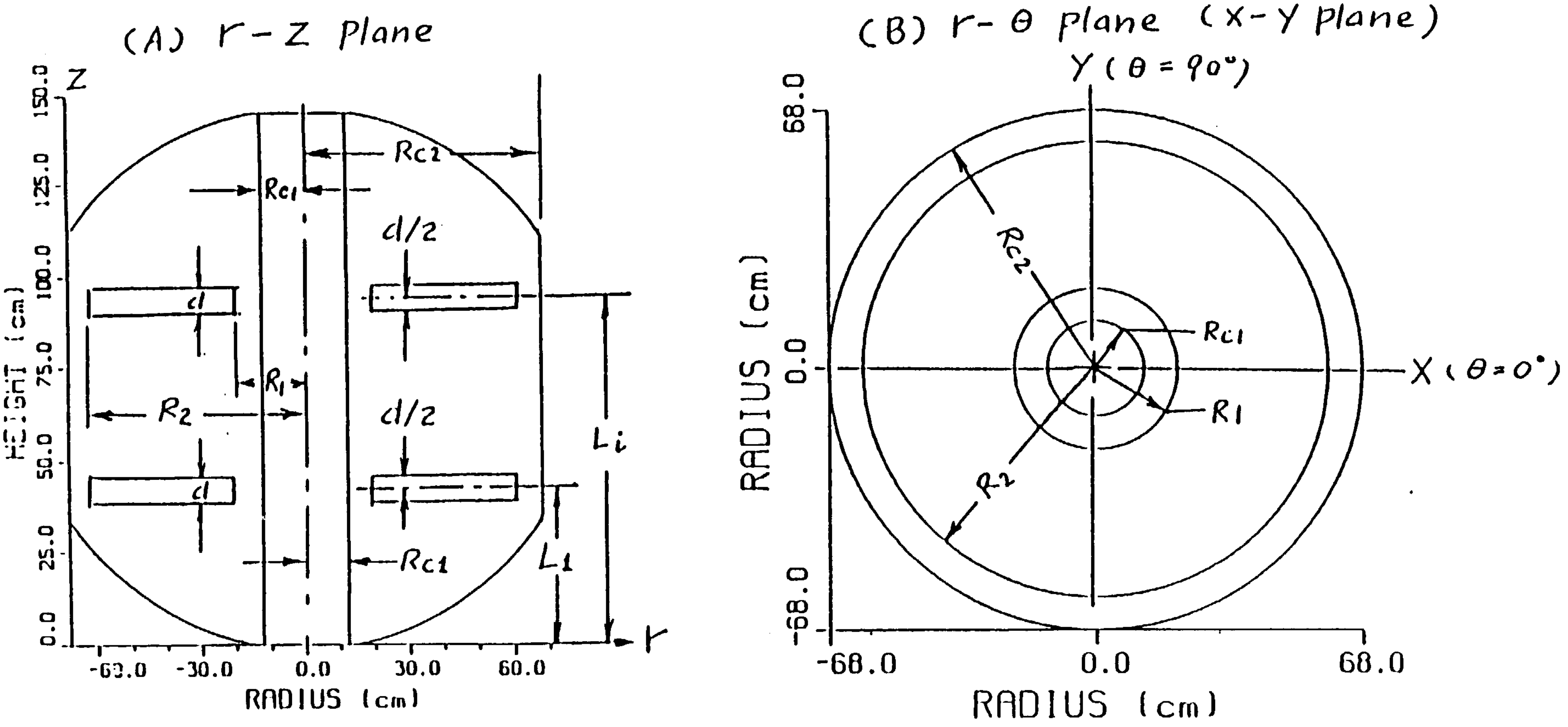
(A) r-Z Plane

(B) r-θ Plane (X-Y Plane)

Fig. 7

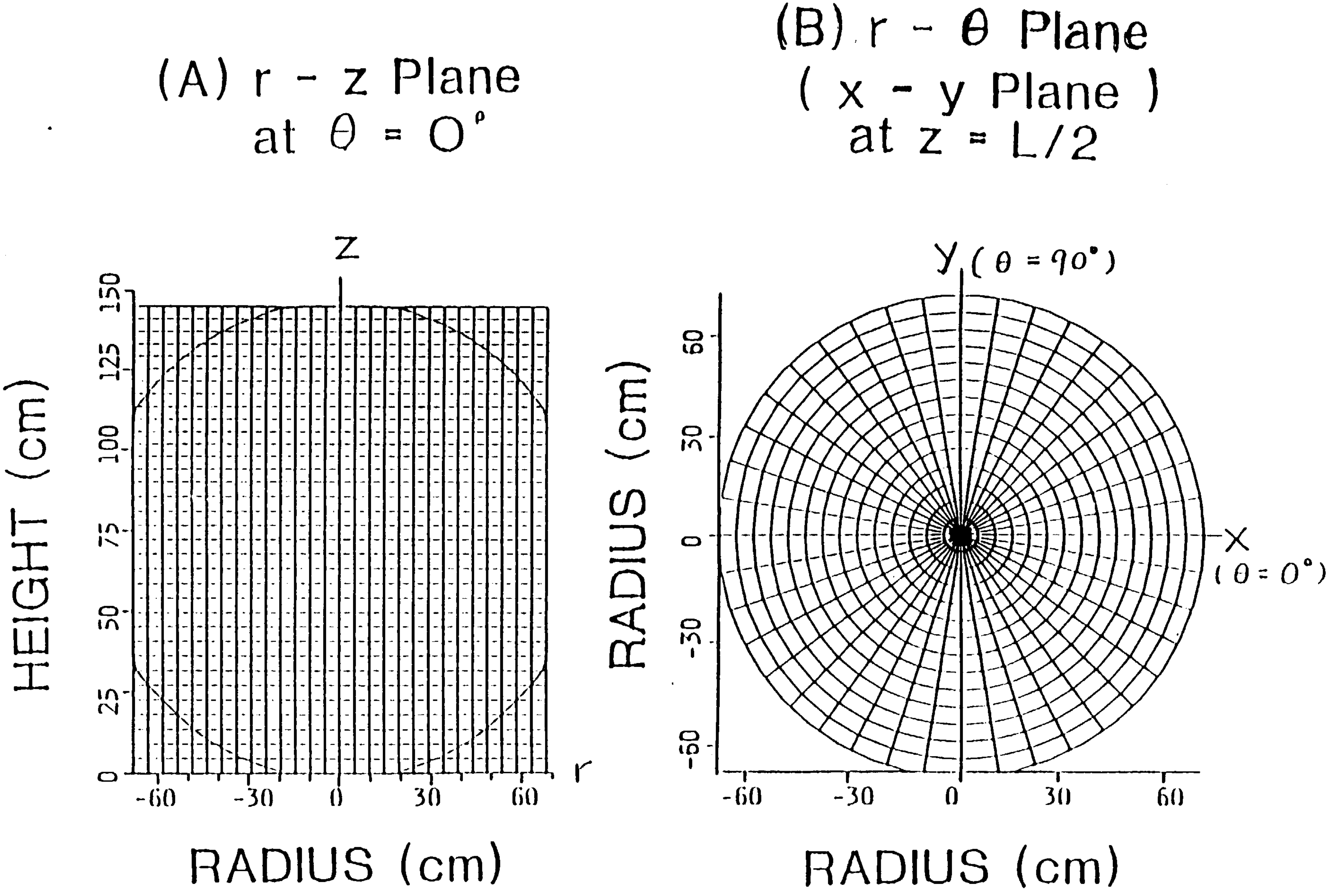

(A) r - z Plane at θ = O°

(B) r - θ Plane (x - y Plane) at z = L/2

Fig. 8

AXAF-S
Time Variation
of
Gravity Gradient
Acceleration
Associated With
Slew Motion

Acting on the
Fluid Mass Located
at
(r, θ, z)

$= (12\ \mathrm{cm}, \pi/2, 3\ \mathrm{cm})$

$g_0 = 9.81\ \mathrm{m/s^2}$

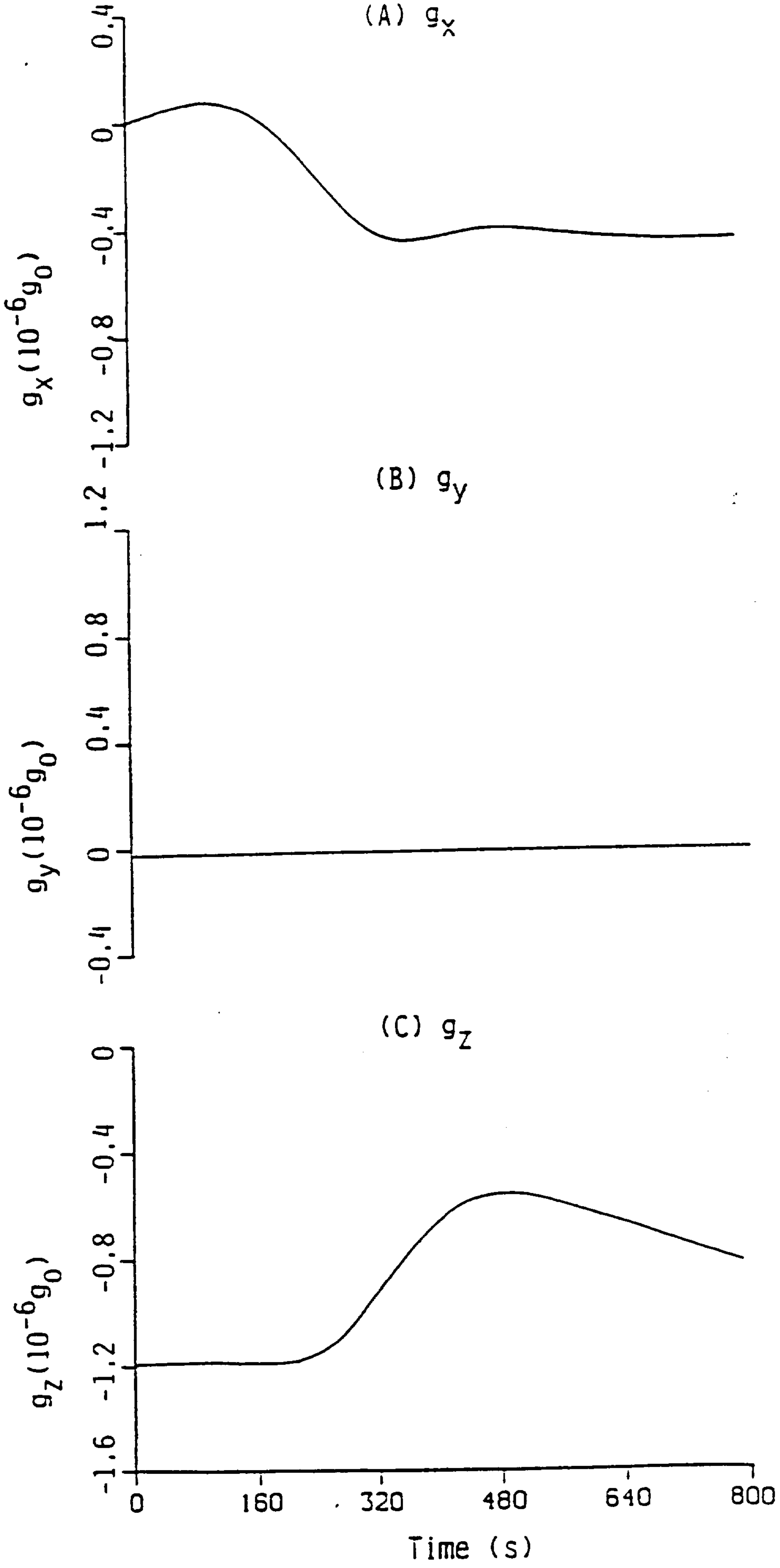

Fig. 9

INITIAL PROFILES OF LIQUID HELIUM AND VAPOR INTERFACE

AXAF Dewar, Liquid Filled Level = 70%

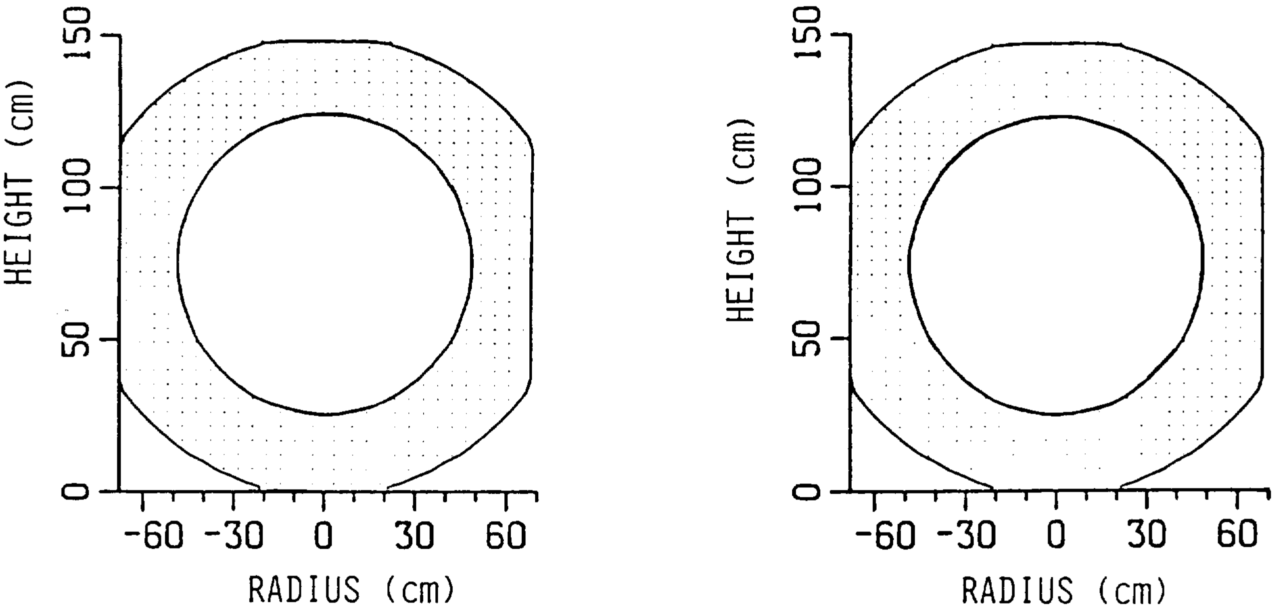
(A) r-z plane at θ = 0° and 180°

(B) r-z plane at θ = 90° and 180°

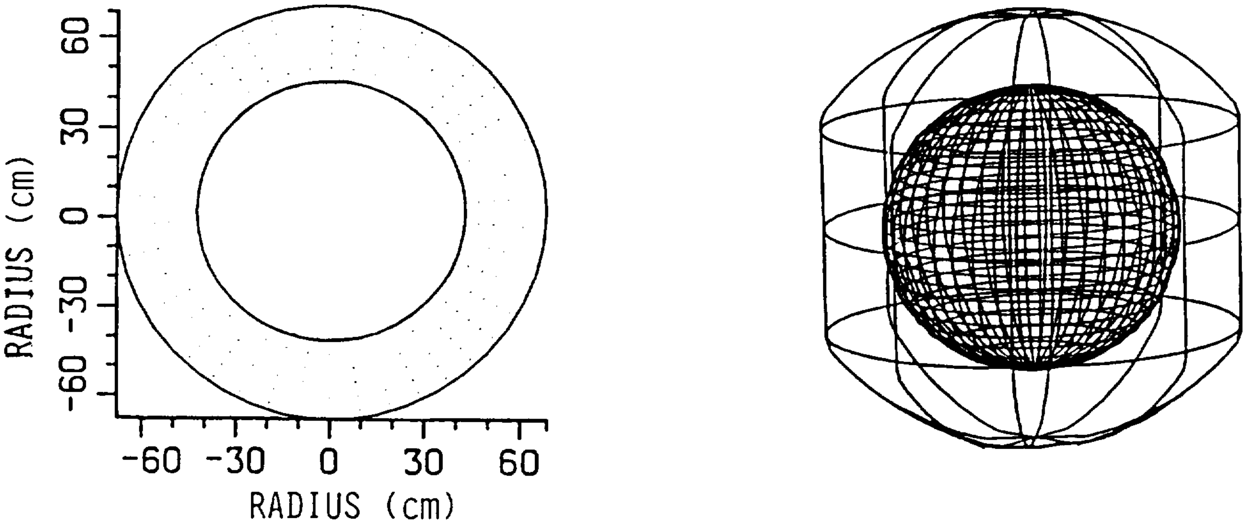
(C) r-θ plane at z = 95.9 cm

(D) Three Dimensional Profile

Fig. 10

SLOSHING DYNAMICS OF AXAF-S CRYOGENIC HELIUM II DEWAR
Driven by Gravity Gradient Acceleration, Liquid Filled Level = 70%

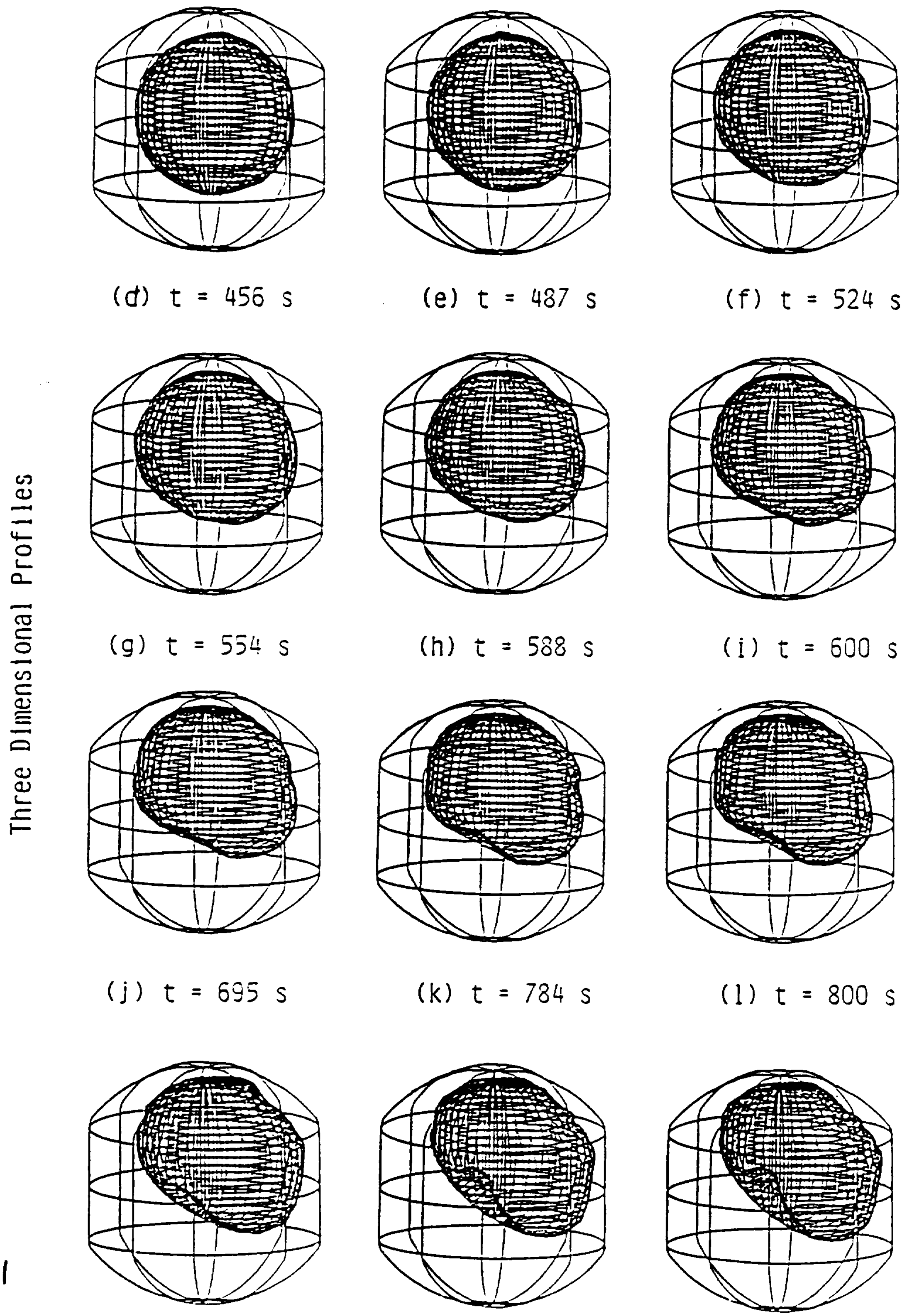

(a) t = 334 s (b) t = 392 s (c) t = 431 s

(d) t = 456 s (e) t = 487 s (f) t = 524 s

(g) t = 554 s (h) t = 588 s (i) t = 600 s

(j) t = 695 s (k) t = 784 s (l) t = 800 s

Fig 11

SLOSHING DYNAMICS OF AXAF-S CRYOGENIC HELIUM II DEWAR
Driven by Gravity Gradient Acceleration, Liquid Filled Level = 70%

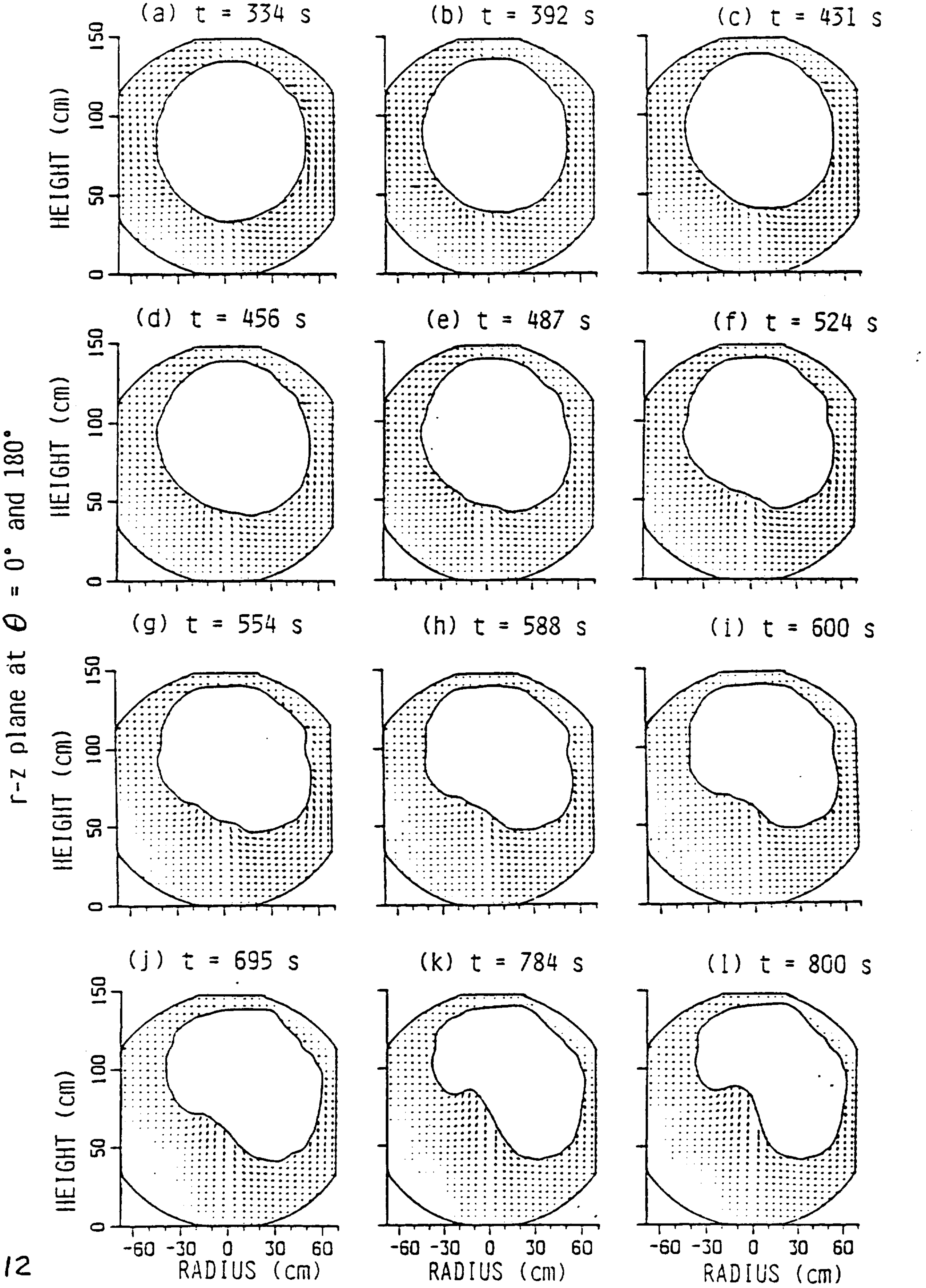

Fig. 12

SLOSHING DYNAMICS OF AXAF-S CRYOGENIC HELIUM II DEWAR
Driven by Gravity Gradient Acceleration, Liquid Filled Level = 70%

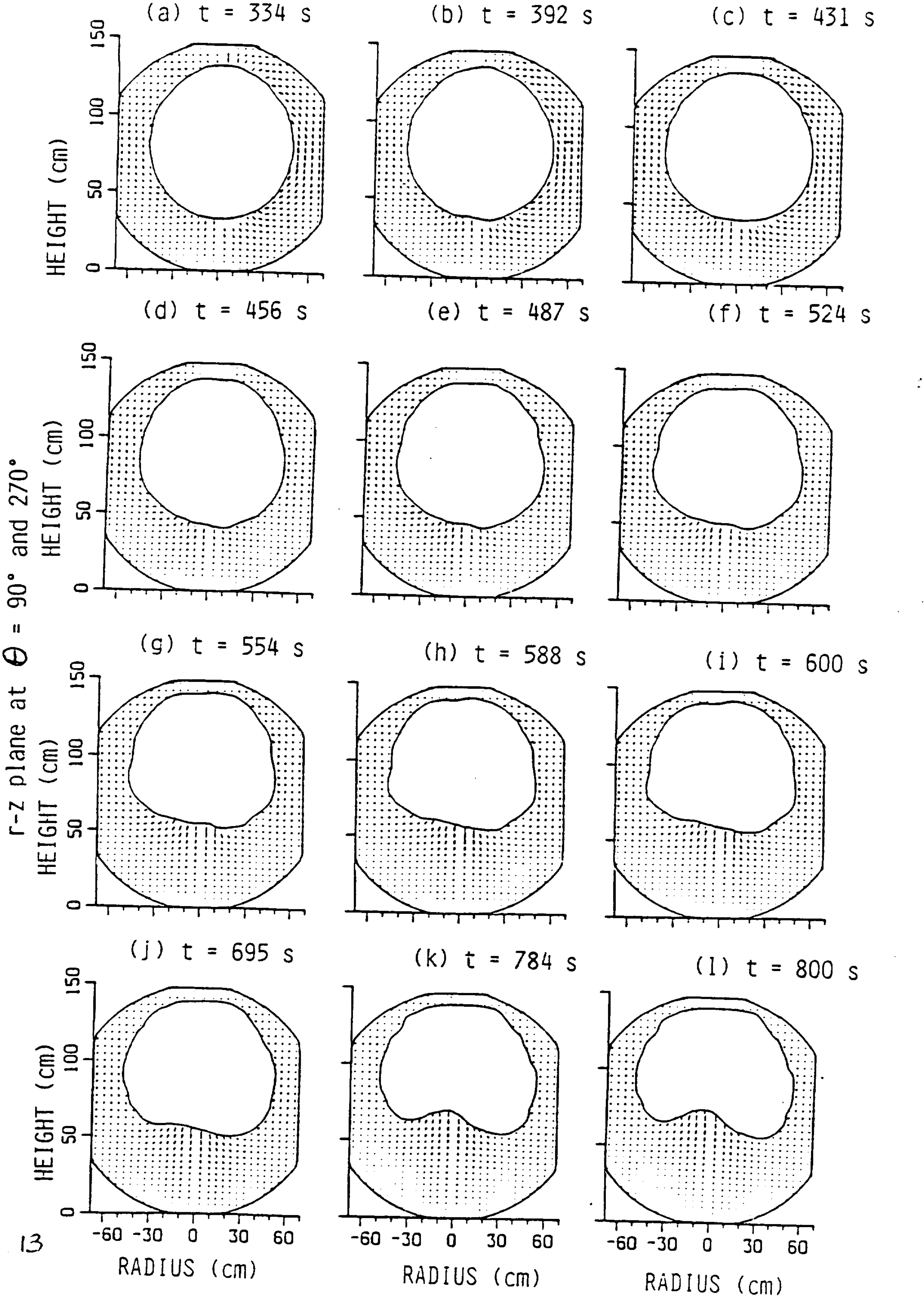

Fig 13

SLOSHING DYNAMICS OF AXAF-S CRYOGENIC HELIUM II DEWAR
Driven by Gravity Gradient Acceleration, Liquid Filled Level = 70%

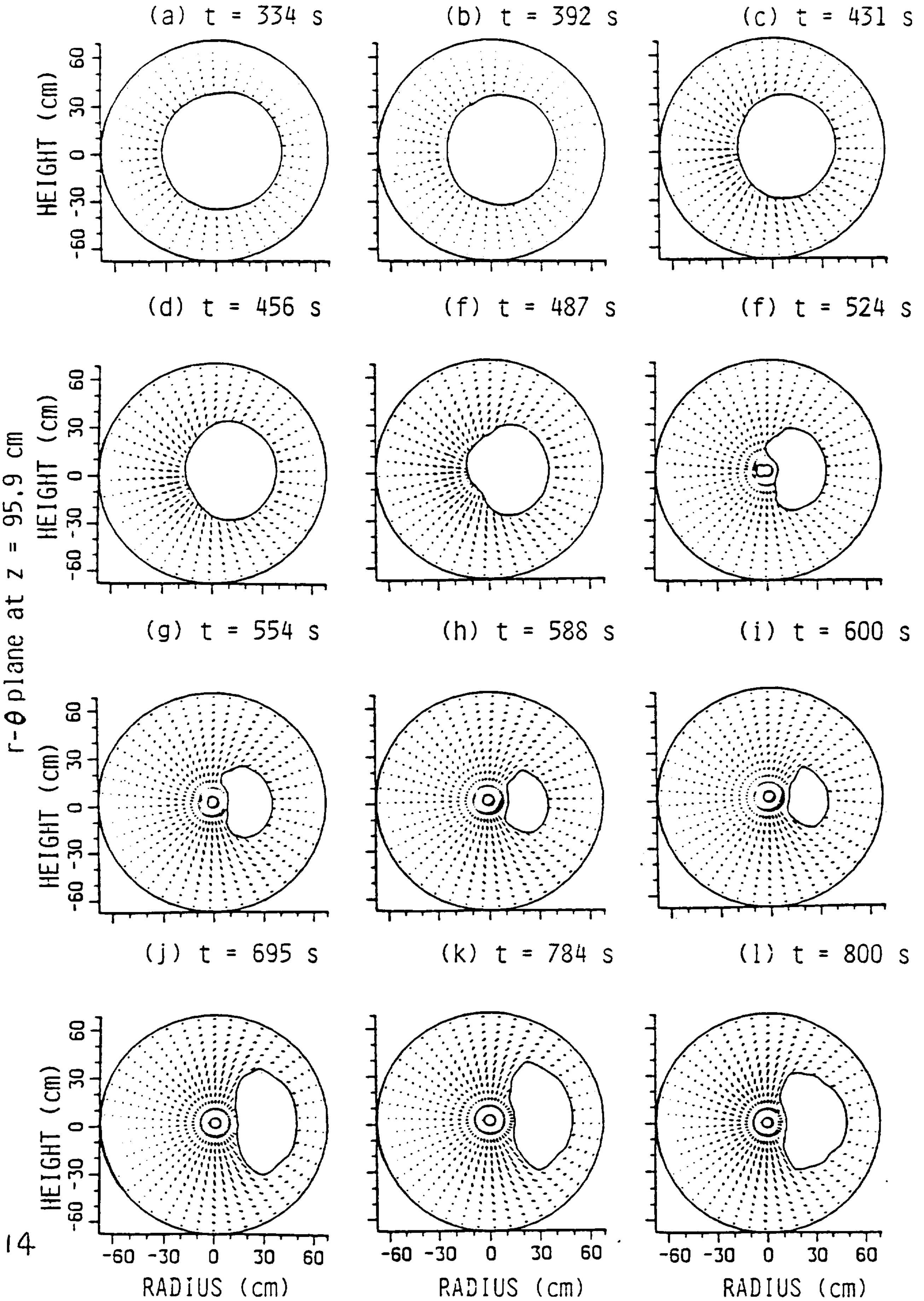
(a) t = 334 s
(b) t = 392 s
(c) t = 431 s
(d) t = 456 s
(f) t = 487 s
(f) t = 524 s
(g) t = 554 s
(h) t = 588 s
(i) t = 600 s
(j) t = 695 s
(k) t = 784 s
(l) t = 800 s

Fig. 14

AXAF-S

VARIATIONS OF

BUBBLE MASS CENTER

(x_c, y_c, z_c)

Driven by

Gravity Gradient

Acceleration

Associated With

Slew Motion

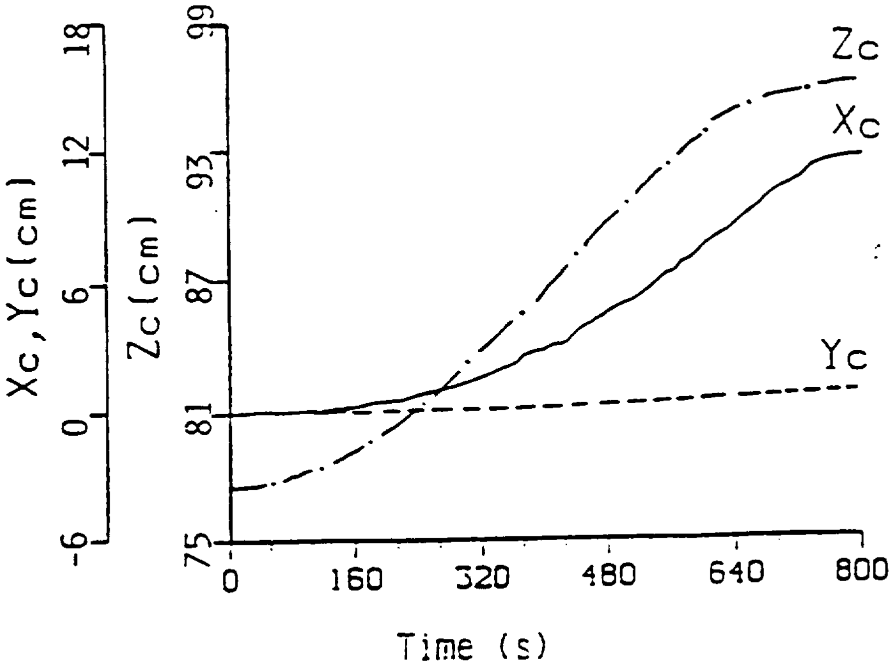

Fig. 15

AXAF-S
Time Variation
of Force Acceleration
Due to Slew
Motion
Acting on the Fluid
Mass Located at
(r, θ, z)

$= (12\ \text{cm}, \pi/2, 3\text{cm})$

$g_0 = 9.81\ \text{m/s}^2$

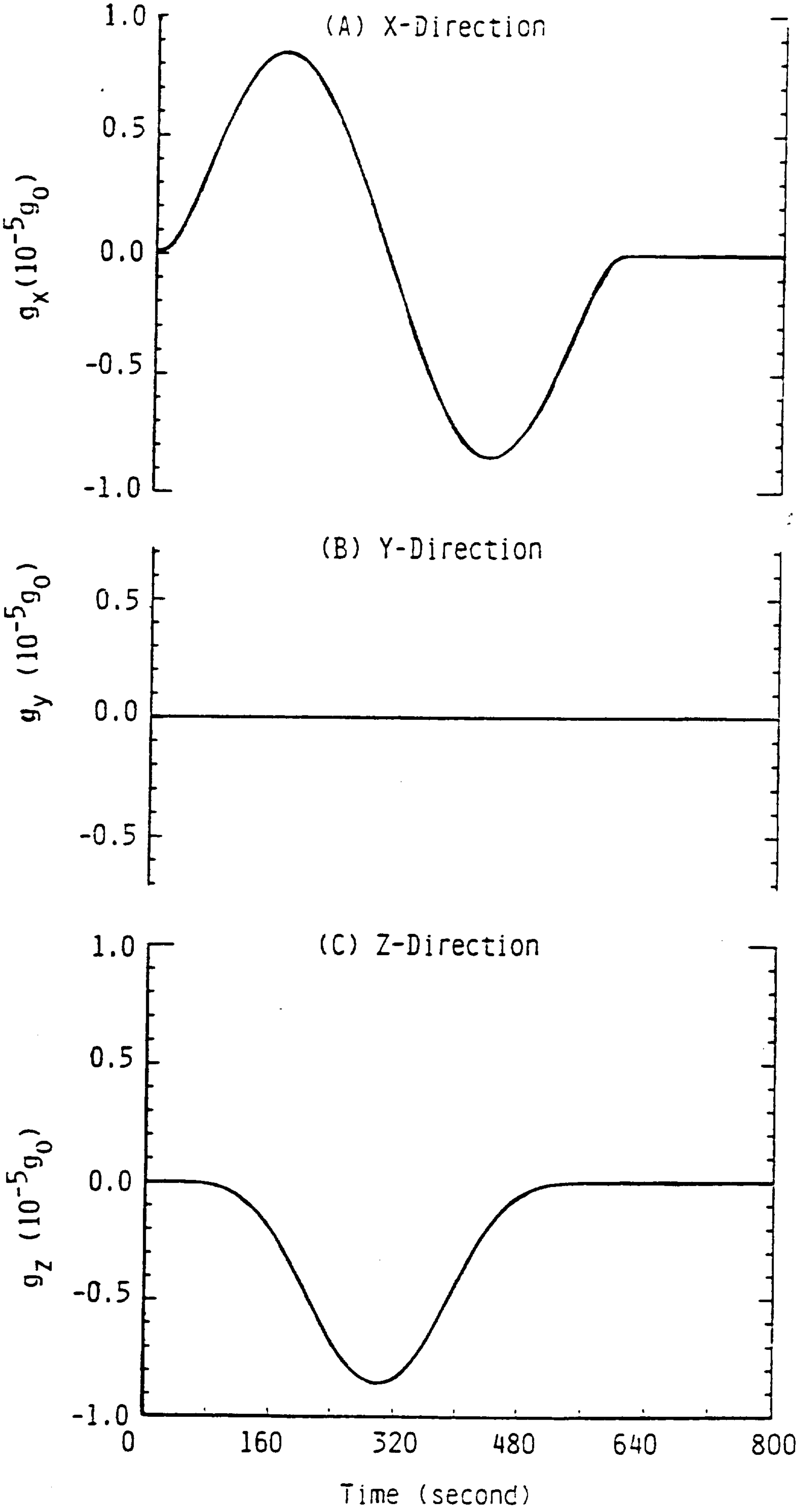

Fig. 16

SLOSHING DYNAMICS OF AXAF-S CRYOGENIC HELIUM II DEWAR, DRIVEN BY JITTER ACCELERATION WITH SLEW MOTION, Liquid Fill Level = 70%

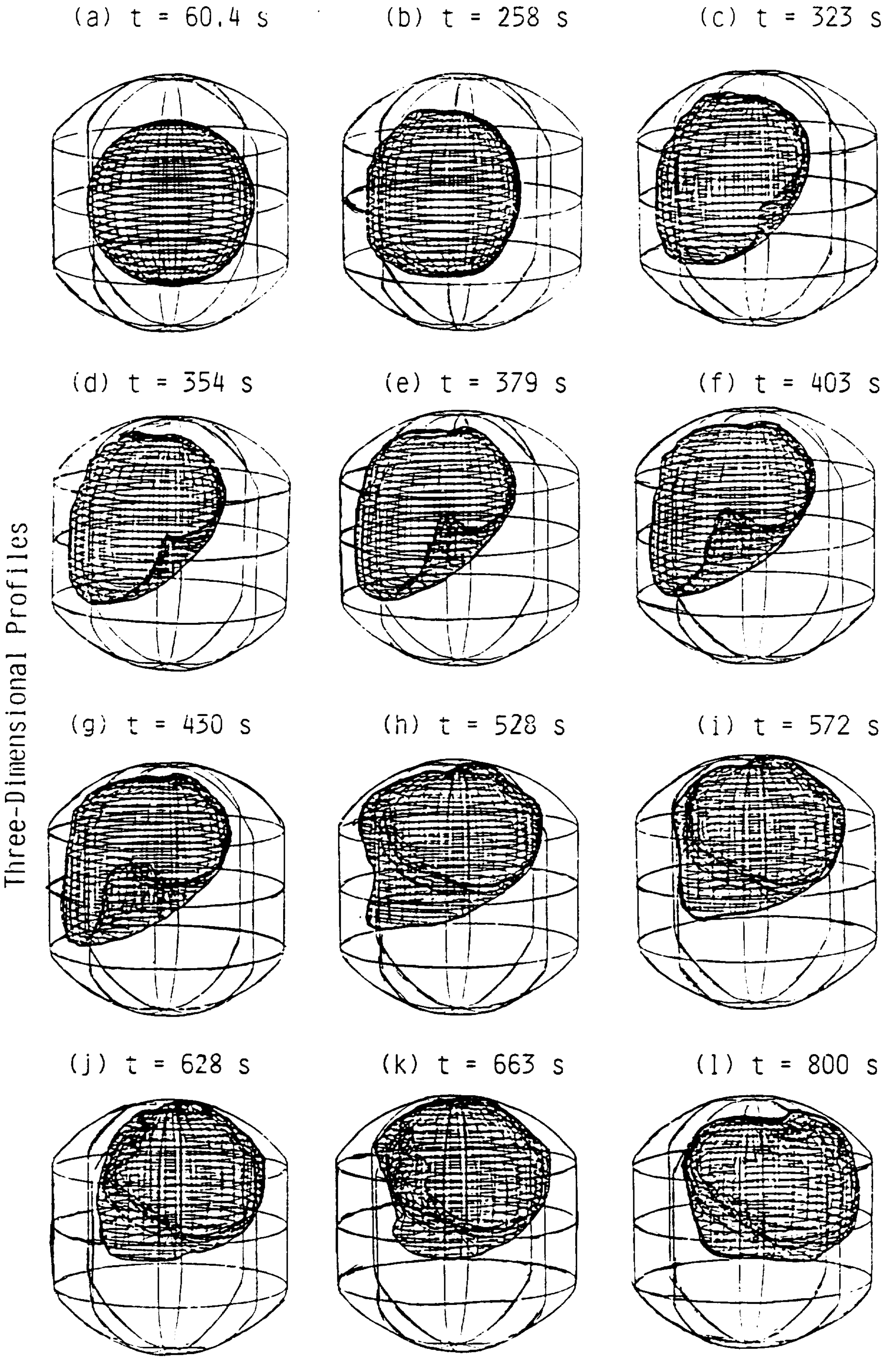

(a) t = 60.4 s
(b) t = 258 s
(c) t = 323 s
(d) t = 354 s
(e) t = 379 s
(f) t = 403 s
(g) t = 430 s
(h) t = 528 s
(i) t = 572 s
(j) t = 628 s
(k) t = 663 s
(l) t = 800 s

Fig.17

SLOSHING DYNAMICS OF AXAF-S CRYOGENIC HELIUM II DEWAR, DRIVEN BY JITTER ACCELERATION WITH SLEW MOTION, Liquid Fill Level = 70%

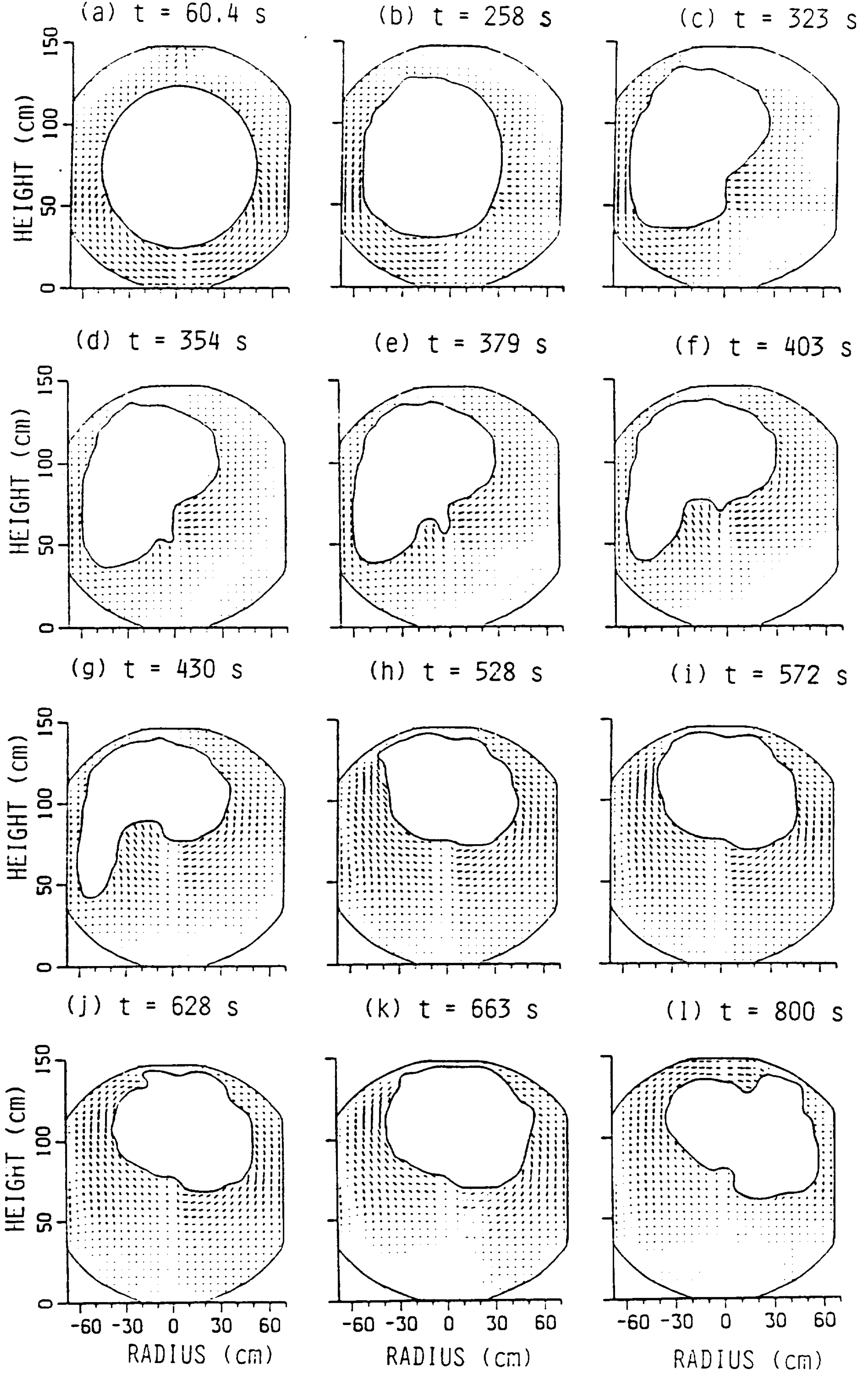
(a) t = 60.4 s (b) t = 258 s (c) t = 323 s

(d) t = 354 s (e) t = 379 s (f) t = 403 s

(g) t = 430 s (h) t = 528 s (i) t = 572 s

(j) t = 628 s (k) t = 663 s (l) t = 800 s

r-z plane at θ = 0° and 180°

Fig. 18

SLOSHNG DYNAMICS OF AXAF-S CRYOGENIC HELIUM II DEWAR, DRIVEN BY JITTER ACCELERATION WITH SLEW MOTION, Liquid Fill Level = 70%

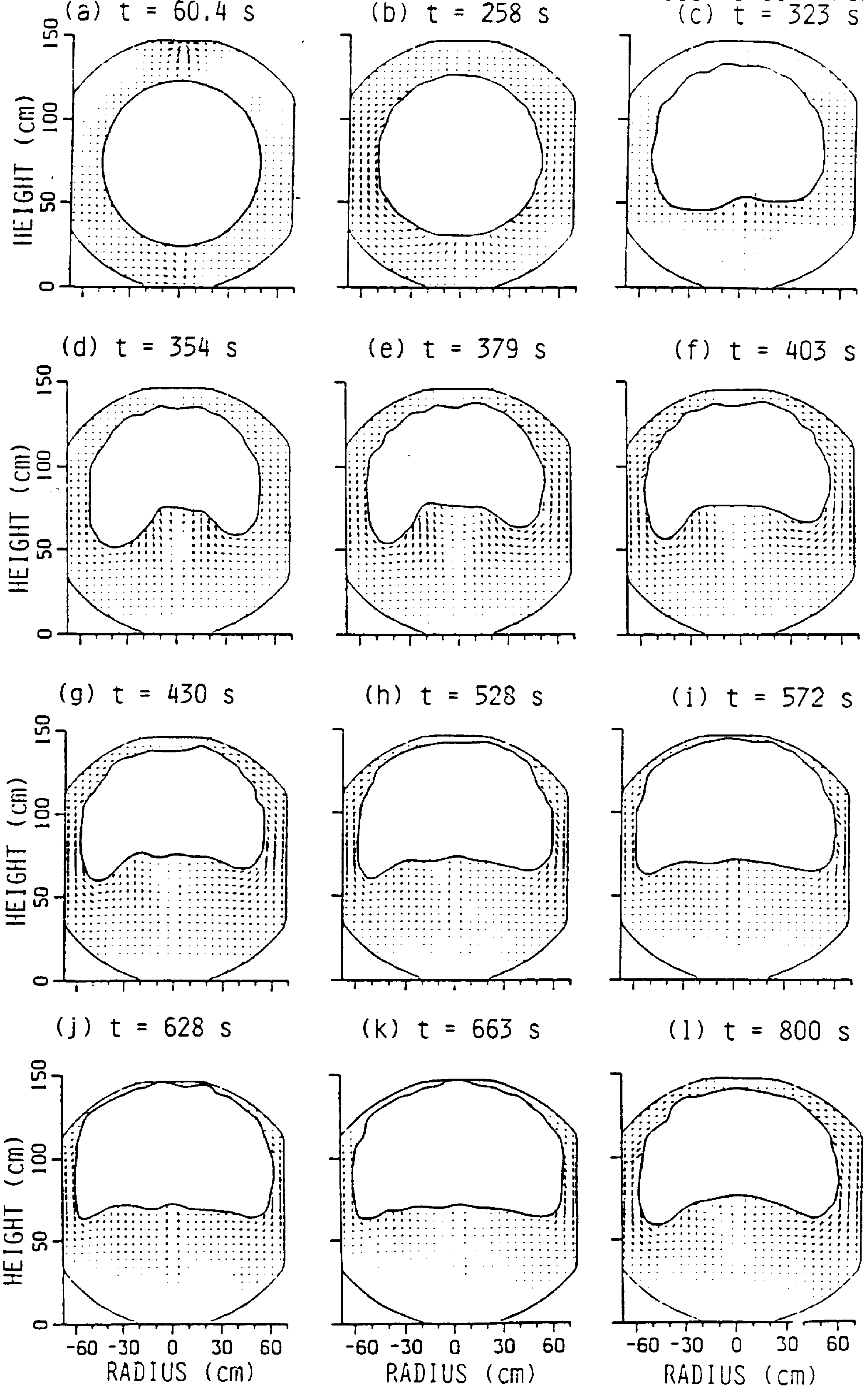
(a) t = 60.4 s
(b) t = 258 s
(c) t = 323 s
(d) t = 354 s
(e) t = 379 s
(f) t = 403 s
(g) t = 430 s
(h) t = 528 s
(i) t = 572 s
(j) t = 628 s
(k) t = 663 s
(l) t = 800 s

r-z plane at θ = 90° and 270°

Fig. 19

SLOSHING DYNAMICS OF AXAF-S CRYOGENIC HELIUM II DEWAR, DRIVEN BY JITTER ACCELERATION WITH SLEW MOTION, Liquid Fill Level = 70%

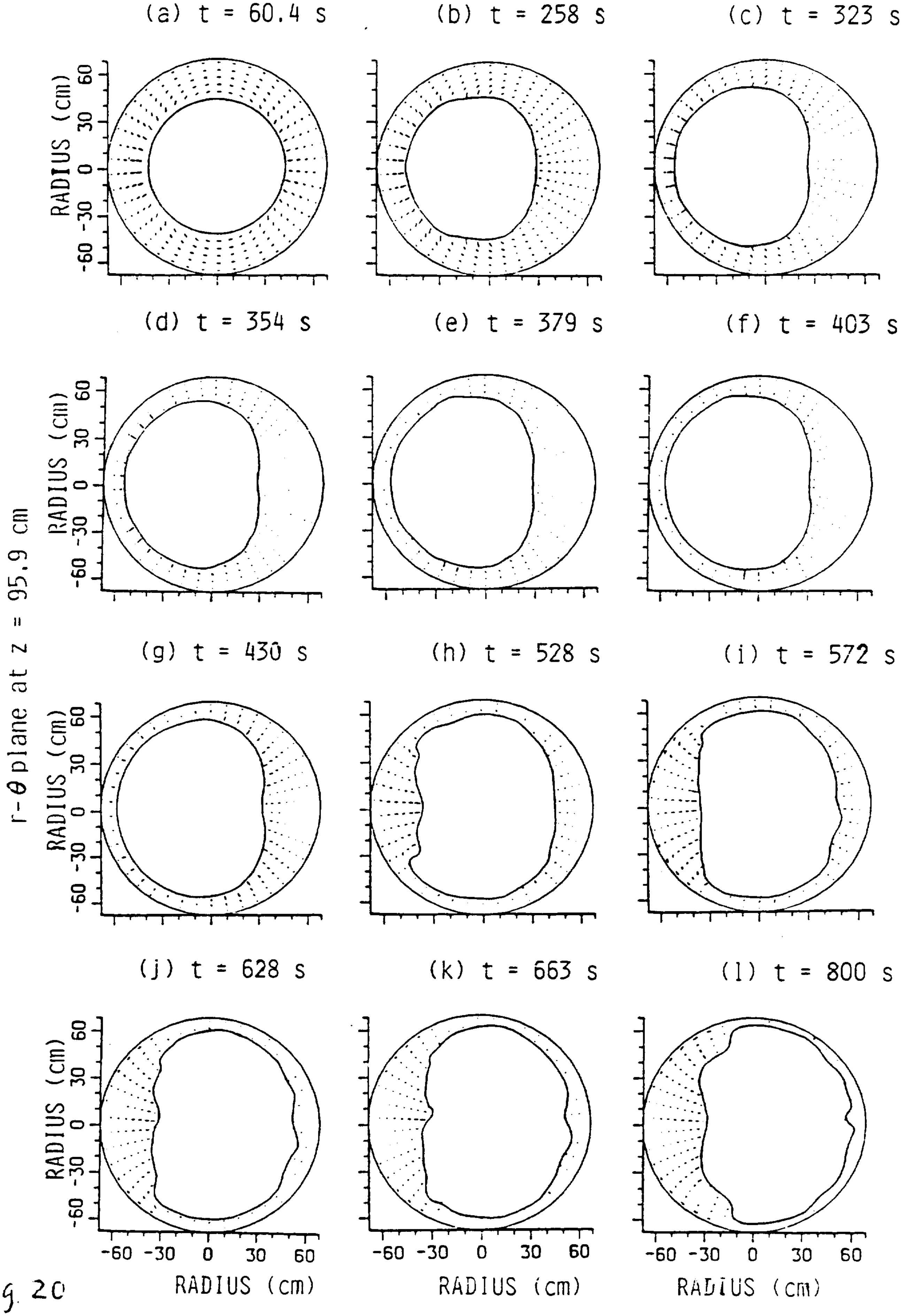
(a) t = 60.4 s (b) t = 258 s (c) t = 323 s

(d) t = 354 s (e) t = 379 s (f) t = 403 s

(g) t = 430 s (h) t = 528 s (i) t = 572 s

(j) t = 628 s (k) t = 663 s (l) t = 800 s

Fig. 20

AXAF-S SPACECRAFT

VARIATIONS OF BUBBLE MASS CENTER (X_c, Y_c, Z_c)

DRIVEN BY

JITTER ACCELERATION WITH SLEW MOTION

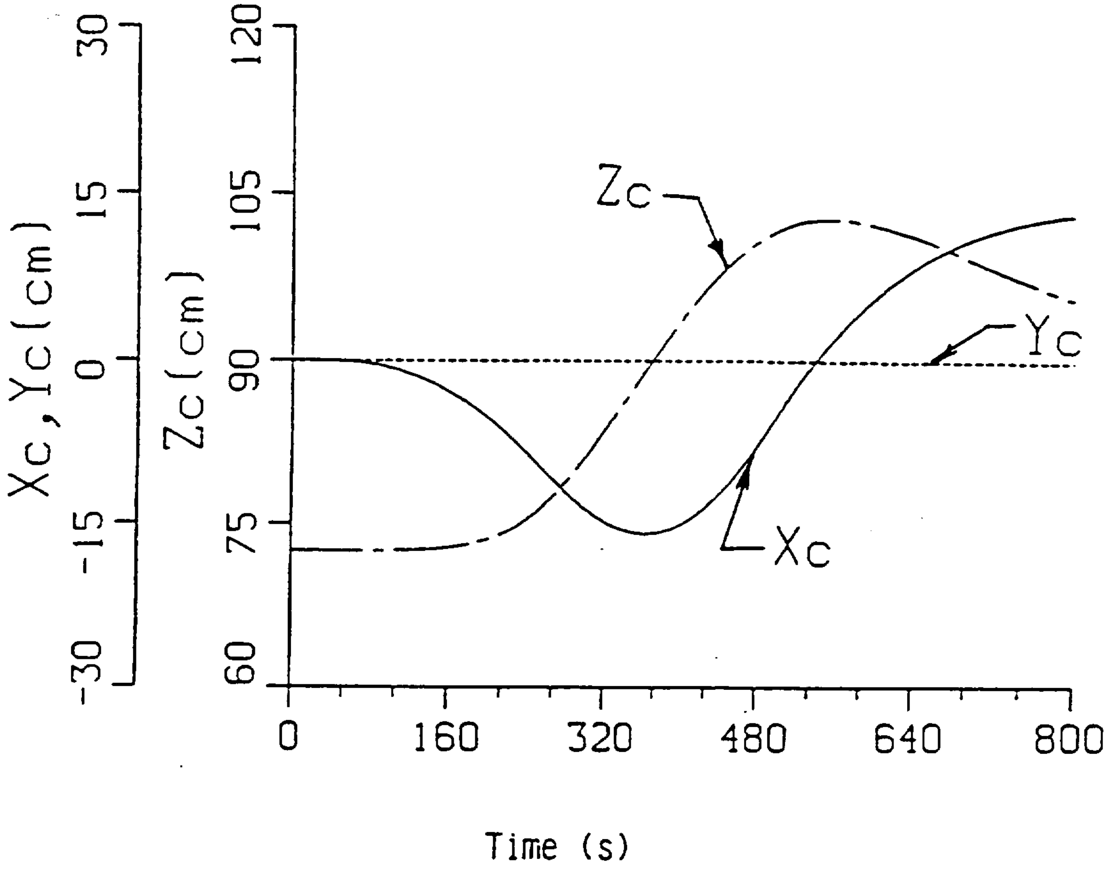

Fig. 21

AXAF-S

VARIATIONS OF
ANGULAR MOMENTUM
(H_x, H_y, H_z)

Driven by
Gravity Gradient
Acceleration
Associated With
Slew Motion

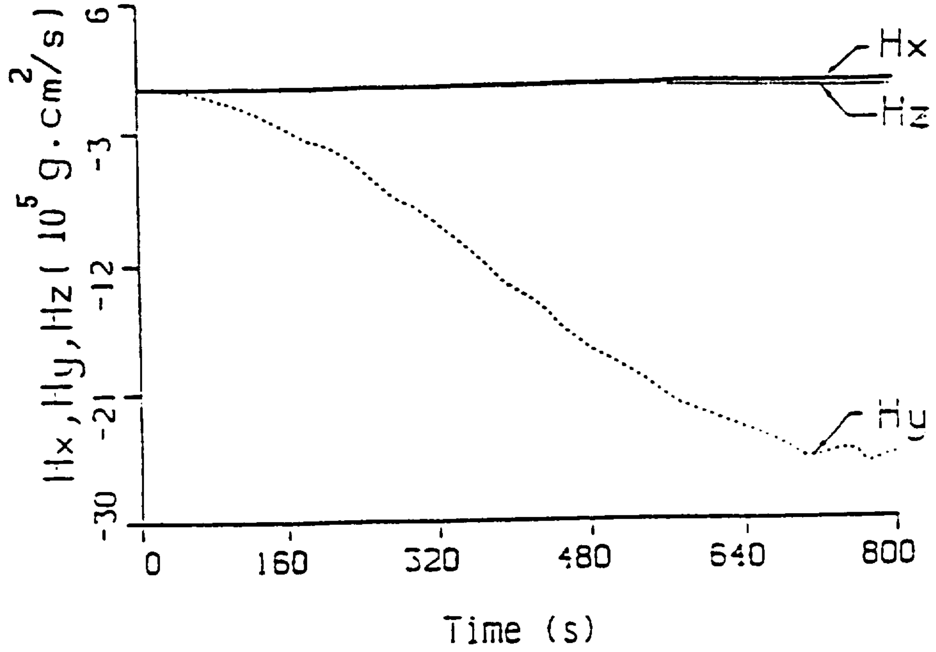

Fig. 22

AXAF-S
VARIATIONS OF
FLUID SYSTEM
MOMENT
(M_x, M_y, M_z)

Driven by
Gravity Gradient
Acceleration
Associated With
Slew Motion

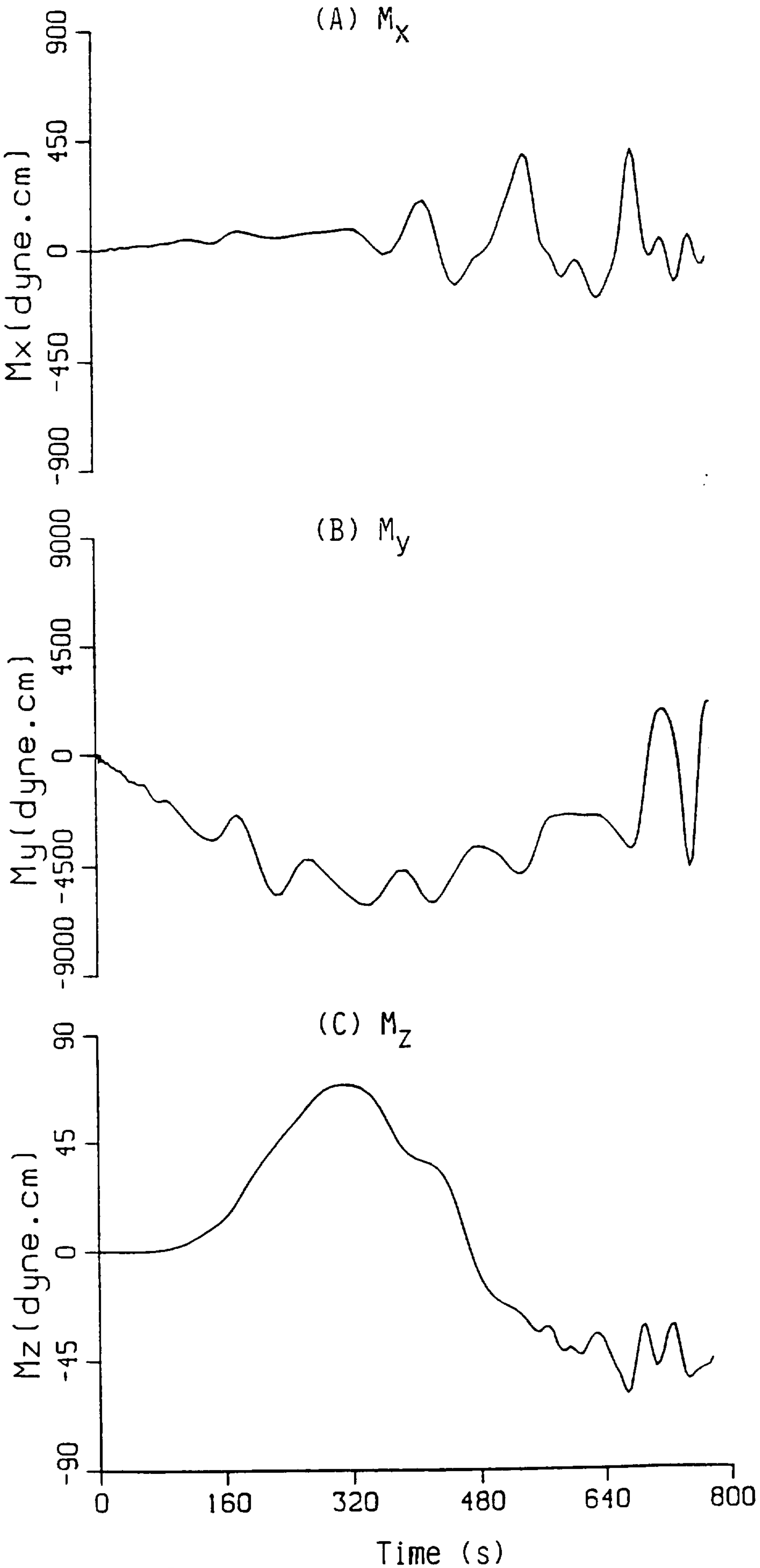

Fig. 23

AXAF-S
VARIATIONS OF ANGULAR
MOMENTUM
(H_x, H_y, H_z)

DRIVEN BY
JITTER ACCELERATION
ASSOCIATED WITH
SLEW MOTION

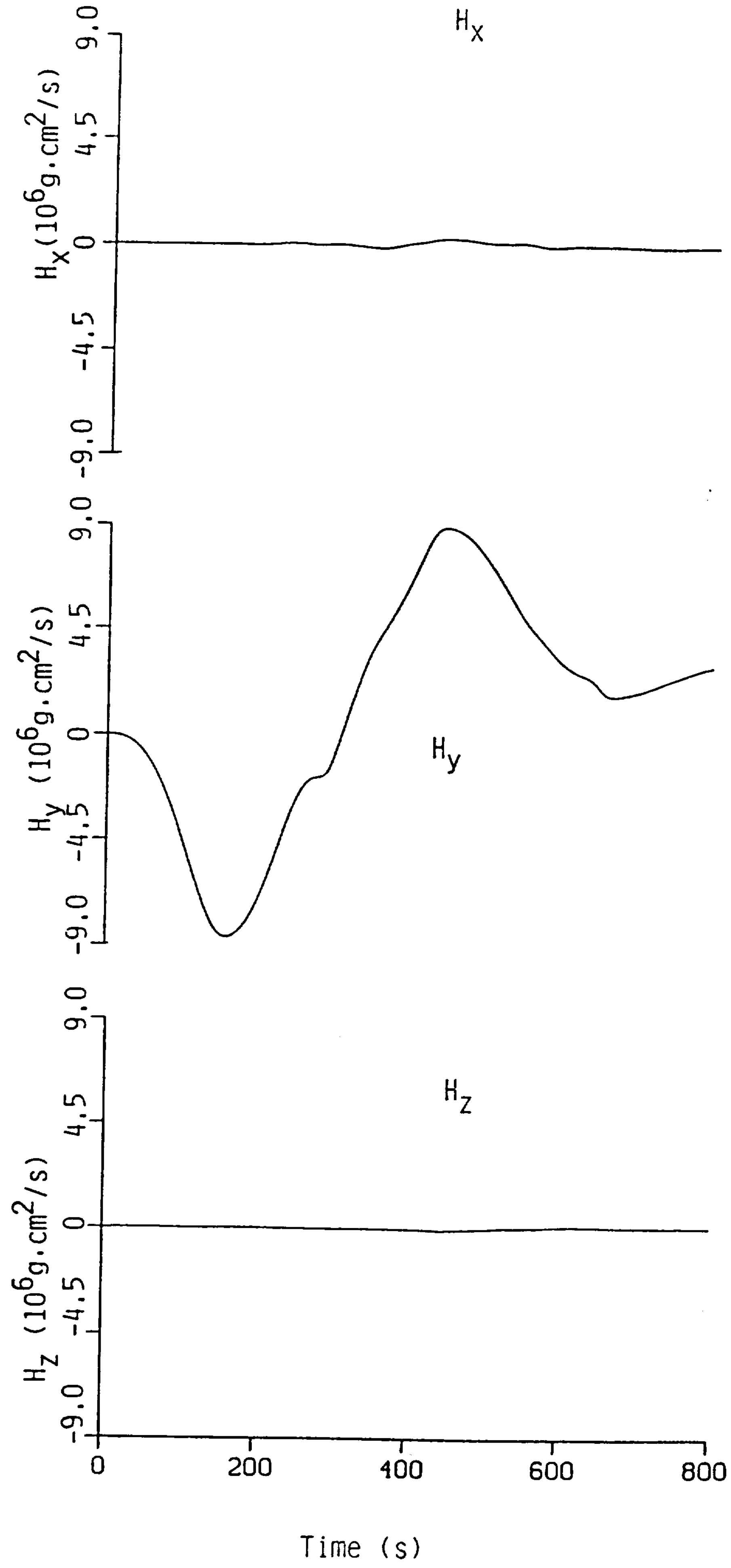

Fig. 24

AXAF-S
VARIATIONS OF FLUID
SYSTEM MOMENT

(M_x, M_y, M_z)

DRIVEN BY
JITTER ACCELERATION
ASSOCIATED WITH
SLEW MOTION

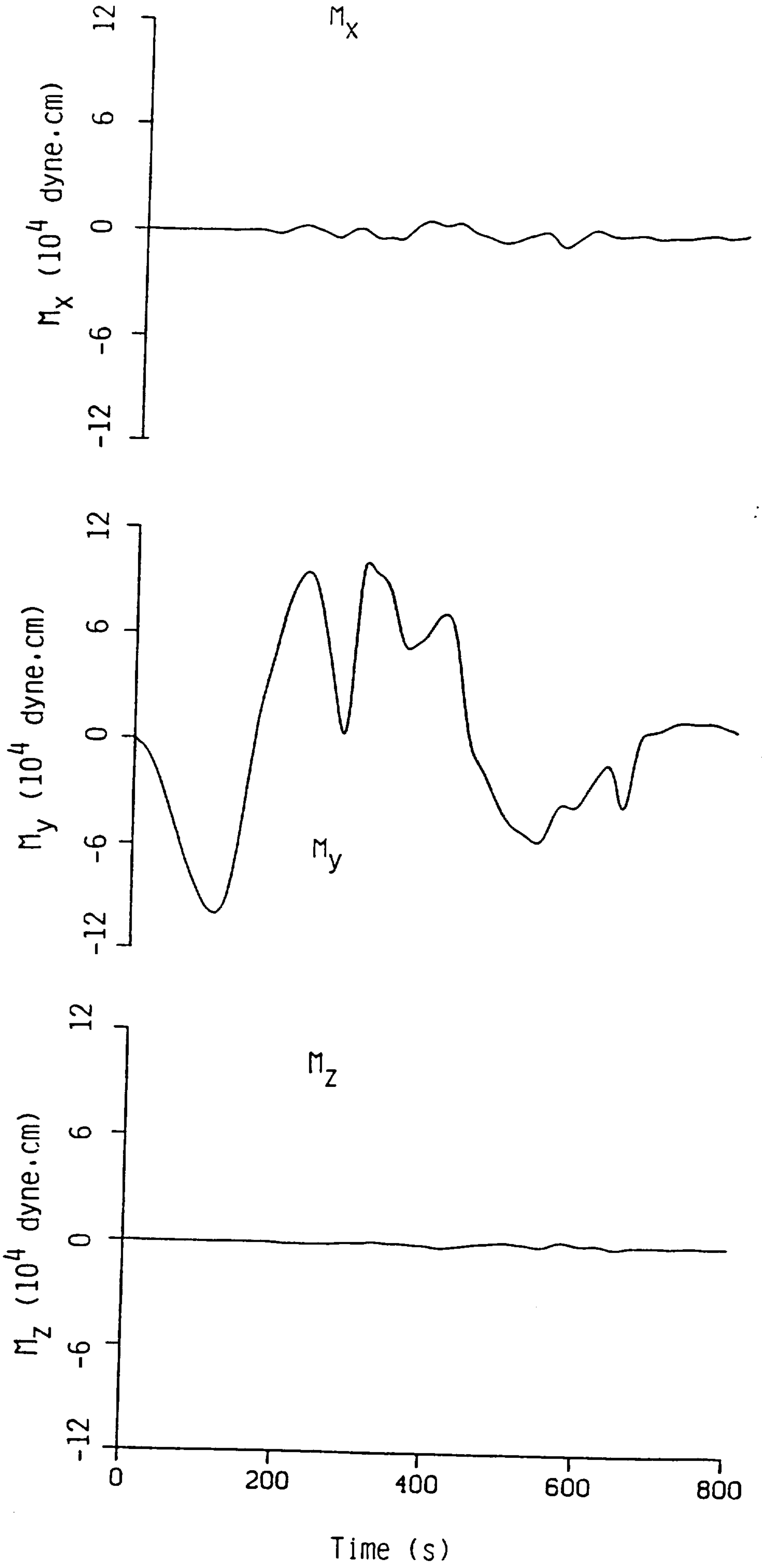

Fig. 25

AXAF-S
VARIATIONS OF STRESS
FORCES ACTING ON THE
DEWAR TANK

(F_x, F_y, F_z)

Driven by
Gravity Gradient
Acceleration
Associated With
Slew Motion

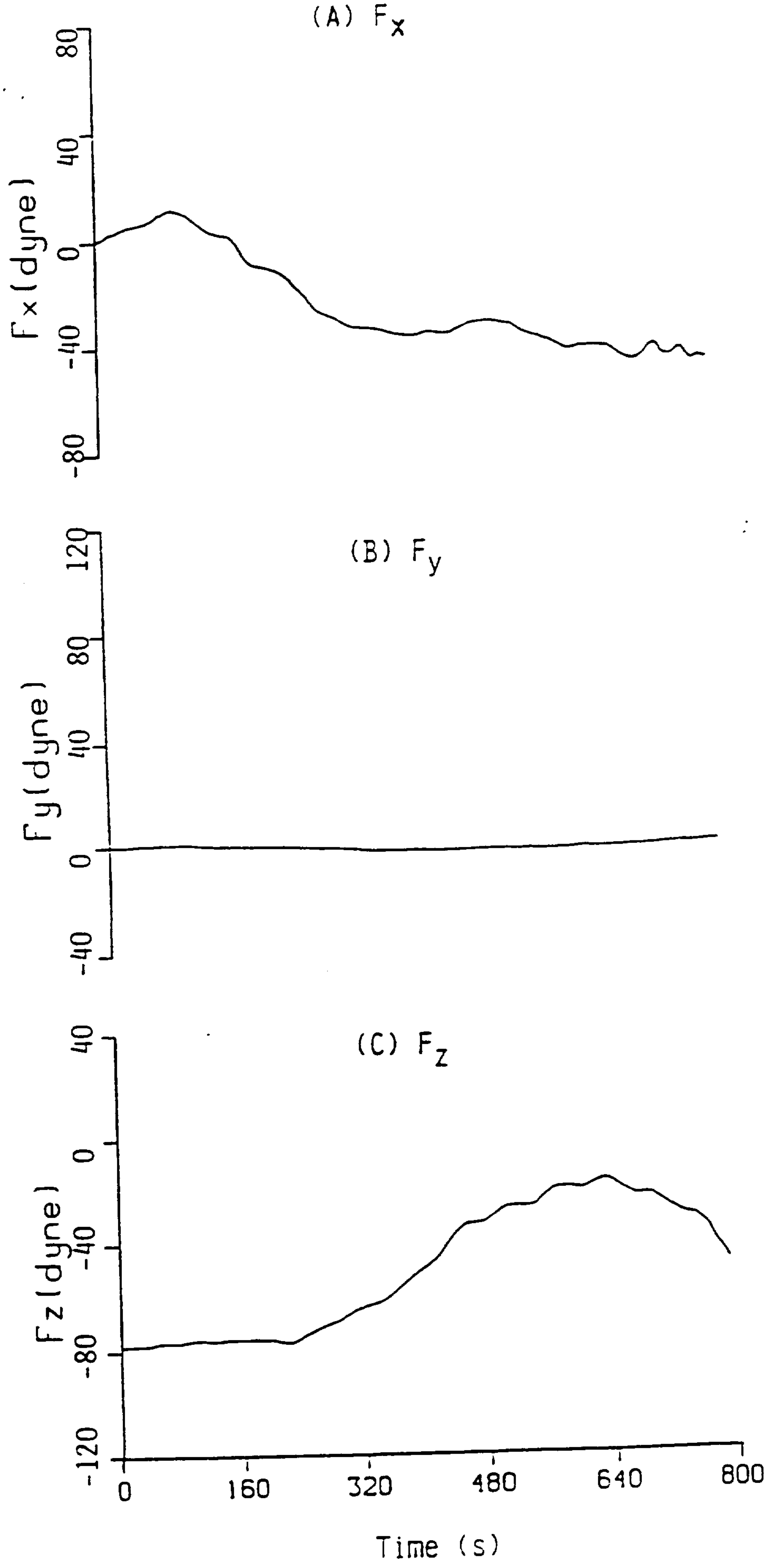

Fig. 26

AXAF-S

VARIATIONS OF VISCOUS STRESS MOMENTS ACTING ON THE DEWAR TANK

(M_x, M_y, M_z)

Driven by Gravity Gradient Acceleration Associated With Slew Motion

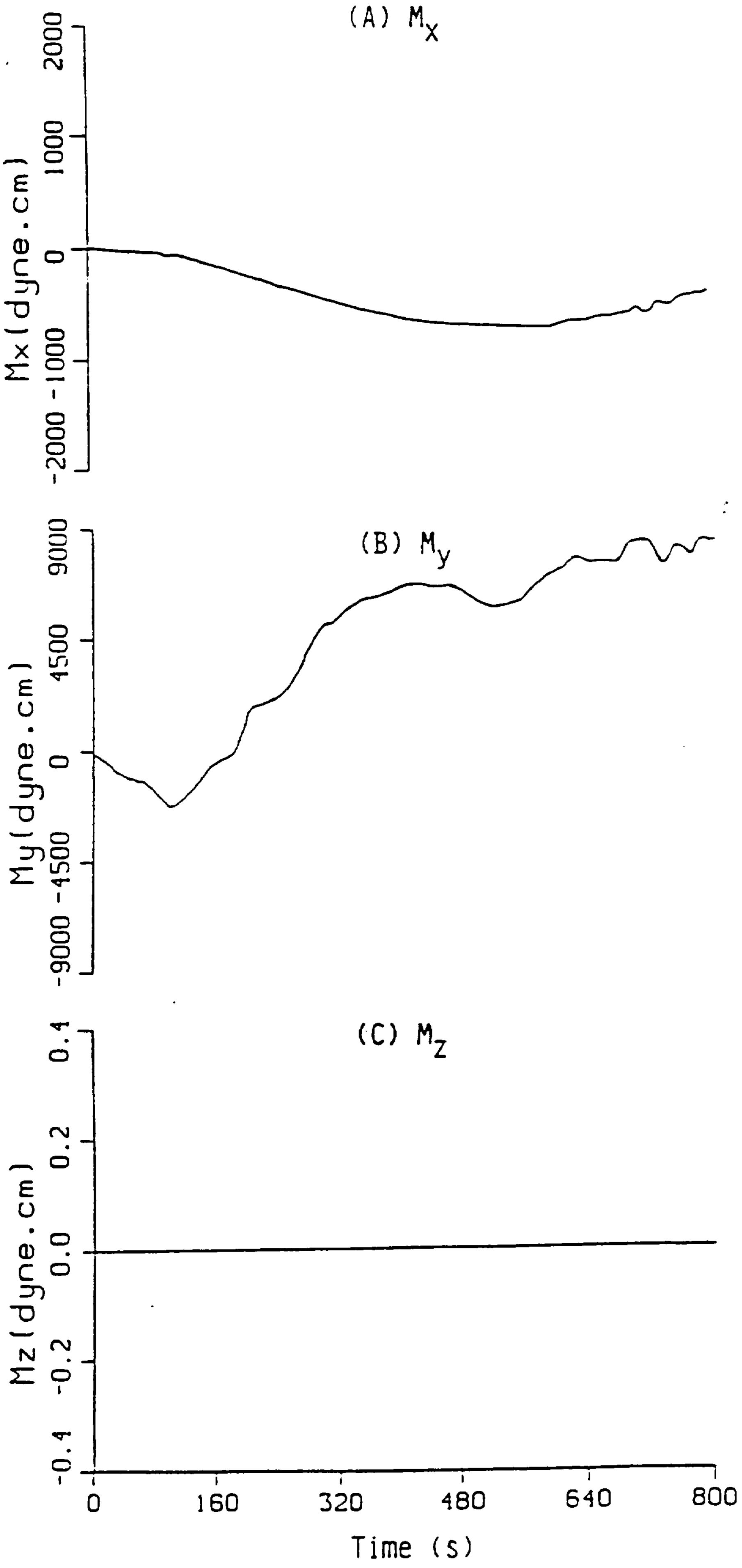

Fig. 27

AXAF-S
VARIATIONS OF MOMENT
ARMS OF VISCOUS STRESS
MOMENT ACTING OF THE
DEWAR TANK

(L_x, L_y, L_z)

Driven by
Gravity Gradient
Acceleration
Associated With
Slew Motion

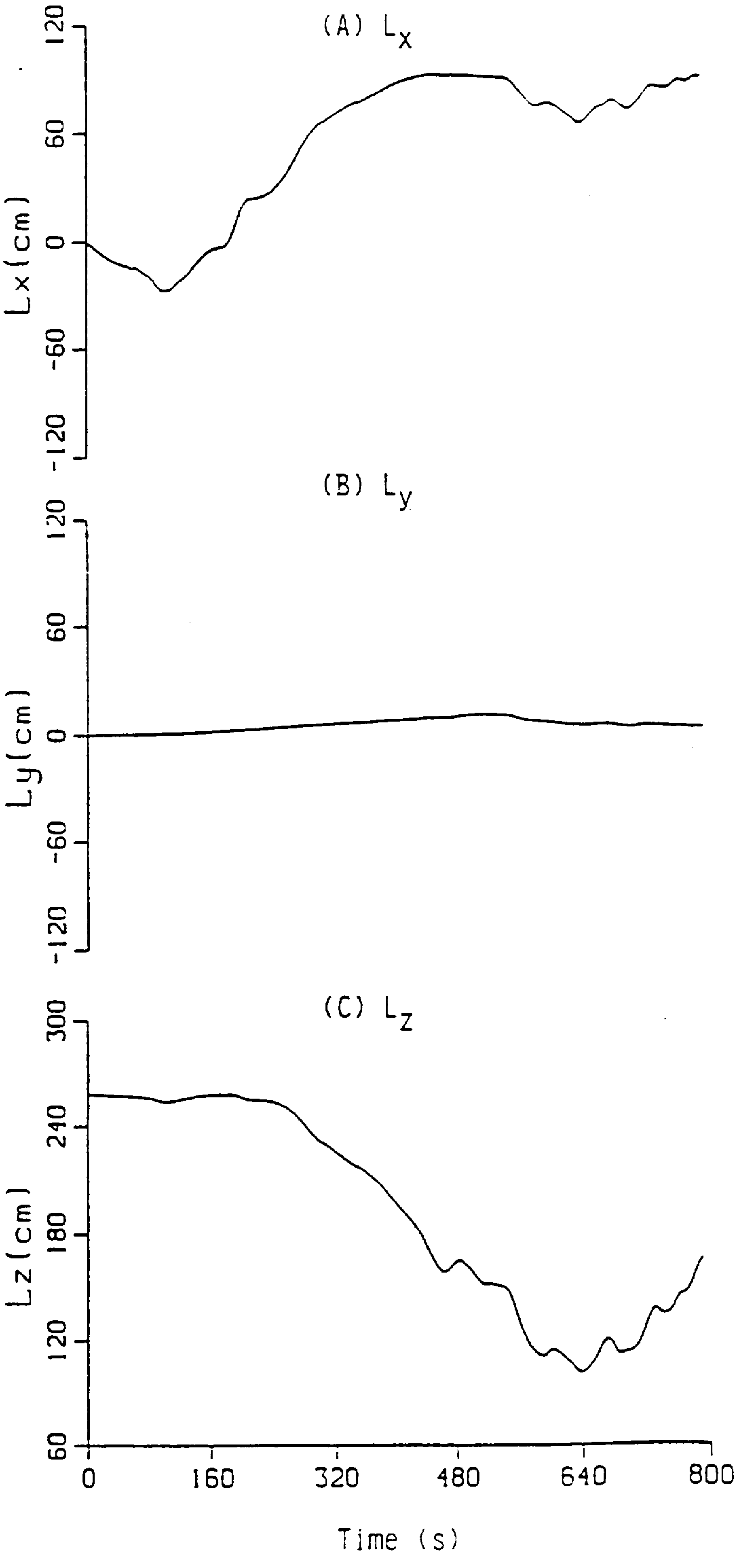

Fig. 28

AXAF-S
VARIATIONS OF STRESS
FORCES ACTING ON THE
DEWAR TANK

(F_x, F_y, F_z)

DRIVEN BY
JITTER ACCELERATION
ASSOCIATED WITH
SLEW MOTION

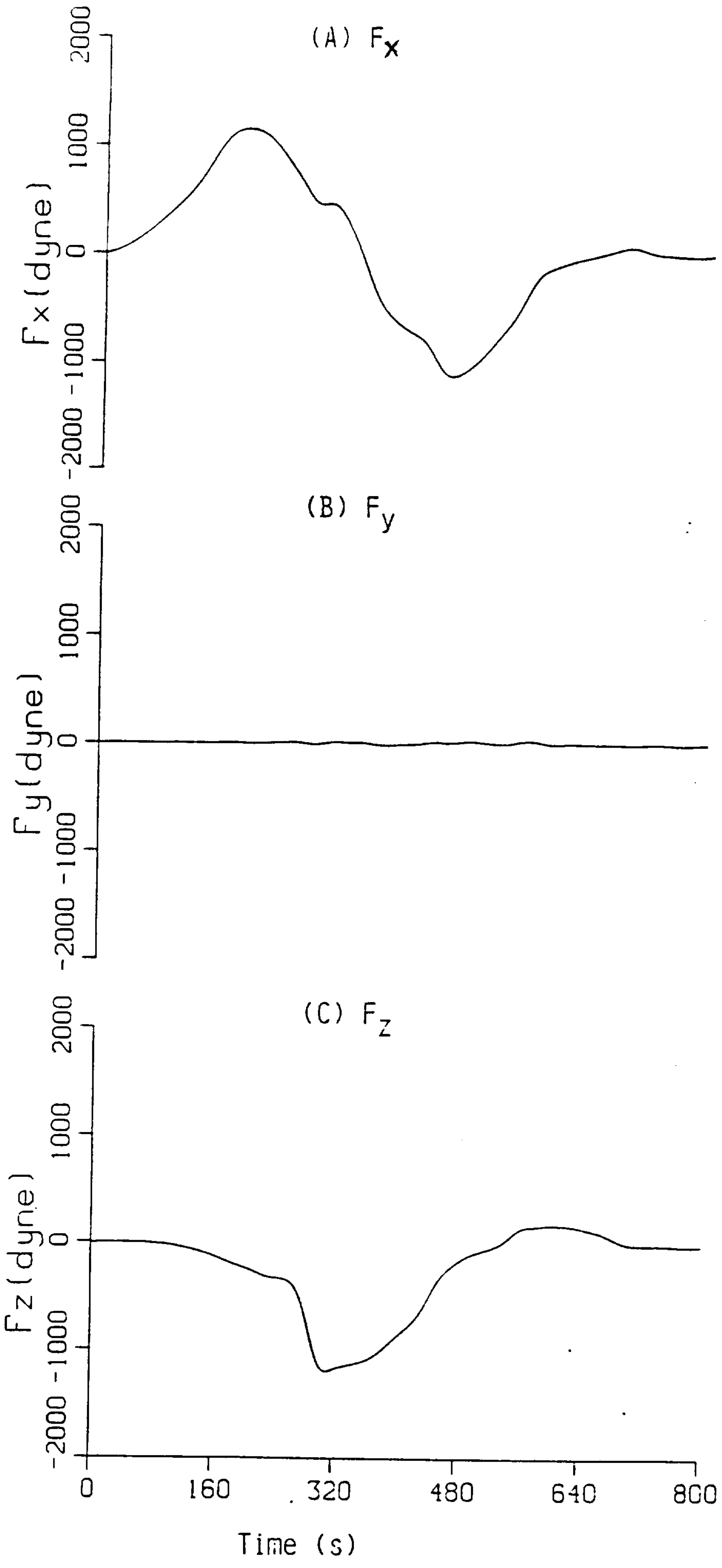

Fig. 29

AXAF-S
VARIATIONS OF VISCOUS
STRESS MOMENTS ACTING
ON THE DEWAR TANK

(M_x, M_y, M_z)

Driven by
Jitter Acceleration
Associated With
Slew Motion

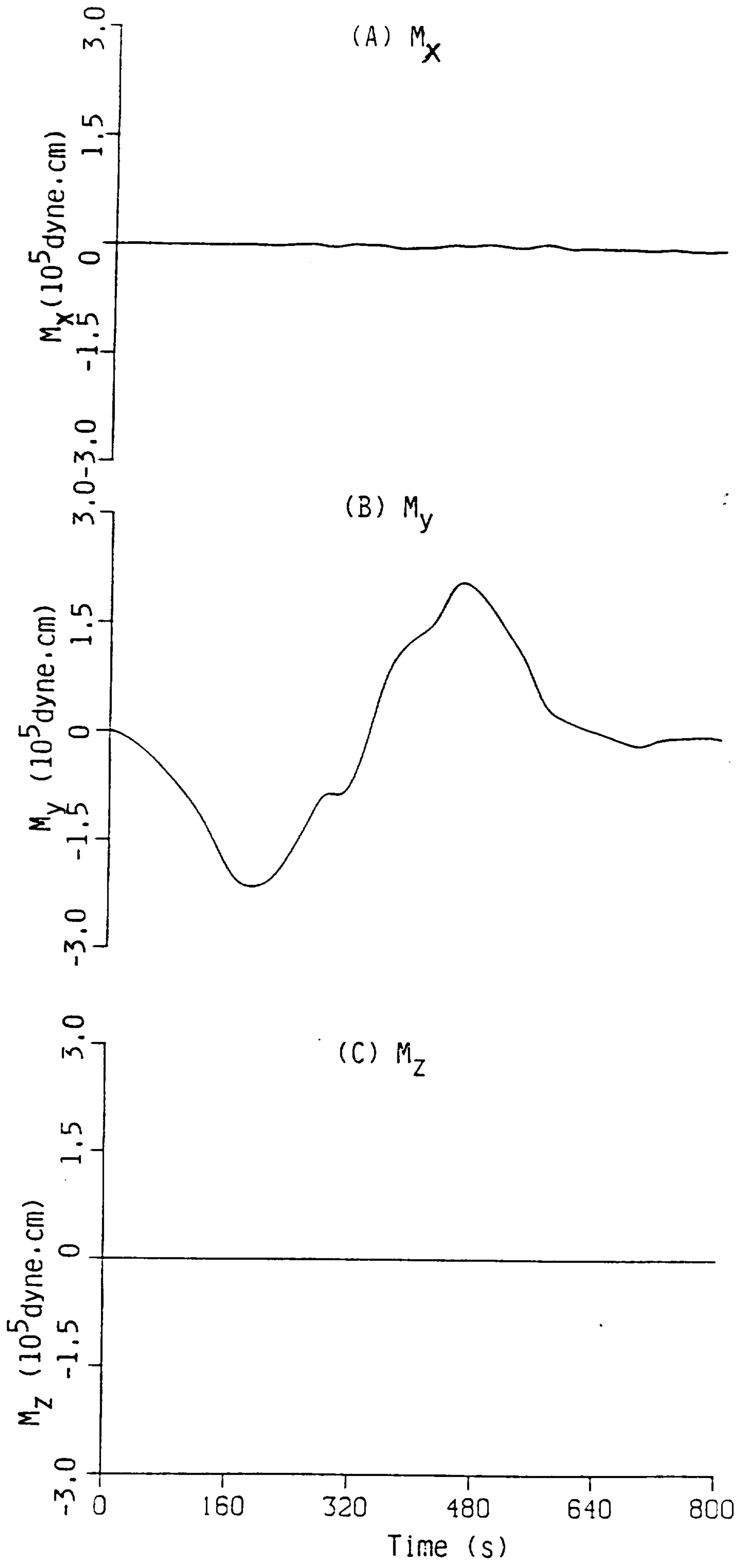

Fig. 30

AXAF-S VARIATIONS
OF MOMENT ARMS OF
VISCOUS STRESS
MOMENT ACTING ON
THE DEWAR TANK

Driven by
Jitter Acceleration
Associated With
Slew Motion

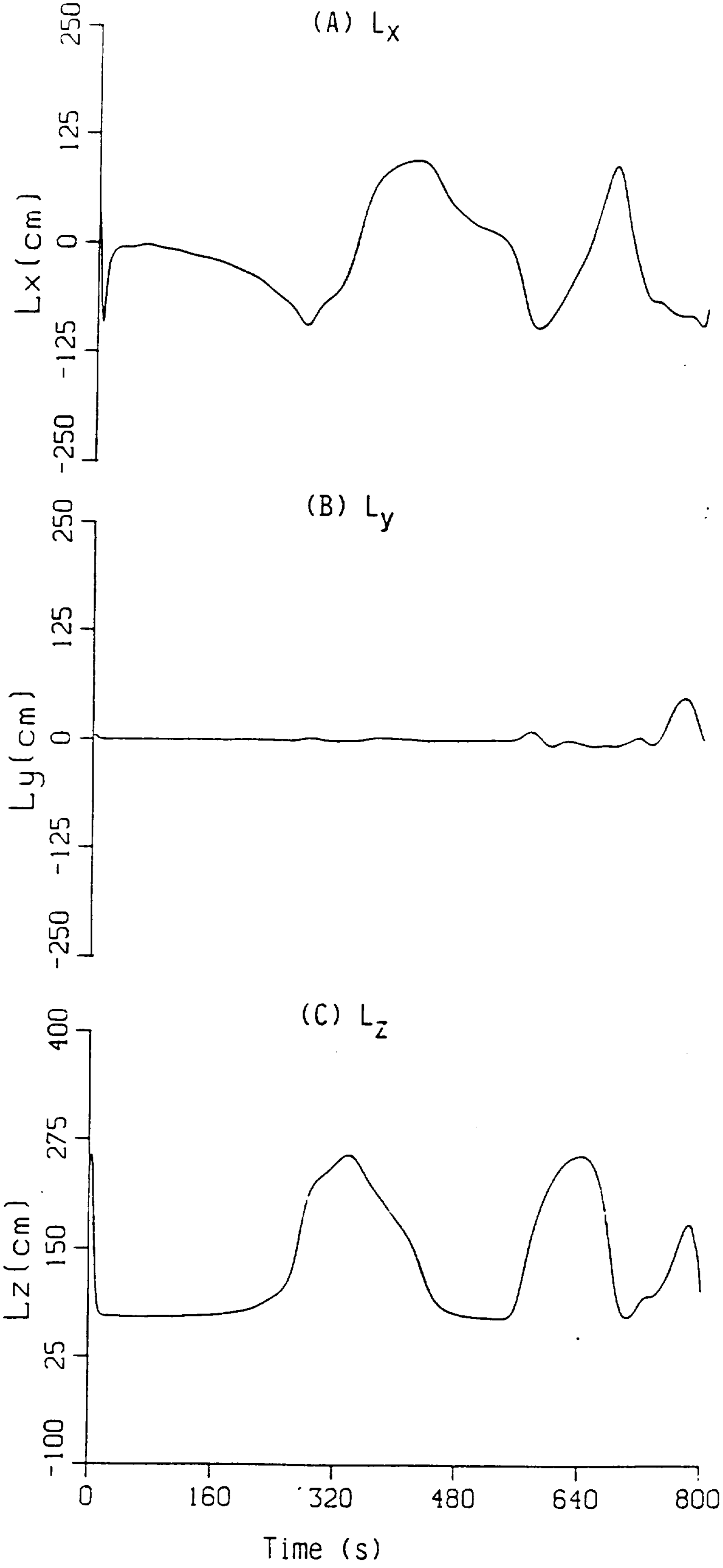

Fig. 31

NASA
National Aeronautical and Space Agency

Report Document Page

1. Report No.

2. Government Accession No.

3. Recipient's Catalog No.

4. Titile and Subtitle Superfluid Helium Sloshing Dynamics Induced Oscillations and Fluctuations of Angular Momentum, Force and Moment Actuated on Spacecraft Driven by Gravity Gradient or Jitter Acceleration Associated With Slew Motion

5. Report Due

6. Performing Organization Code
University of Alabama in Huntsville

7. Aurthor(s)
R. J. Hung

8. Performing Organization Report No.

9. Performing Organization Name and Address
University of Alabama in Huntsville
Huntsville, Alabama 35899

10. Work Unit No.

11. Contract or Grant No.
NAS8-38609 Delivery Order No. 96

12. Sponsoring Agency Name and Address
National Aeronautics and Space Administration
Washington, D.C. 20546-001
Marshall Space Flight Center, AL 35812

13. Type of report and Period covered
Final Report

14. Sponsoring Agency Code

15. Supplementary Notes

16.Abstract

The mathematical formulation of orbital spacecraft sloshing dynamics for partially filled liquid of cryogenic superfluid helium II in dewar container driven by the gravity gradient acceleration associated with slew motion are studied. The Advanced X-Ray Astrophysics Facility-Spectroscopy (AXAF-S) spacecrafts is chosen as a practical example in this study. Explicit mathematical expressions to manage orbital gravity gradient acceleration associated with slew motion which is acting on the spacecraft fluid systems are derived. The numerical computation of sloshing dynamics is based on the non-inertia frame spacecraft bound coordinate, and solve time-dependent, three-dimensional formulations of partial differential equations subject to initial and boundary conditions. The numerical computation of fluid viscous stress forces and moment fluctuations exerted on the dewar container driven by gravity gradient acceleration associated with slew motion are investigated. This study discloses capillary effect of sloshing dynamics governed liquid-vapor interface fluctuations, fluid viscous forces and moment fluctuations exerted on the spacecraft system and their relationship with the major driving force of gravity gradient acceleration associated with slow motion which affects the stability of the orbital spacecraft fluid system in a microgravity environment.

17. Key Words (Suggested by Author(s))
AXAF-S Spacecraft, Sloshing Dynamics, Spacecraft Slew Motion, Microgravity, Superfluid Helium, Gravity Gradient Acceleration, Fluid Force Activated on Dewar Container, Fluid Moment Activated on Dewar Container

18. Distribution Statement

19. Security Class. (of this report)
Unclassified

20. Security Class. (of this page)
Unclassified

21. No. of pages

22. Price